IMPLEMENTATION OF THE TWO-SCALE APPROXIMATION IN AN OPERATIONAL WAVE MODEL

by

Jean-Pierre Auclair

Submitted in partial fulfillment of the requirements
for the degree of Master of Science

at

Dalhousie University
Halifax, Nova Scotia
November 2011

DALHOUSIE UNIVERSITY

DEPARTMENT OF OCEANOGRAPHY

The undersigned hereby certify that they have read and recommend to the Faculty of Graduate Studies for acceptance a thesis entitled "IMPLEMENTATION OF THE TWO-SCALE APPROXIMATION IN AN OPERATIONAL WAVE MODEL" by Jean-Pierre Auclair in partial fulfillment of the requirements for the degree of Master of Science.

Dated: November 23, 2011

External Examiner: _____

Co-Supervisors: _____

_____

Readers: _____

_____

DALHOUSIE UNIVERSITY

DATE: November 23, 2011

AUTHOR: Jean-Pierre Auclair

TITLE: IMPLEMENTATION OF THE TWO-SCALE APPROXIMATION IN AN OPERATIONAL WAVE MODEL

DEPARTMENT OR SCHOOL: Department of Oceanography

DEGREE: M.Sc. CONVOCATION: May YEAR: 2012

_____

Signature of Author

TABLE OF CONTENTS

LIST OF FIGURES

ABSTRACT

Accurate evaluation of the non-linear wave-wave energy transfer requires a significant proportion of the computation time of ocean wave models. The Discrete Interaction Approximation (DIA) developed within the first version of the WAM model (*WAMDI*, 1988) is the only algorithm to be used today in operational wave modelling as it is the only way to calculate the wave-wave interactions rapidly enough. In this study, the Two-Scale Approximation (TSA), a potential successor method to the DIA, was successfully implemented in the third generation operational wave model WAVEWATCH III^{TM}(WW3). Preliminary results (*Perrie and Resio*, 2009) showing that it offers improved accuracy are confirmed in this study by the modelling of wave evolution under constant winds. Fetch-growth curves and two-dimensional spectra for energy and non-linear wave-wave interactions obtained using the TSA in these conditions show better agreement to more exact computations of non-linear interactions, than the DIA results. Modelling of a variety of SWAMP-type tests (*SWAMP*, 1985) allowed an investigation of the capabilities of the current implementation of the TSA method. From these experiments, several potential improvements to the implementation of the method have been found which will widen the scope of applicability of this formulation to the more realistically complicated sea states encountered in operational modelling.

LIST OF ABBREVIATIONS AND SYMBOLS

AvDI	Advanced Dominant Interaction approximation
DIA	Discrete Interaction Approximation
Exact-NL	Exact Non-Linear interaction method
GMD	Generalized Multiple DIA
JONSWAP	JOint North Sea WAve Project
NNIA	Neural Network Interaction Approximation
WAM	WAve Modeling system
WRT	Webb-Resio-Tracy method
WW3	WaveWatchIII wave model

F	Energy spectrum	$m^2 Hz^{-1}$
f	Frequency	Hz
f_p	Peak frequency	Hz
H_s	Significant wave height	m
k	Wavenumber	m^{-1}
N	Action spectrum	m^2
S_{ds}	Dissipation source term	m^2
S_{in}	Wind input source term	m^2
S_{nl}	Non-linear interactions source term	m^2
σ	Intrinsic frequency	Hz
T	Time scale	hr
θ	Directions	$degrees$

ACKNOWLEDGEMENTS

First amongst the many people who deserve to be acknowledged are my supervisors, Dr. Will Perrie and Dr. Jinyu Sheng, for their unfaltering support. Their advice as research and academic supervisors, covering everything from the elaboration of the research project to the refinements of the thesis, was defining for this project. For his unmatched helpfulness with the understanding of the model code and the tackling of the main topic of this work, Bechara (Bash) Toulany marked my time working at BIO. Don Resio, from the U.S. Army Research and Development Center, provided the initial inspiration and supplied the basic code of the TSA. Many thanks go to Daniel Morrison, for his diligence in solving the many computer or network related issues I encountered, to Eric Oliver for discussions of the intricacies of LaTeX document writing and to all my friends at Dal for making my time in Halifax as enjoyable as it has been. Finally, I want to thank my parents, for setting me on this path and helping me along it, as well as Canada's Panel on Energy Research and Development and the National Ocean Partnership Program of the US Office of Naval Research for funding this project.

CHAPTER 1

INTRODUCTION

1.1 Background

The numerical prediction of ocean waves has been a challenge for years. Wave models require a sufficient resolution in spectral space in order to represent multiple components of the wave field. This change from the modelling of physical space only to physical and spectral spaces increases both the complexity and the number of computations necessary in the model. Because of computing time constraints, an accurate description of the evolution of the full wave spectrum related to the sea state, including all non-linear processes, is still beyond the reach of operational wave models currently used in forecasting.

Ocean waves prediction is important for a variety of applications (e.g. marine forecasts related to fisheries, transport, search and rescue, offshore development and recreation) and will benefit from refinements of the forecasted wave spectrum. Products of wave forecasts are currently often limited to significant wave height (H_S), mean wave direction and peak period, but additional information could be provided to end users, which would be useful if the accuracy of the modelled sea state were increased. Further knowledge of the variability in the waves could prove to be highly valuable for ship safety and operations as the impact of waves on ships depends on their frequencies as well as the overall wave height distribution. Producing reliable assessments of wave climatology is also important for infrastructure design and coastal engineering. As the coastal populations in the world

keep increasing, proper estimates of wave impacts on the coastal areas become even more relevant, especially in view of possible changes in storm climatology and associated waves, due to global warming. Furthermore, a proper description of ocean wave energy spectra can be used to improve the evaluations of ocean mixing (*Qiao et al.*, 2004; *Smith*, 2006; *Warner et al.*, 2010) while also being central to a more physics-based approach to computation of fluxes of energy, momentum, moisture and gases at the ocean-atmosphere boundary in modelling (*Moon et al.*, 2004).

Several wave models are currently in operation and most of them are maintained by organizations dedicated to weather prediction. Two of the most widely used operational wave models are the WAve Modeling (WAM) system maintained by the European Center for Medium-Range Weather Forecast and the WaveWatch III^{TM}model (hereafter WW3) developped by Hendrik L. Tolman at the National Oceanic and Atmospheric Administration (NOAA). WW3 has been developed following WAM and the two models share a similar approach and modular structure, along with parameterizations and approximations based on recent research. They are therefore of comparable skill when used to model wave evolution and could also both make use of a better representation of the non-linear processes that determine development of the wave energy spectrum.

Wave evolution can be described in terms of the wave energy equation which considers wind energy input, non-linear energy transfer between waves and wave dissipation (e.g. due to white-capping). In current operational wave models, the non-linear energy transfer is often calculated using the Discrete Interaction Approximation (DIA) method described in *Hasselmann and Hasselmann* (1985) and *Hasselmann et al.* (1985). Research studies tend to use alternate methods in favour of higher accuracy, such as the the Webb-Resio-Tracy (WRT) method developed by *Webb* (1978), *Tracy and Resio* (1982) and *Resio and Perrie* (1991). The DIA and WRT methods offer either high computational efficiency and limited skill or time consuming computation of accurate results, respectively. Neither method has seen significant changes since their original development several decades ago but advances in computer electronics have been remarkable. Current resources dedicated to modelling

are able to support new methods such as the Two-Scales Approximation (TSA) (*Resio and Perrie*, 2008), which are able to compute non-linear wave-wave interactions more accurately than the DIA, while being faster than the WRT method.

1.2 Literature Review

1.2.1 The Three Generations of Numerical Wave Models

Numerical wave models are often described as belonging to one of three generations. These three generations came successively when significant improvements in the physics of wave models were achieved. The type of wave physics used in a model determine which generation the model belongs to. First generation wave models are associated with a combination of empirical relationships and assumptions used to simplify the evolution of waves for given wind conditions and fetch or duration relations. These models neglect non-linear wave interactions completely and tend to be very limited in their scope and capabilities. However, they can still be very useful tools if applied to a specific problem. Environment Canada still uses a first generation model for the analysis of trapped-fetch waves, a situation where waves and an associated storm move in synch. By keeping up with the waves, the storm can continue to supply energy for wave growth until they become dangerously large (*Bowyer and MacAfee*, 2005). This model considers waves of only one frequency and a limited relative spread between wind and wave directions. However, the model does have reasonable skill in forecasting waves and no third generation model can compete with its execution time. This modeling system is therefore useful for forecasters as they can analyse different scenarios quickly, helping them to cope with the often capricious nature of tropical storms (*MacAfee and Bowyer*, 2005).

The development of second generation models was based on the implementation of the wave energy (or wave action) spectrum. However, the lack of a proper representation of non-linear energy transfer in second generation models forces them to use assumptions

which severely limit their possibilities in terms of the shape of the energy spectrum. Models which represent the energy spectrum use the energy transfer equation:

$$\frac{\partial F}{\partial t} + (\cos\phi)^{-1}\frac{\partial}{\partial \phi}(V_\phi \cos\phi F) + \frac{\partial}{\partial \lambda}(V_\lambda F) + \frac{\partial}{\partial \theta}(V_{\theta g} F) = S(\phi, \lambda, F) \tag{1.1}$$

$$V_\phi = \frac{c_g \cos\theta + U_\phi}{R}, \tag{1.2}$$

$$V_\lambda = \frac{c_g \sin\theta + U_\lambda}{R\cos\phi}, \tag{1.3}$$

$$V_{\theta_g} = \dot{\theta} - \frac{c_g * \tan\phi\cos\theta}{R}, \tag{1.4}$$

$$S = S_{in} + S_{nl} + S_{ds} \tag{1.5}$$

where $\dot{\theta} = \frac{\partial\theta}{\partial t}$, c_g is the group velocity, U is the surface current speed and R is the radius of the Earth. In Eq.1.1, $F = F(f, \theta, \phi, \lambda, t)$ is the energy spectrum at a specific location in latitude, longitude coordinates (ϕ and λ, respectively) and at a given time t, expressed as a function of wave frequency f and direction θ, with $\theta = 0$ for waves traveling from west to east. The total source term, S, is defined as encompassing all sources and sinks of energy as well as the non-linear wave dynamics which are not described by the left side of Eq.1.1. Source terms include the wind input (S_{in}), the non-linear interactions (S_{nl}) and dissipation (S_{ds}), along with other possible terms. Although second generation models are based on the wave energy spectrum, they tend to use certain assumptions in order to restrict the spectral shape of the waves in the source terms used in Eq.1.1 in order to simplify the equation. Using several different models and test cases, it is shown in *SWAMP* (1985) that these assumptions in turn limit the capabilities of the models to represent a variety of situations like wind wave generation over pre-existing swell (waves which are decoupled from the wind). The removal of the assumed constraints on spectral shapes present in second generation models gives third generation models additional degrees of freedom to simulate sea state.

The most important improvement of third generation wave models over their second generation counterparts is the ability to resolve non-linear wave-wave interactions without

specifying the shape of the wave spectra *a priori*. This grants third generation models the flexibility needed to attempt to represent many kinds of waves created by evolving wind fields.

Results produced by the third generation wave models, however, are still limited by the accuracy of the implemented source terms. The proper resolution of non-linear interactions is proving particularly difficult due to its complexity and the high computational effort required to compute them accurately. Thus, although third generation models are the state of the art when it comes to wave modeling, second and even first generation models can also achieve comparable predicting skills when concentrating on certain model products. For example, models of all generation can simulate integrated variables more accurately as they depend weakly on the details of the spectral energy balance. This is the case for the significant wave height (H_S), the average wave height of the third largest waves measured from trough to crest. *Liu et al.* (2000) compared models from all three generations and obtained similar H_S predictions from the three different generations of wave models in a simulation of the waves on Lake Michigan. A similar conclusion is also reached by *Cardone et al.* (1996). These results could be interpreted as meaning that the increase in computer resources necessary for the operational use of third generation models might not be worth the cost. However, while all the wave models can forecast significant wave heights and wave directions to some extent, only the third generation models can reasonably represent the wave energy spectrum by explicitly computing wave processes in the source terms. The wave energy spectrum contains a wealth of information inaccessible to earlier generations of wave models but available to third generation models. This information can then be used to sustain more complex parameterizations of wave processes, air-sea momentum flux and ocean mixing, for example, allowing for a much more complete modeling of the ocean-atmosphere system. Therefore, third generation models have a non-negligible advantage over their predecessors when it comes to providing an accurate simulation of real world physics.

1.2.2 Wave Model Physics and Non-Linear Interactions

Proper representation of the different processes involved in the energy equation (Eq. 1.1) is necessary in order to accurately calculate spectral wave evolution. For example, wind-wave energy input (S_{in}) is often based on the theory of *Miles* (1957). In this approach to wind-wave interactions, different wave modes grow according to the curvature of the boundary layer wind field ($\frac{\partial^2 \mathbf{u}}{\partial z^2}$) at the height where the wind velocity is equal to the wave speed of a given mode. Negative curvature of the wind field (winds increasing slower with height, or a concave upward wind profile) will cause the waves to grow, whereas positive curvature will not further the growth of the waves. The wind profile (which is usually assumed to follow a logarithmic profile in the absence of waves) has a natural negative curvature and allows for the growth of waves. In the long term, the waves would grow to such an extent as to use all the available energy from the wind and then stabilize, leaving a linear wind profile (*Janssen*, 1982).

For wave propagation, and generally in wave modelling, the concept of wave action (*Whitham*, 1965; *Andrews and McIntyre*, 1978) is also very important in wave models. Wave action is defined as $N = F/\sigma$, where F is the energy and σ is the intrinsic angular frequency, as observed in the coordinate system moving with the mean flow. Wave action is particularly useful since it is conserved during interactions, which is important when currents are present. To this day, numerical wave models still are based on the determination of the evolution of wave action density spectra as in Eq. (1.1).

The computation of non-linear wave-wave interactions is a very significant component of third generation wave models, essential in distinguishing them from their second generation predecessors. In current third generation operational wave models, the Discrete Interaction Approximation (DIA, described in section 2.1.3) is used to resolve non-linear wave-wave interactions (*Hasselmann and Hasselmann*, 1985). This method sacrifices accuracy for computational efficiency in order to ensure that the wave models can run simulations quickly enough to be used for forecasts. Methods which compute non-linear interactions with a high degree of accuracy do exist, but their use is impossible in operational modeling

as they are extremely expensive computationally. The WRT method, for example, typically requires 10^3 to 10^4 times longer computational time than the DIA to complete a given simulation (*Tolman*, 2009). Therefore, other methods are being considered which would improve on the accuracy of non-linear interactions compared to the DIA, while not being as computationally expensive as the so-called exact methods.

The simplest step forward, given the success of the DIA as the only method used in operational modeling for more than 20 years, is to broaden the interactions considered in the spectral space by the method to obtain a more accurate basis to the approximation. This method is called the Generalized Multiple DIA method (GMD, see *Tolman*, 2008). However, as the GMD still does not cover the whole integration space it therefore suffers from similar shortcomings as the DIA, but to a lesser extent. Depending on the tests and comparisons, the GMD can be found to be too inaccurate to properly resolve the energy balance although it may be an interesting, easy improvement for operational purposes.

Building on the advancement in computer technology, an approach based on neural networks, known as the Neural Network Interaction Approximation (NNIA), is currently being developed. This method depends on the learning capabilities of neural networks, first training the methodology with pairs of spectra and calculated non-linear transfer, then using that "knowledge" to come up with an energy transfer for given wave spectra (*Tolman et al.*, 2005). While the NNIA has potential for operational purposes, it suffers from not physically or mathematically deriving its non-linear transfer, which can be a problem in process studies.

Other methods that are currently under development include experimental approximation methods which make use of precomputed energy transfers. The Advanced Dominant Interaction method (AvDI) takes advantage of certain scaling properties of the non-linear transfer in order to reduce the amount of calculations necessary to obtain an accurate estimate (*Perrie et al.*, 2010). For a given wavevector, a dominant part of the non-linear transfer occurs when interacting with some other specific wavevectors. In this approach,

the total interaction is approximated by scaling the dominant transfer with a parameter obtained through comparisons of the given spectrum with other, pre-processed spectra using fuzzy logic.

1.3 Objectives

Operational wave models are currently limited in their capabilities due to their poor simulation of wave energy or action spectra. Another area that has suffered from the inaccuracies of current models is the investigation of the dynamics of wave evolution. This can be addressed by implementing more accurate methods for the computation of non-linear energy transfer which will consider the entirety of the wave spectrum in the calculations of the wave-wave interactions for every wave frequency and direction. In order to achieve this, three main objectives were set for this study:

- To complete the implementation of a modern approximation of the non-linear wave-wave interactions, the TSA, in WW3.
- To compare versions of WW3 using (i) DIA, (ii) the new implementation of the TSA and (iii) the WRT method, in terms of accuracy, in order to demonstrate the potential of an operational wave model using the TSA
- To investigate possible modifications to the new implementation of the TSA in order to improve the value of the approximation for operational modelling.

While *Perrie and Resio* (2009) demonstrated the potential of the TSA method, their experiment used predetermined observed spectra and computed the transfers outside of a numerical model. The goal of this project is to demonstrate the advantages offered by using the TSA for the non-linear transfers over multiple integrations as resolved in the case of evolving spectra in a numerical model.

The DIA is the only numerical method used in operational wave modeling to this day and is therefore the reference against which new methods have to be compared. Once the

TSA is successfully implemented, the performance of the two models (operational WW3 using DIA and WW3-TSA) will be assessed against results obtained using the more exact interactions computed by the WRT method in SWAMP test cases such as the evolution of a wave field under constant or changing winds.

1.4 Structure

Chapter 2 describes the main components of the numerical wave model used for this work, WW3, including the available source terms used for the simulations: wind-wave interactions, wave dissipation and non-linear interactions using both the DIA or WRT methods, as well as the numerical schemes used for advection and time integration. Chapter 3 describes both the theory behind the TSA and its implementation in WW3. Chapter 4 presents simple numerical experiments performed with a one point model used to assess the potential of the TSA for the computation of the wave-wave interactions for evolving spectra. Chapter 5 covers experiments performed with the physical domain extended to two-dimensions so that the impact of advection schemes and fetch on wave evolution can be investigated. Chapter 6 summarizes and discusses the results of the previous experiments and their consequences.

CHAPTER 2

MODEL DESCRIPTION

WAVEWATCH III (WW3, see *Tolman* 2009) is a numerical wave model developed and used for operational purposes at the National Centers for Environmental Prediction (NCEP). Written using fortran90 with a modular structure, the model can be run in parallel, taking advantage of multiple processors in order to reduce elapsed computational time, and allows the user to choose between different representations of wave physics.

The model setup for the theoretical experiments performed in this study makes use of a Cartesian formulation of the space domain for simplicity, although a longitude-latitude formulation is also available. Only water depths which are well beyond the threshold for shallow water waves are used in the experiments performed. As a result, depth-induced breaking, triad interactions and wave bottom scattering are all considered to be negligible. The numerical simulations take into account wind-wave interactions, non-linear wave-wave interactions and wave dissipation and are done with two different advection schemes.

2.1 Source Terms

As introduced in section 1.2, source terms for wave energy attempt to include all the energetics in a wave model and are calculated based upon the current sea state at each model point in space. The balance among them determines the evolution of the total energy in the waves. Spectral energy of the waves changes according to the two-dimensional

representation of the source terms in the model. The formulations used are therefore very important in order to obtain realistic simulations of the sea state.

2.1.1 Wind-Wave Interactions

In the experiments, the representation of the energy input to waves by the wind is based on the work of *Chalikov and Belevich* (1993) and *Chalikov* (1995). The implementation of this source term in WW3 is described in *Tolman and Chalikov* (1996). Using a two-dimensional model for extensive computations of the wave boundary layer, the wind-input parameter β, is investigated. This parameter defines the ratio between wave energy and the wind input term as a function of frequency ω as:

$$\beta(\omega) = \frac{\rho_a}{\rho_w} \frac{\epsilon(\omega)}{\omega S(\omega)} \tag{2.1}$$

where $\epsilon(\omega)$ is the spectral density of energy exchange, ρ_a is the air density, $S(\omega)$ is the wave energy spectrum and ρ_w is the water density. This parameter can be approximated by a piecewise continuous function, shown for different values of the drag coefficient in Figure 2.1 and given by:

$$10^4\beta = \begin{cases} -a_1\tilde{\omega}_a^2 - a_2, & \tilde{\omega}_a < -1 \\ a_3\tilde{\omega}_a(a_4\tilde{\omega}_a - a_5) - a_6, & \tilde{\omega}_a \in (-1, \Omega_1/2) \\ (a_4\tilde{\omega}_a - a_5)\tilde{\omega}_a, & \tilde{\omega}_a \in (\Omega_1/2, \Omega_1) \\ a_7\tilde{\omega}_a - a_8, & \tilde{\omega}_a \in (\Omega_1, \Omega_2) \\ a_9(\tilde{\omega}_a - 1)^2 + a_{10}, & \tilde{\omega}_a > \Omega_2 \end{cases} \tag{2.2}$$

where $\tilde{\omega}_a = \omega|u_\lambda|cos(\theta_r)/g$ is the non-dimensional wave frequency of a wave moving at angle θ_r with the wind, u_λ is the wind velocity at the height of the normalized wavelength λ_a given by:

$$\lambda_a = \frac{2\pi}{k|cos(\theta_r)|} \tag{2.3}$$

for a wavenumber k. In the approximation, a_1 to a_{10}, as well as Ω_1 and Ω_2, are parameters depending on the drag coefficient (c_λ) at that height (*Chalikov*, 1995) and defined as:

$$
\begin{aligned}
\Omega_1 &= 1.075 + 75C_\lambda, & \Omega_2 &= 1.2 + 300C_\lambda \\
a_1 &= 0.25 + 395C_\lambda, & a_3 &= (a_0 - a_2 - a_1)/(a_0 - a_4 + a_5) \\
a_2 &= 0.35 + 150C_\lambda, & a_5 &= a_4\Omega_1 \\
a_4 &= 0.30 + 300C_\lambda, & a_6 &= a_0(1 - a_3) \\
a_9 &= 0.35 + 240C_\lambda, & a_7 &= (a_9(\Omega_2 - 1)^2 + a_{10})/(\Omega_2 - \Omega_1) \\
a_{10} &= -0.05 + 470C_\lambda, & a_8 &= a_7\Omega_1 \\
& & a_0 &= 0.25a_5^2/a_4.
\end{aligned}
\tag{2.4}
$$

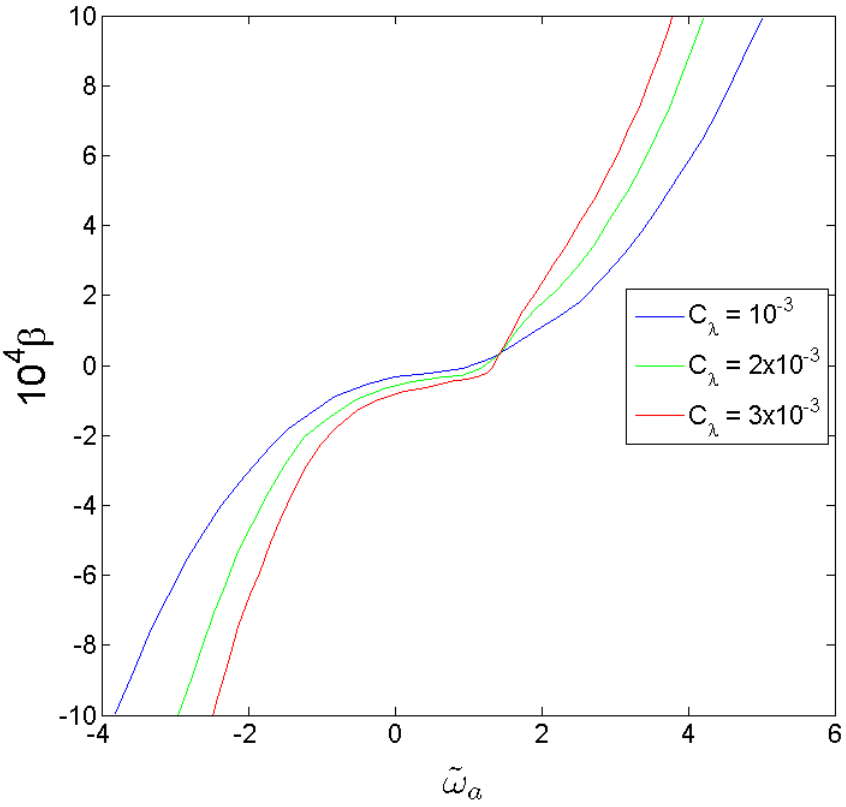

Figure 2.1: Wind-input parameter (β) as a function of apparent frequency ($\tilde{\omega}_a$) for different values of the drag coefficient (C_λ).

The wave model takes a reference wind velocity u_r at the height z_r and then produces the profile of wind velocities and drag coefficients as a function of height using a logarithmic wind layer approximation:

$$u_z = \frac{v_*}{\kappa} ln(\frac{z}{z_0}) \tag{2.5}$$

where v_* is the friction velocity, $\kappa = 0.4$ is the Von Kármán constant and z_0 is the roughness parameter obtained from the wave energy spectrum and wind properties. The profiles are thus given by:

$$u_\lambda = u_r \frac{ln(\lambda_a/z_0)}{ln(z_r/z_0)} \tag{2.6}$$

$$C_\lambda = C_r(\frac{u_r}{u_\lambda})^2. \tag{2.7}$$

The wave action spectrum $N(k, \theta)$ in the model is resolved on a two-dimensional space (k, θ). The formulation for the normalized interaction between wind and waves, S_{in}, is therefore extended to include multiple wave directions by using the two-dimensional action density and the interaction parameter for every wavenumber k and direction θ. The calculation of the wind input source term (S_{in}) is thus done for every spectral component individually using:

$$S_{in}(k, \theta) = \beta(\omega(k), \theta)\omega(k)N(k, \theta). \tag{2.8}$$

It is interesting to note that for waves moving faster than the wind, as well as waves moving against the wind, the wind input source term can be negative. Figure 2.2 shows such a case when the wind is perpendicular to the main wave direction. Here the energy growth is negative for waves going against the wind ($\theta > 270^0$) and it is positive where the swell has a component propagating along the wind around $\theta = 223^o$. The generation of new wind waves at higher frequencies is also visible.

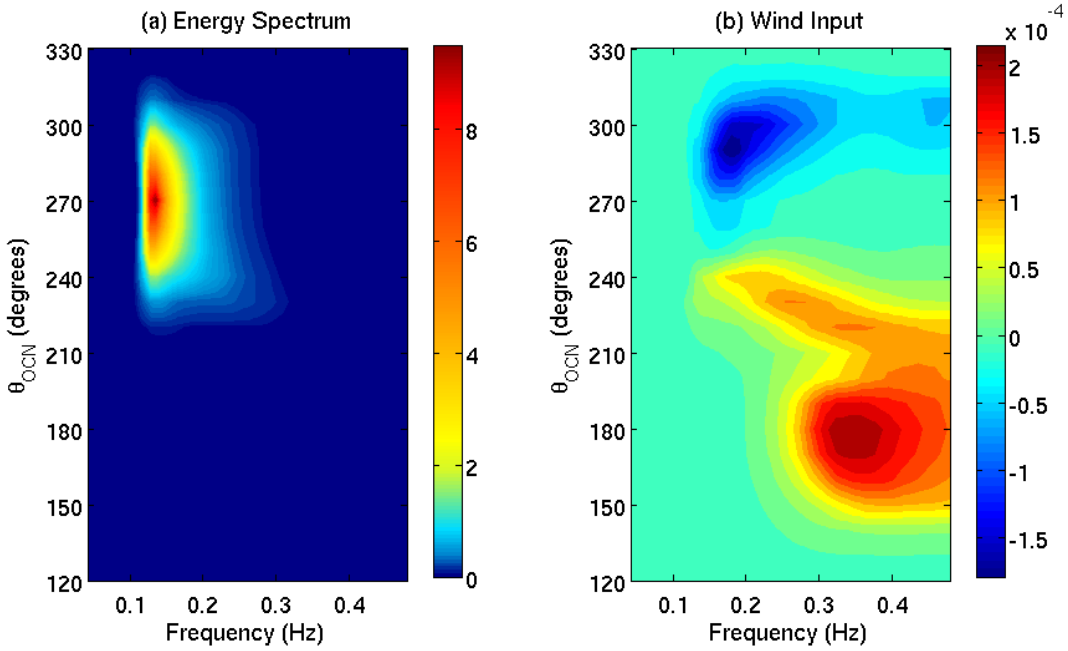

Figure 2.2: (a) Energy spectrum ($m^2 Hz^{-1}$) (left) and (b) wind-wave interactions (m^2), S_{in}, generated by easterly winds ($\theta = 270^o$) for 48 hours and northerly winds ($\theta = 180^o$) for 30 minutes. Angles θ_{OCN} are following the oceanographic convention.

2.1.2 Wave Dissipation

Wave dissipation encompasses the processes which remove energy from the existing wave field. One of the important processes is wave breaking (commonly called "whitecapping"). It can be described as the wave break-down that occurs when its energy content at a certain wavelength is too large, and the wave is too steep to be stable. The wave energy is then transferred to ocean mixing, currents and turbulence. Another important process is the interaction of waves with the water below them. Turbulence in the oceanic boundary layer causes a transfer of energy from the waves to the water column, further reducing their energy. Because both processes are very complex and neither is very well understood, the wave dissipation term in operational wave models is parameterized as a closure term, such that the overall wave evolution in the model follows observations (*Tolman and Chalikov*, 1996).

Most of the existing wave dissipation parameterizations are quasi-linear in the energy spectrum and take the form:

$$S_{ds} = -T_{ds}^{-1} F(f, \theta) \tag{2.9}$$

where F is the energy spectrum and T_{ds} is the dissipation time scale, which can be a function of environmental or spectral parameters, such as the wind velocity, wave direction or frequency. This formulation works well around the spectral energy peak and for frequencies lower than the peak frequency, the region known as the forward face of the spectrum. However, another approach is needed for the dissipation occuring at high frequencies.

The region of the energy spectrum where the frequency is about 2.5$\sim$3.5 times the frequency of the energy peak is known as the equilibrium range. In this region, source terms tend to cancel one another, resulting in a self-similar shape that only weakly depends on fetch. The timescales of evolution in the equilibrium range differ significantly from those of the forward face, therefore these two regions need to be considered separately for wave dissipation (*Tolman and Chalikov*, 1996). The dissipation components include: (i) a dissipation term for low frequencies similar to what would be used for turbulent viscosity in the oceanic boundary layer, and (ii) a purely diagnostic term designed to obtain the desired spectral shape at high frequencies.

The low frequency part of the parameterization comes from the energy flux to deeper water by the interaction of the wave motion with the underlying water. The formulation used in WW3 is based on the Reynolds Averaged Navier-Stokes Equations, and accounts for the mean flow, waves and turbulence, to define the local rate of wave energy dissipation, via the spectral form:

$$S_{ds,l}(f, \theta) = -2k^3 F(f, \theta) \int_0^\infty K(z) e^{-2kz} dz \tag{2.10}$$

where $K(z)$ is the eddy viscosity as a function of depth. Using dimensional analysis and neglecting stratification (the dissipation should mostly be in the mixed layer of the ocean), the eddy viscosity is found to depend on friction velocity (u_*), depth (z), high frequency wave height (h) and a dimensionless parameter representing wave age (ξ). Defining the effective eddy viscosity, K_e, as:

$$\begin{aligned} K_e &= k \int_0^\infty K(z) e^{-2kz} dz \\ &= u_* h \int_0^\infty k \tilde{K}(\frac{z}{h}, \xi) e^{-2kz} dz = u_* h \phi(\xi) \end{aligned} \tag{2.11}$$

where $\phi(\xi)$ is a nondimensional function of wave age found to be linear during the tuning process, leads to low frequency dissipation represented as:

$$S_{ds,l}(f, \theta) = -2 u_* h k^2 \phi(\xi) F(f, \theta). \tag{2.12}$$

Interestingly, this formulation means that there will be no dissipation in the absence of wind ($u_* = 0$) or high frequency waves ($h = 0$).

The high frequency dissipation term is a closure term, intended to be consistent with other source terms in the equilibrium range of the spectrum in the sense of constraining WW3 to compare as well as possible with observations. Since this region of the energy spectrum is largely independent of fetch, the balance should be attained between S_{in}, S_{nl} and S_{ds} and allow for a stable shape of the energy to fit an f^{-5} tail (in WW3) in this region. With the other two source terms and the desired shape known, it becomes a closure problem. Assuming that the balance

$$S_{in} + S_{nl} + S_{ds} = 0 \tag{2.13}$$

is achieved for a one-dimensional spectrum of the form

$$F(f) = \alpha g^2 (2\pi)^{-4} f^{-5} \tag{2.14}$$

and defining the interaction timescales at a given frequency as

$$T^{-1} = \frac{\int_\theta S d\theta}{\int_\theta F d\theta} \tag{2.15}$$

the timescale T of interaction can then be compared. Non-linear interactions scale by $f^{11}F^2$, which in this region of the spectrum corresponds to a linear dependence on frequency, whereas wind-wave interactions have a cubic dependence. The balance is thus mainly between input and dissipation in the equilibrium range. From this result and knowledge of the wave model numerics, the high frequency dissipation can be expressed as

$$\begin{aligned} S_{ds,h}(f,\theta) &= -a_0(\frac{u_*}{g})^2 f^3[\alpha_n(f)]^B F(f,\theta), \\ B &= a_1(\frac{fu_*}{g})^{-a_2}, \end{aligned} \tag{2.16}$$

where α_n is the frequency dependant nondimensional energy level from the definition of the energy spectrum in the equilibrium range (eqn. 2.14) normalized by a representative level which comes from tuning, along with a_0, a_1 and a_2.

Both high and low frequency dissipation terms are then blended linearly between frequencies, in order to obtain the full dissipation term in the model, an example of which is shown in Figure 2.3.

2.1.3 Non-Linear Wave-Wave Interactions

Non-linear energy transfer between ocean waves (S_{nl}, Eq.1.5) occurs between quadruplets of waves. Solving the formulation for interactions with a given wave represented by wavevector $\mathbf{k}_1$ thus requires consideration of all possible sets three wave vectors $(\mathbf{k}_2, \mathbf{k}_3, \mathbf{k}_4)$. Integration of the non-linear interactions over all three two-dimensional wave vectors thus yields the change in action density N_1 at wavenumber k_1 as a 6-dimensional integral in wave-number space specified by the Hasselmann equation:

$$\begin{aligned} S_{nl} = \int\int\int & G(\mathbf{k}_1,\mathbf{k}_2,\mathbf{k}_3,\mathbf{k}_4)\delta(\mathbf{k}_1+\mathbf{k}_2-\mathbf{k}_3-\mathbf{k}_4)\delta(\sigma_1+\sigma_2-\sigma_3-\sigma_4) \\ & \times[N_1N_3(N_4-N_2)+N_2N_4(N_3-N_1)]d\mathbf{k}_2 d\mathbf{k}_3 d\mathbf{k}_4 \end{aligned} \tag{2.17}$$

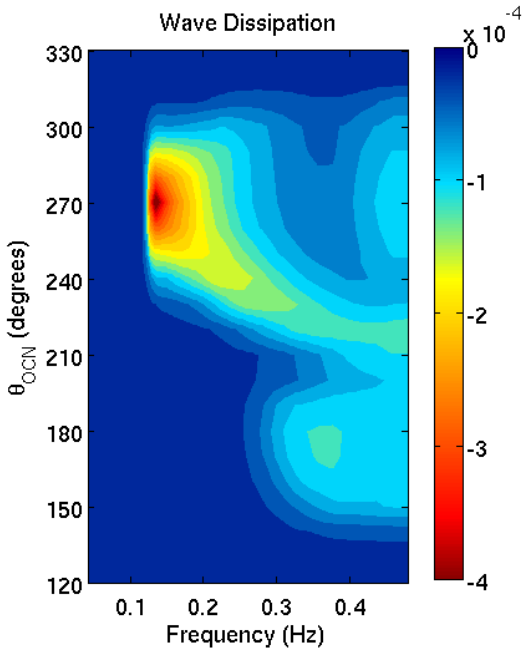

Figure 2.3: Wave dissipation (m^2) term calculated for the energy spectrum shown in Figure 2.2(a). Note the dissipation around the swell peak, the extension towards the new wind direction where higher frequency waves are developing and the local maximum for wind sea at higher frequency.

where the wave action densities $N_i = F_i/\sigma_i$ are defined for wavevectors k_i, G is a complicated coupling term (*Hasselmann*, 1962) and the delta functions enforce the two quadruplet interaction constraints:

$$\mathbf{k}_1 + \mathbf{k}_2 = \mathbf{k}_3 + \mathbf{k}_4, \tag{2.18}$$

$$\sigma_1 + \sigma_2 = \sigma_3 + \sigma_4. \tag{2.19}$$

This equation was also discovered independently by *Zakharov and Filonenko* (1966).

The non-linear interactions are responsible for the familiar shape of the wave energy spectrum, transferring energy from mid-frequencies and the spectral peak region (where input by wind is usually the largest) to lower frequencies, ultimately creating swell. This can be seen in Figure 2.4, which shows the non-linear interactions spectrum corresponding

to the energy spectrum presented in Figure 2.2(a). In this case, the energy transfer to lower frequencies is caused by negative interactions in mid-frequencies ($f \sim 1.6Hz$) and positive interactions below the energy peak ($f \sim 1.2Hz$). Energy transfers towards higher frequencies ($f > 0.45$ Hz in Fig.2.4) and side-lobes at about 45 degrees from the main wave direction ($\theta = 300^o$ in Fig.2.4) can also be seen. The positive side-lobes contribute to bimodal characteristics in spectra, as suggested by *Webb* (1978) and recently observed by *Long and Resio* (2007). The energy transferred to high frequencies is then lost to wave-breaking dissipative processes (S_{ds}).

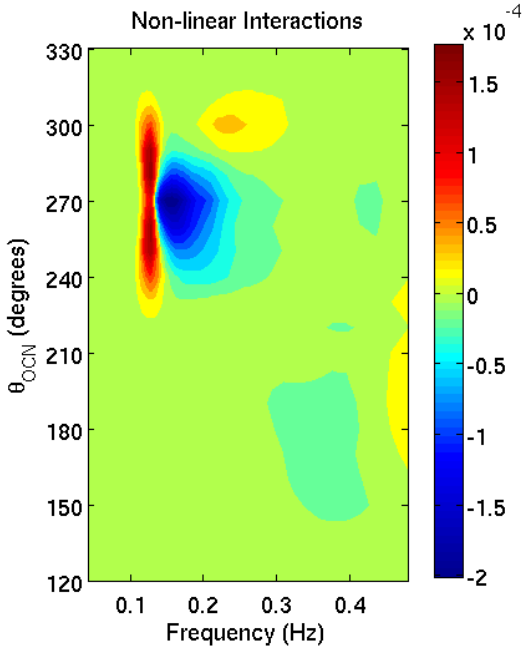

Figure 2.4: Non-linear interactions (m^2) calculated for the energy spectrum shown in Figure 2.2.

Third generation wave models can use a variety of methods for the computation of non-linear energy transfers, of which the most important is the Discrete Interaction Approximation (DIA) (*Hasselmann and Hasselmann*, 1985; *Hasselmann et al.*, 1985). It was developed for the first third generation model, WAM (*WAMDI*, 1988) and is still in use to this day, as it is the only method to be computationally efficient enough for operational models. The WAM model allows an explicit balance of wind input, non-linear

wave-wave interactions and wave dissipation, whereas previous models would underestimate non-linear interactions or neglect them altogether and overestimated wind input as a compensation. In third generation wave models, the explicit balance of source terms attempts to resolve as many degrees of freedom as the spectrum has, allowing energy to be distributed in response to the specifics of the forcing. Therefore, increasing the accuracy of the non-linear transfer calculation methods is related to increasing the number of degrees of freedom of the model. This freedom in the non-linear energy transfer also allows a greater freedom in spectral shapes; thus, situations where swell and wind seas are present or where winds change sharply (potentially creating multi-modal spectra) can be modelled much more accurately than in models of the preceding generations.

The interactions between waves of different frequencies and directions are central to the creation of the spectral shape. Besides the theoretical work done to understand the Hasselmann equation (Eq. 2.17), there is also the challenge of calculating the S_{nl} expression in a numerical wave model. Although it is possible to calculate the non-linear term exactly, it is a very expensive calculation computationally and, even with the resources available today, it is too inefficient for operational wave modeling. Of all the numerical methods that calculate the integral accurately, the first was developed by *Hasselmann and Hasselmann* (1985) and called Exact-NL. The Exact-NL method calculates the non-linear transfer by integrating over the whole discrete wave energy spectrum, essentially performing a summation over all wavenumbers, which is very time consuming. It was subsequently improved by using scaling properties of Eq. (2.17) and geometric arguments to avoid repeating certain parts of the calculations, which led to the equivalent, yet faster, Webb-Resio-Tracy method (*Webb*, 1978; *Tracy and Resio*, 1982; *Resio and Perrie*, 1991).

After the completion of the Exact-NL method, the Discrete Interaction Approximation (DIA) (*Hasselmann et al.*, 1985) was developed. It has become the workhorse of operational wave modeling to this day as its calculation time is orders of magnitudes faster than the so-called exact methods. The DIA is based on using only a subset of the interacting wavenumbers, which makes the reduction in calculation time possible, according to:

$$\omega_1 = \omega_2 = \omega \tag{2.20}$$

$$\omega_3 = \omega(1+\lambda) \tag{2.21}$$

$$\omega_4 = \omega(1-\lambda) \tag{2.22}$$

with $\lambda = 0.25$. Since the angles between the wavenumbers are predefined as $\theta_3 = 11.5^o, \theta_4 = -33.6^o$, the DIA only computes a restricted subset of the interactions. Having such a limited set of interactions, good agreement in all regions of the wave spectrum is impossible. The DIA is tuned such that it models the low frequency spectral peak well since this is the dominant energy bearing region of the spectrum. The use of the DIA has important impact both on the other regions of the energy spectrum and on integrated variables such as H_s, the significant wave height, which is the most commonly forecasted variable. However, the main downside of the use of the DIA is a rather poor agreement in the higher frequency regions of the spectrum where the DIA overestimates the negative mid-frequency S_{nl} lobe as well as the positive high frequency variation. Figure 2.5 shows a comparison between the Exact-NL and DIA methods exhibiting this behaviour. To counteract the error introduced by the DIA, wind input and wave dissipation are in turn overestimated in the mid and high frequency regions, respectively, creating a state of energy balance that attempts to reproduce observed values for integrated quantities like H_s, but for which the details of the evolution are strongly biased.

2.2 Time-Stepping Scheme

Wave modeling involves the simulation of a vast variety of phenomena occurring at widely differing time steps. These include the slow variation of water levels with tides (typically $T \sim 12$ hrs for semi-diurnal tides), the propagation of waves from one grid point to the next ($T \sim \delta x/c_p$) to the waves themselves, their wave-wave interactions and their evolution, which depend on much smaller time scales. In order to cope with this, WW3

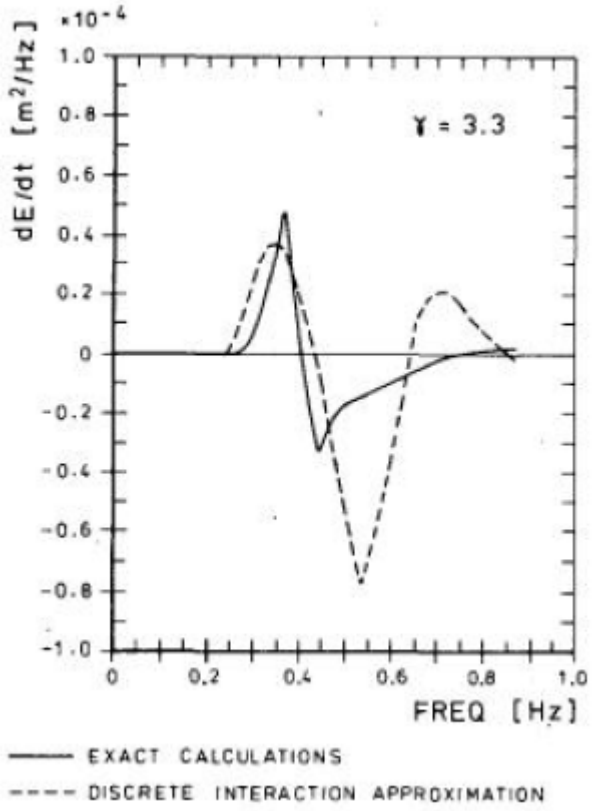

Figure 2.5: Comparison of the one-dimensional non-linear interactions (S_{nl}) as computed by Exact-NL with the results from DIA for a JONSWAP spectrum (*Hasselmann et al.*, 1985).

uses 4 different time steps:

δt_g: a global time step for the propagation of the entire solution in time,

δt_p: the spatial propagation time step,

δt_s: the intra-spectral propagation time step, used for refraction.

δt_S: the source term integration time step.

The last three of the above time steps, which are integer fractions of the global time step, are associated with different aspects of wave evolution as indicated, and are treated individually in the model. If computations required for spatial and intra-spectral propagation should occur for the same time, the order in which they are performed is alternated for

higher numerical accuracy. WW3 therefore performs the following three different time integrations of the wave field:

Firstly, for the spatial propagation, it numerically solves

$$\frac{\partial N}{\partial t} + \frac{\partial}{\partial x}\dot{x}N + \frac{\partial}{\partial y}\dot{y}N = 0, \tag{2.23}$$

where $N = Nc_g^{-1}$, $\dot{x}$ and $\dot{y}$ are the longitudinal and meridional propagation speeds, respectively. Secondly, for the intra-spectral propagation WW3 solves

$$\frac{\partial N}{\partial t} + \frac{\partial}{\partial k}\dot{k}_g N + \frac{\partial}{\partial \theta}\dot{\theta}_g N = 0 \tag{2.24}$$

$$\dot{k}_g = \frac{\partial \sigma}{\partial d}\frac{\mathbf{U}\cdot\nabla_x d}{c_g} - \mathbf{k}\cdot\frac{\partial \mathbf{U}}{\partial s} \tag{2.25}$$

$$\dot{\theta}_g = \dot{\theta} - \frac{cg\tan\phi\cos\theta}{R} \tag{2.26}$$

$$\dot{\theta} = -\frac{1}{k}\left[\frac{\partial \sigma}{\partial d}\frac{\partial d}{\partial m} - \mathbf{k}\cdot\frac{\partial \mathbf{U}}{\partial x}\right] \tag{2.27}$$

where $\mathbf{U}$ is the current velocity, d is the depth and m and s are coordinates parallel and perpendicular to the direction θ. Thirdly, for the source term integration it solves

$$\frac{\partial N}{\partial t} = S \tag{2.28}$$

using the semi-implicit scheme based on

$$\delta N(k,\theta) = \frac{S(k,\theta)}{1 - \epsilon D(k,\theta)\delta t} \tag{2.29}$$

where ϵ is a parameter between 0 and 1 and D is given by

$$D(k,\theta) = \frac{\partial S(k,\theta)}{\partial N(k,\theta)} \tag{2.30}$$

which is called the diagonal term.

2.3 Advection Schemes

To assess the impact of wave propagation on the model results from the two-dimensional experiments, two different propagation (advection) schemes are used in this study. The simplest one is a first order upwind scheme, originally intended for use during development of WW3. A flux formulation is used where the flux between grid points is given by

$$F_{i,-} = [\dot{\phi}_b N_u]^n_{j,l,m}, \tag{2.31}$$

$$\dot{\phi}_b = 0.5(\dot{\phi}_{i-1} + \dot{\phi}_i)_{j,l,m}, \tag{2.32}$$

$$N_u = \begin{cases} N_{i-1} & \text{for } \dot{\phi}_b \geq 0 \\ N_i & \text{for } \dot{\phi}_b < 0, \end{cases} \tag{2.33}$$

where j, l and m are discrete grid counters in λ-, θ- and k-spaces, respectively and n is the discrete time step counter. Here, $\dot{\phi}_b$ is the propagation velocity, or group velocity, at the boundary between the cells considered. The time stepping is thus done using:

$$N^{n+1}_{i,j,l,m} = N^n_{i,j,l,m} + \frac{\Delta t}{\Delta \phi}[F_{i,-} - F_{i,+}] + \frac{\Delta t}{\Delta \lambda}[F_{j,-} - F_{j,+}] \tag{2.34}$$

where Δ t is the propagation time step, $\Delta\ \phi$ and $\Delta\ \lambda$ are latitude and longitude increments, respectively, and the different F_i represent fluxes with the neighbouring cells.

The other propagation scheme used is the QUICKEST scheme developed by *Leonard* (1979) and *Davis and More* (1982) with the ULTIMATE TVD (total variance diminishing) limiter (*Leonard*, 1991). This scheme is third order in accuracy in both space and time.

It is interesting to note that both advection schemes come with significant differences. The first order scheme has a high degree of numerical diffusion, which is absent in the third order scheme. Although this is an advantage in the third-order scheme, the numerical diffusion also smooths out numerical noise, which can limit its impact on wave contours. Examples of wave fields using these schemes are shown in Figure 2.6, which illustrate the effect of the different schemes on the wave fields.

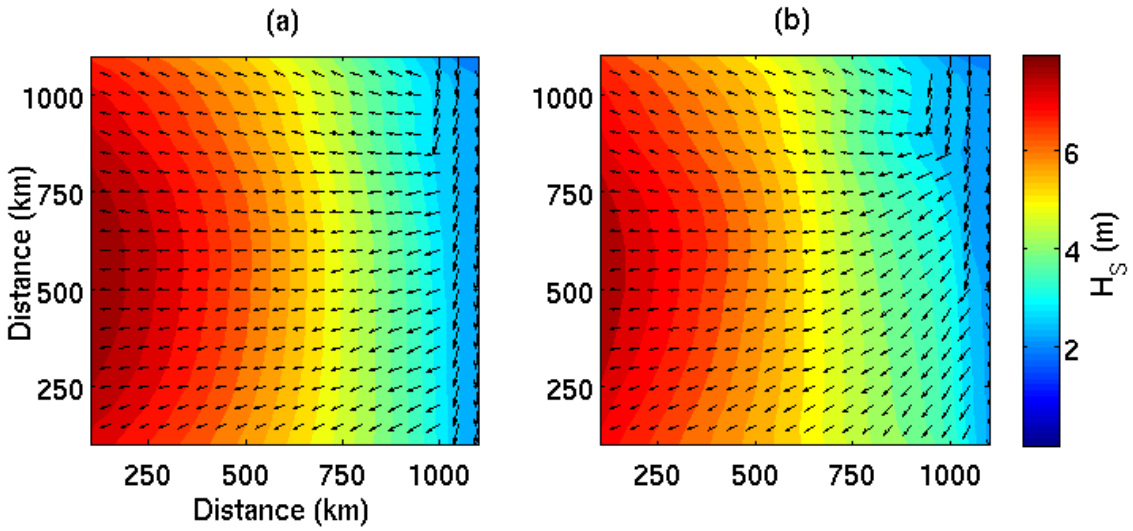

Figure 2.6: Significant wave height fields (in meters) and wave direction (arrows) calculated using (a) the linear propagation scheme and (b) the cubic propagation scheme after 48 hours of winds blowing westward and 5.5 hours of winds blowing South. Note the differences in the North-East corner of the domain.

CHAPTER 3

TWO-SCALE APPROXIMATION

Motivated by the fact that, currently, the most widely used methods of calculation of the non-linear wave-wave interactions (viz. DIA, Exact-NL or WRT) have problems in either efficiency or accuracy, a step forward for numerical ocean wave modelling, especially operational modelling, is to develop a new method which should be fairly accurate and also efficient. With the advances in computing technology and the deployment of computer clusters to satisfy modelling needs, computational resources available today are vastly superior to those which were available more than twenty-five years ago, when the previous methods were designed. As such, new methods can afford to be computationally more expensive than the DIA which, after years of use, is unchallenged in its efficiency. All the potential efficiency gains from symmetry and geometrical integration arguments have already been implemented for the so-called exact integration of the interactions. Therefore, future methods require the application of new approximations in order to offer gains in accuracy compared to the DIA while remaining operationally viable.

Introduced by *Resio and Perrie* (2008), the Two-Scale Approximation (henceforth TSA) represents such a method which can make use of new computing technology. The TSA tries to achieve a better approximation in order to get numerical results that are more faithful to those of the complete integral than the DIA while remaining numerically efficient enough to be used in operational model runs.

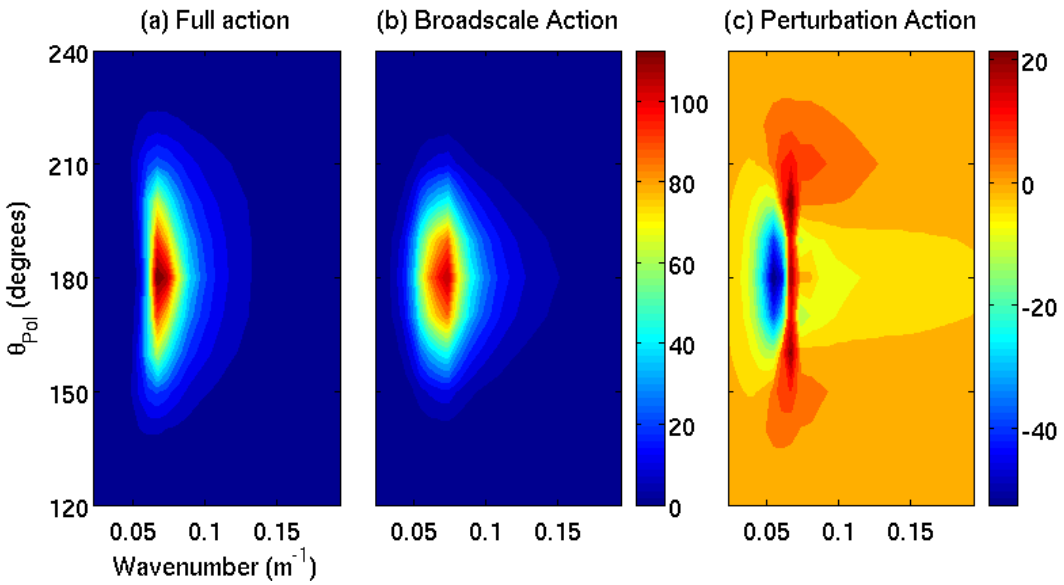

Figure 3.1: Decomposition of (a) the wave action spectrum into (b) the parametric broad-scale shape and (c) its associated perturbation, or local-scale, term. Note: a slight asymmetry in the energy spectrum is made evident in the perturbation term.

3.1 Formulation

The TSA is based on a decomposition of the wave energy spectrum into two parts, one of which follows a predefined parametric shape, and the other is the residual deviation from this shape. The parametric part of the spectrum, also called the broad-scale term, represents the first term of a functional series expansion and should contain most of the energy, especially around the spectral energy peak. The residual part, also called local scale, is the deviation of the spectrum from the parametric fit and contains the remaining energy. For classical JONSWAP wind sea, the parametric broad-scale term should provide a good representation of most of the spectrum, and the local scale term should be small. However, in the case of complex sea states, we will show that the local scale term becomes more prominent. Figure 3.1 shows an example of the decomposition for a spectrum generated by an easterly wind blowing for forty-eight hours, followed by a half-hour of northerly wind.

In the TSA formulation, in order to calculate the wave-wave interactions, only a subset of all possible interactions are retained. The original action component in Eq.2.17 is cubic

in wave action and contains two terms; the first uses the product of wave numbers one and three, the second uses their difference. By decomposing the spectrum into two scales, broad-scale and local-scale, each term of the cubic component becomes eight terms (2^3), yielding:

$$\begin{aligned} N^3 = \quad & \hat{n}_1\hat{n}_3(\hat{n}_4 - \hat{n}_2) + \hat{n}_2\hat{n}_4(\hat{n}_3 - \hat{n}_1) + \\ & n'_1n'_3(n'_4 - n'_2) + n'_2n'_4(n'_3 - n'_1) + \\ & \hat{n}_1\hat{n}_3(n'_4 - n'_2) + \hat{n}_2\hat{n}_4(n'_3 - n'_1) + \\ & n'_1n'_3(\hat{n}_4 - \hat{n}_2) + n'_2n'_4(\hat{n}_3 - \hat{n}_1) + \\ & \hat{n}_1n'_3(\hat{n}_4 - \hat{n}_2) + \hat{n}_2n'_4(\hat{n}_3 - \hat{n}_1) + \\ & n'_1\hat{n}_3(\hat{n}_4 - \hat{n}_2) + n'_2\hat{n}_4(\hat{n}_3 - \hat{n}_1) + \\ & \hat{n}_1n'_3(n'_4 - n'_2) + \hat{n}_2n'_4(n'_3 - n'_1) + \\ & n'_1\hat{n}_3(n'_4 - n'_2) + n'_2\hat{n}_4(n'_3 - n'_1) \end{aligned} \tag{3.1}$$

where hats(ˆ) represent broad-scale components and primes(´) represent the local-scale perturbations. The first two terms in Eq.3.1 include self interactions in the broad-scale components on the first line, which can be obtained from shape characteristics and scaling properties of non-linear transfer. Those form the broad-scale's contribution to S_{nl} and are denoted B. The other terms are the cross-interactions between local- and broad-scale terms. The argument is made by *Resio and Perrie* (2008) that there should be no, or very little, correlation between terms involving n'_2 and n'_4 along with their product and difference. Their integral should be much smaller than that of the other terms in the expansion since they are expected to oscillate between positive and negative contributions. Keeping only the cross-interactions which strongly depend on the dominant broad-scale terms results in a new cubic term. The approximation to the cubic interaction term can be defined as:

$$N^3 \approx B + N^3_* \tag{3.2}$$

where

$$B = \hat{n}_1\hat{n}_3(\hat{n}_4 - \hat{n}_2) + \hat{n}_2\hat{n}_4(\hat{n}_3 - \hat{n}_1) \tag{3.3}$$

$$\begin{aligned} N_*^3 &= \hat{n}_2\hat{n}_4(n_3' - n_1') + n_1'n_3'(\hat{n}_4 - \hat{n}_2) \\ &+ \hat{n}_1n_3'(\hat{n}_4 - \hat{n}_2) + n_1'\hat{n}_3(\hat{n}_4 - \hat{n}_2). \end{aligned} \tag{3.4}$$

This choice of terms allows to reduce the integral from six to two dimensions. Indeed, the integral still covers the whole two-dimensional spectrum of the third wavenumber (k_3) but keeping the broad-scale contribution from wave number two ($\hat{n}_2$) and four ($\hat{n}_4$) does not force the integral to remain six-dimensional. The wave action for these spectral components only comes from the broad-scale, and thus only depends on the same parameters as the broad-scale action for wave numbers one ($\hat{n}_1$) and three ($\hat{n}_3$). The broad-scale components can all be precomputed using the broad-scale and retrieved when necessary, saving valuable computational time. The results from the two different components, B and N_*^3, can be summed up to produce the two-scale approximation to the non-linear wave-wave interactions described by Eq.2.17, the TSA, defined as:

$$\frac{\partial n_1}{\partial t} = \int\int\int (B + N_*^3)C|\frac{\partial W}{\partial n}|^{-1} ds k_3 d\theta_3 dk_3 \tag{3.5}$$

where ds is a coordinate defined along the spectral space which satisfies the interaction constraints (Eq.2.18-2.19) while C and $|\frac{\partial W}{\partial n}|^{-1}$ are the coupling and gradient terms, equivalent to G in Eq.2.17. The reduction of the problem to two parts, one of which has a simpler parametric solution, allows for much faster calculations which still consider the wave spectrum for all spectral space, instead of a subset.

The TSA formulation given by Eq.3.5 can be rewritten to take advantage of the potentially precomputed quantities as

$$\begin{aligned} \frac{\partial n_1}{\partial t} &= (\frac{\beta}{\beta_0})^3 B_i \\ &+ (\frac{f_{p0}}{f_p}) \left\langle \begin{array}{c} (\frac{\beta}{\beta_0}) \int\int (\hat{n}_1 n_3' + n_1'\hat{n}_3 + n_1'n_3')\Lambda_d(\hat{n}_2 - \hat{n}_4, k_1, k_3, \theta_3, x_1, ..., x_n) k_3 d\theta_3 dk_3 \\ +(\frac{\beta}{\beta_0})^2 \int\int (n_1' - n_3'\Lambda_p(\hat{n}_2\hat{n}_4, k_1, k_3, \theta_3, x_1, ..., x_n) k_3 d\theta_3 dk_3 \end{array} \right\rangle \end{aligned} \tag{3.6}$$

where B_i is the integral of the broad-scale contribution from equation 3.5 and the remaining integral makes use of the precomputed variables Λ_p and Λ_d:

$$\Lambda_d(\hat{n}_2 - \hat{n}_4, k_1, k_3, \theta_3, x_1, ..., x_n) = \oint C|\frac{\partial W}{\partial n}|^{-1}(\hat{n}_4 - \hat{n}_2)ds \quad (3.7)$$

$$\Lambda_p(\hat{n}_2\hat{n}_4, k_1, k_3, \theta_3, x_1, ..., x_n) = \oint C|\frac{\partial W}{\partial n}|^{-1}(\hat{n}_4\hat{n}_2)ds. \quad (3.8)$$

The integration along the locus of points which satisfy the wave-wave interaction conditions (Eq.2.18-2.19) is then only dependant on the broad-scale parameters. In this formulation, the integral for the TSA thus has only 2 dimensions in spectral space, rather than 6 dimensions for Exact-NL, the exact integral, or 3 dimensions for the WRT method. This approach cannot be reproduced by geometric methods used by DIA or GMD because they only consider a fixed number of locations in spectral space when approximating the non-linear wave-wave interactions. The ability of the TSA to consider the whole spectral space, while intrinsically more computationally expensive than the DIA, also allows for an increase in accuracy that is beyond the reach of other simpler methods.

The contributions from both the broad- and local-scale parts of the approximation are shown in Figure 3.2, for the spectrum shown in Figure 3.1a. The shape of the broadscale non-linear interactions in Figure 3.2a is similar to what should be expected; a positive lobe at low wavenumber and negative lobe for higher wavenumbers. This represents a flux of energy from higher frequencies to lower ones, or the evolution of wind waves into swell. The perturbation, which is essentially a correction term, amplifies the positive peak while reducing the amplitude of the negative and side lobes.

The sum of the two interaction components shown in Figure 3.2 yields the two-scale approximation to the non-linear interactions, shown in Figure 3.3b, with the interactions from the WRT method shown in panel a. Figure 3.3 illustrates that, in areas close to the spectral peak and where the broad-scale covers most of the action, the approximation holds very well. Further from the peak, where the fit is not as accurate, the approximation does

not have the same skill. Since the shape of the broad-scale and the exactitude of the fit are entirely up to the fitting procedure, the TSA can theoretically hold in any situation. In this work, a simple symmetric spectral shape with a single peak is used.

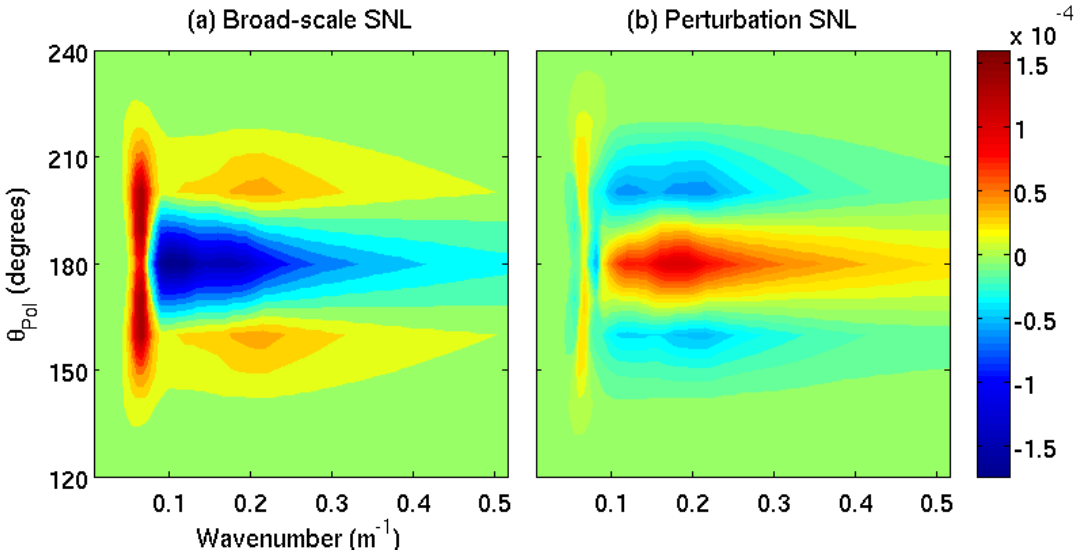

Figure 3.2: Contributions to the non-linear interactions from (a) the broad-scale and (b) the perturbation, or local-scale, terms shown in Figure 3.1b and c.

3.2 Implementation

WW3 already includes modules for the computation of non-linear wave-wave interactions using the DIA and the WRT method. Because TSA is an approximation based on modifications of the exact calculations, the simplest approach for its implementation inside the model is to modify the code used for the WRT method. As our aim is to evaluate the accuracy of the TSA, we overlook the time saving potential of TSA and focus solely on obtaining a modified module which is able to calculate the non-linear wave-wave interactions using the TSA in a mathematically correct way.

In order to use the TSA inside WW3, three modifications are required: the addition of an algorithm to divide the wave energy spectrum into a parametric broad-scale part with its associated perturbation local-scale term; alteration of the code in order to calculate the TSA for the non-linear wave-wave interactions; and a derivation of the TSA diagonal terms as defined in 2.30.

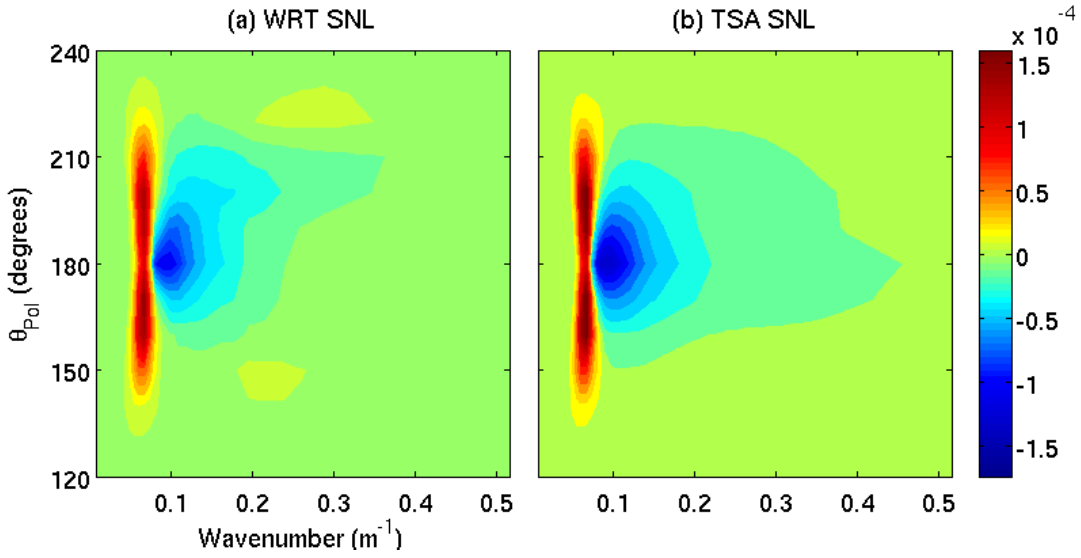

Figure 3.3: Non-linear interactions as calculated by (a) the WRT method and (b) the TSA for the input spectrum shown in Figure 3.1a. Asymmetry in the local-scale leads to asymmetry in the non-linear interactions.

3.2.1 Creation of the Two Energy Scales

The energy partition is performed in a subroutine called optsa in the non-linear interactions computation module mod_xnl4v5.f90. This subroutine uses peak frequency, group velocity as well as one- and two-dimensional energy to calculate the two scales necessary for the calculation of TSA for the interactions.

The wave spectrum partition is performed on the one-dimensional energy spectrum obtained from the integration of the two-dimensional energy spectrum over directions. An example of the one-dimensional spectrum is shown in Figure 3.4 for the two-dimensional spectrum of Figure 3.1. With the peak identified, the energy at that frequency is used to find the dominant direction of the main component of the waves. It is common in wave modelling to approximate the wave spectra by using the separable form:

$$F(f,\theta) \approx F_{1D}(f)D(\theta) \tag{3.9}$$

where F is the two-dimensional wave spectrum and $F_{1D}(f)$ is the one-dimensional energy spectrum obtained by integrating the two-dimensional spectrum over directions. The spectral spreading function, $D(\theta)$, is usually of the form

$$D(\theta) = \frac{cos^m(\theta)}{\int_{-\pi/2}^{\pi/2} cos^m(\theta)d\theta} \tag{3.10}$$

and is used to spread the energy contained in F_{1D} over spectral directions 90 degrees to the left and right of the main spectral direction. A higher spreading power (m) confines the energy closely around the peak direction while a lower value corresponds to energy spreading over multiple directions. In this implementation of the TSA, sixteen powers are considered for the parametric form, giving the different spreading functions shown in Figure 3.5. The spreading power to be used in the decomposition is obtained by comparing the peak energy divided by the energy integral of the spectrum at that frequency to the cosine normalization that would correspond to the different spreading powers, as shown in Figure 3.6. Using this power, the energy of the one-dimensional fit will be spread over directions in order to obtain the two-dimensional fit, shown for the peak frequency of the

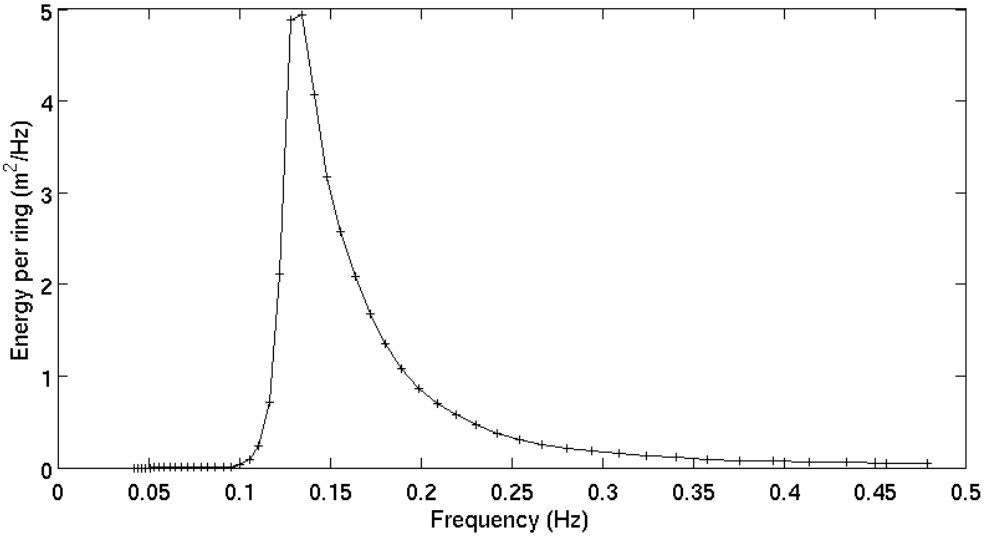

Figure 3.4: One-dimensional wave energy spectrum.

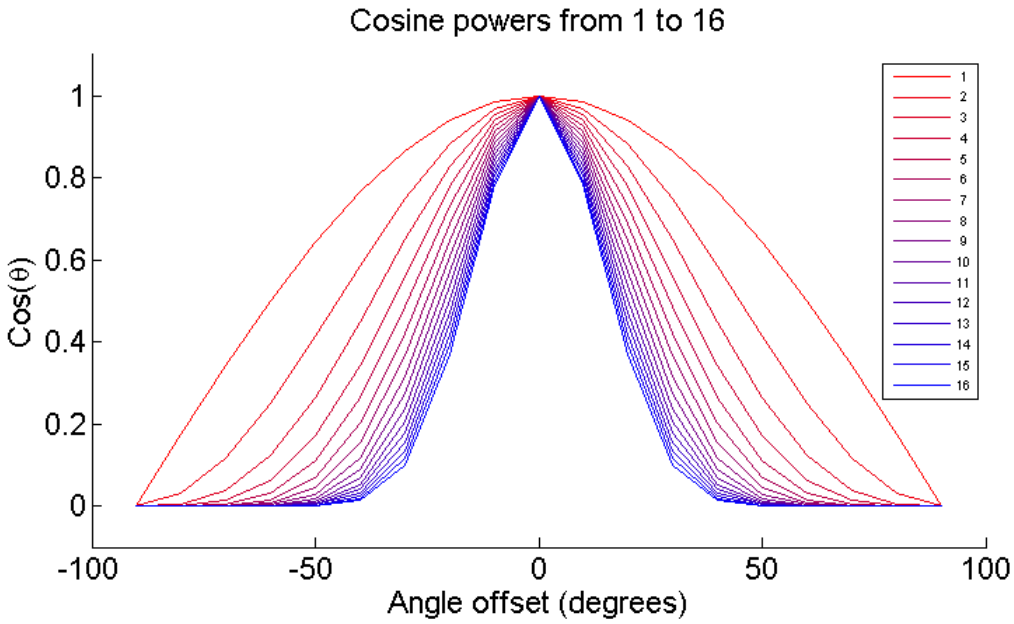

Figure 3.5: Spreading powers considered in the creation of the broad-scale term for the energy spectrum.

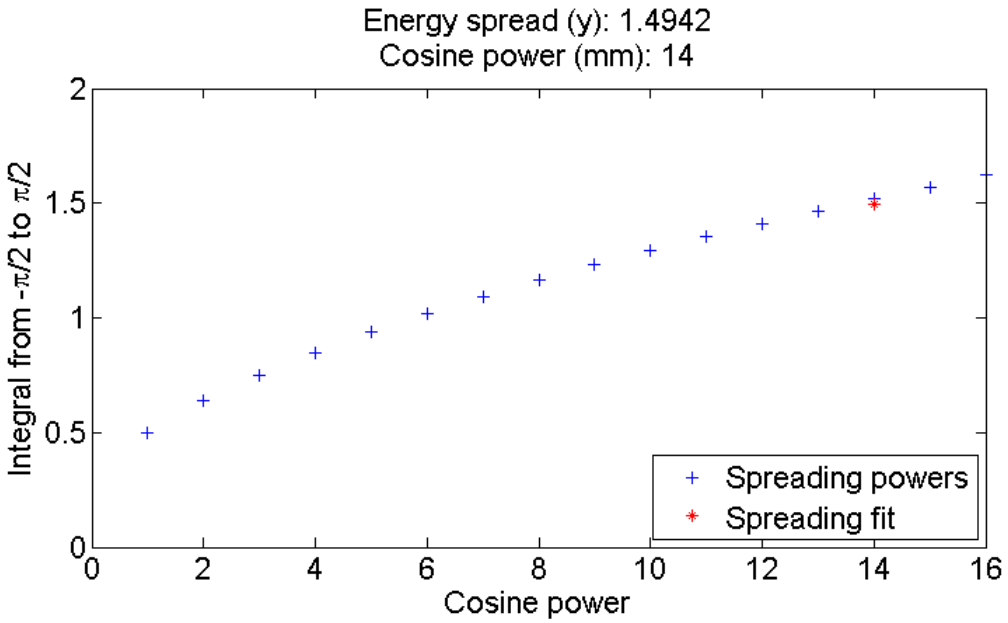

Figure 3.6: Fit of the ratio of peak energy to energy integral by comparison with the integral of cosines of the various spreading powers.

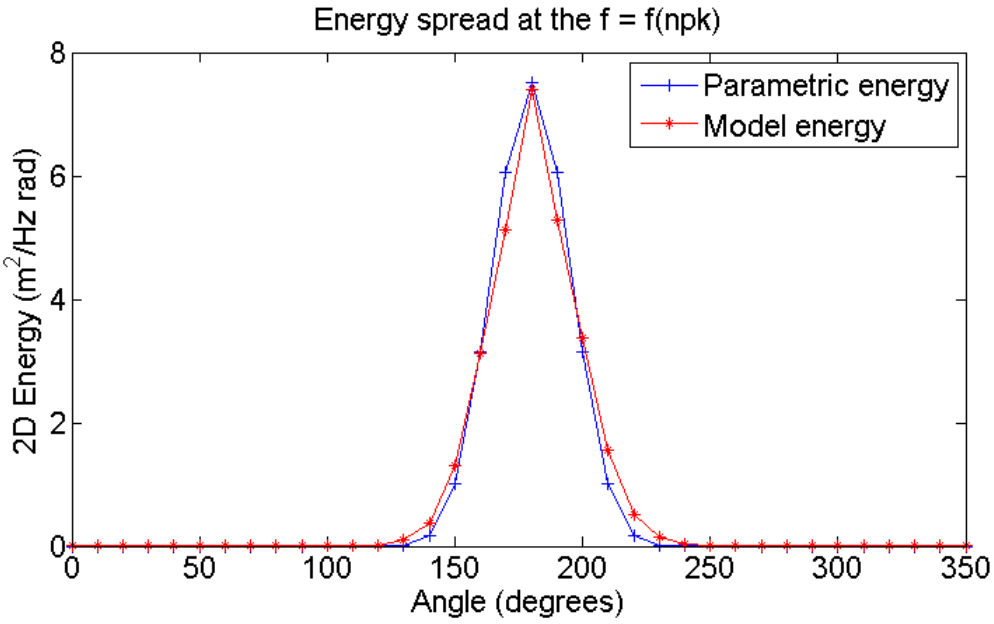

Figure 3.7: Comparison of the model energy spectrum and the spectral spreading obtained.

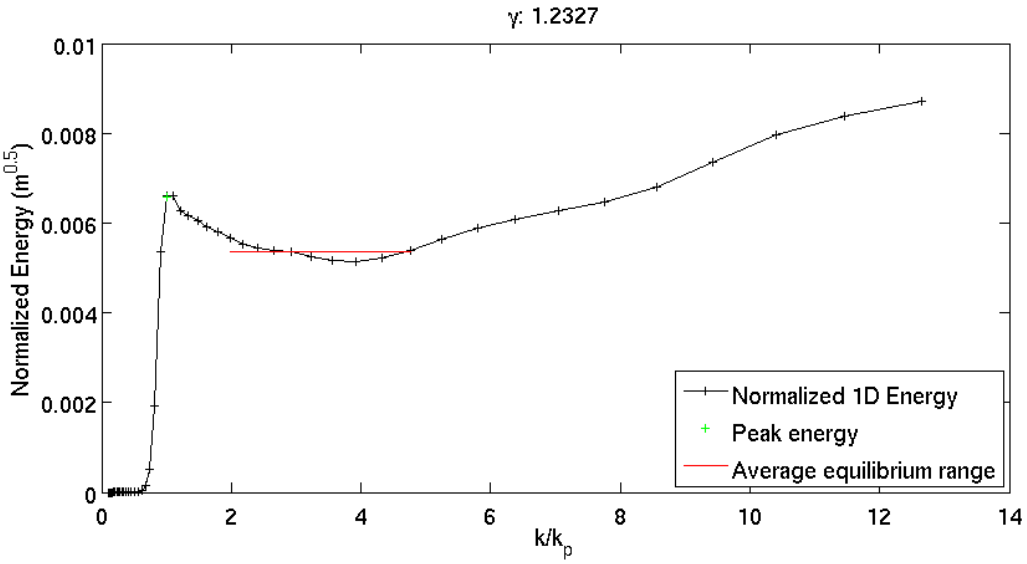

Figure 3.8: Normalized energy and fitting parameters used for the generation of the one-dimensional energy spectrum.

spectrum in Figure 3.7.

After the spreading power is obtained, the one-dimensional energy spectrum fit is determined. In order to limit the number of parameters used to store the pre-computed variables, the energy fit is done with a predetermined shape which relies solely on γ, the ratio of energy at the peak of the normalized spectrum to the average of the energy content in the equilibrium range. In the literature, this region of the spectrum corresponds to frequencies that are about 2.5$\sim$3.5 times larger than the peak frequency, but in the implementation the factors used are 1.36 and 2.27. Normalized energy, equilibrium range and the fitting parameter can be seen in Figure 3.8.

The parametric one-dimensional energy spectrum is generated in accordance to a predefined shape and transformed to action, to give the broad-scale spectrum in Figure 3.9. The parametric spectrum is then convoluted with the spreading function in order to obtain the two-dimensional parametric, or broad-scale, action (Figure 3.1b) and the difference with the model's action is stored as the perturbation, or local-scale term (Figure 3.1c).

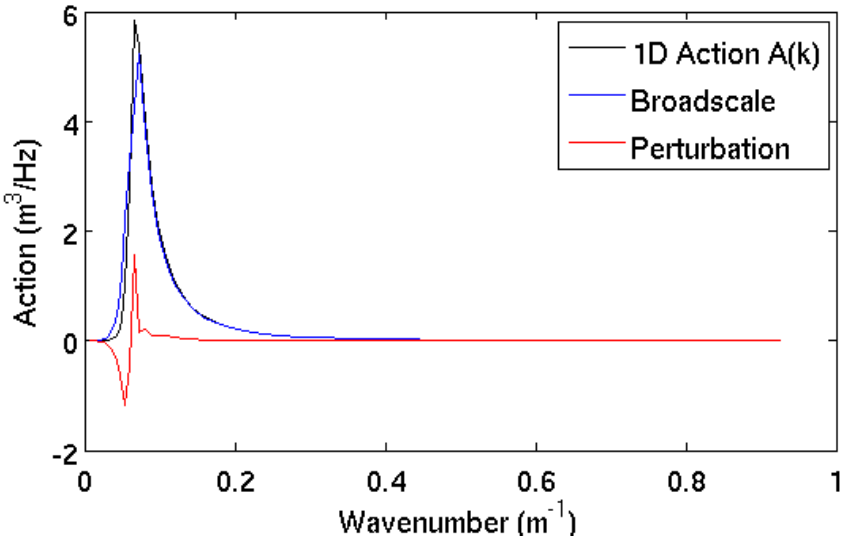

Figure 3.9: One-dimensional action spectrum, parametric fit and perturbation.

3.2.2 Calculation of the Non-Linear Wave-Wave Interactions

TSA's calculation of non-linear wave-wave interactions is performed in subroutine q_t13v4T which is added to the interactions module mod_xnl4v5.f90. Since there are certain conditions under which the TSA cannot be used, such as when the spectral peak is at very high frequencies forcing the equilibrium range outside of the modelled spectral space, the original WRT subroutine was retained as a contingency. Because the TSA integral is computed subject to the same constraints as WRT, all the geometry of the wave-wave interactions is exactly the same as for the WRT method.

3.2.3 Derivation and Calculation of the Diagonal Terms

Diagonal terms are defined for all frequencies and directions by Eq.2.30 and are required in Eq.2.29 for the time integration of source terms. Although it is relatively straightforward to take the derivative of Eq.2.17 with respect to action density, it becomes more complicated when confronted with the interaction integral as defined for the TSA, since terms are defined as functions of both scales, not the total action.

However, the broad-scale and perturbation interactions can be recombined together to obtain the total interactions as calculated using the TSA:

$$\begin{aligned} N^3_{tsa} &= (\hat{n}_1 + n'_1)(\hat{n}_3 + n'_3)(\hat{n}_4 - \hat{n}_2) \\ &+ \hat{n}_2\hat{n}_4(\hat{n}_3 + n'_3 - \hat{n}_1 - n'_1). \end{aligned} \tag{3.11}$$

Let $n_1 = \hat{n_1} + n'_1$, then the cubic term of the non-linear interactions for the TSA can be re-written as

$$\begin{aligned} N^3_{tsa} &= n_1(\hat{n}_3 + n'_3)(\hat{n}_4 - \hat{n}_2) \\ &+ \hat{n}_2\hat{n}_4(\hat{n}_3 + n'_3 - n_1) \end{aligned} \tag{3.12}$$

in which case the diagonal term, for action $n_1 = N(k_1, \theta_1)$, is given by:

$$\begin{aligned} D(k_1, \theta_1) &= \frac{\partial S(k_1, \theta_1)}{\partial N(k_1, \theta_1)} \\ &= \int\int\int ((\hat{n}_3 + n'_3)(\hat{n}_4 - \hat{n}_2) - \hat{n}_2\hat{n}_4)C|\frac{\partial W}{\partial n}|^{-1} ds k_3 d\theta_3 dk_3. \end{aligned} \tag{3.13}$$

Figure 3.10 compares the diagonal terms calculated by the WRT and TSA methods. The action spectrum used as the input for the computation of the diagonal term by both methods is the slightly asymmetric spectrum shown in Figure 3.1a. This creates asymmetries in the diagonal terms which are significant in the WRT diagonal terms of Figure 3.10a. The TSA diagonal terms also show asymmetries, although they are much less significant than those observed in the WRT diagonal terms. The overall shapes, with a stronly negative area for high wavenumbers along $\theta = 180^o$ and a weaker negative area along $\theta = 360^o$, are also similar in the two methods.

The diagonal terms can be further divided into two parts, with one calculated using the broad-scale, D_B and the other obtained from the perturbation term D_P, in order to speed up computations. Here, D_B is solely dependant on the broad scale and can be entirely pre-computed using

$$D_B(k_1,\theta_1) = \int\int\int (\hat{n}_3(\hat{n}_4 - \hat{n}_2) - \hat{n}_2\hat{n}_4)C|\frac{\partial W}{\partial n}|^{-1} ds k_3 d\theta_3 dk_3. \tag{3.14}$$

The diagonal term associated with the perturbation is then

$$D_P(k_1,\theta_1) = \int\int n_3' \Lambda_d(\hat{n}_2 - \hat{n}_4, k_1, k_3, \theta_3, x_1, ..., x_n) k_3 d\theta_3 dk_3 \tag{3.15}$$

which uses the same pre-computed variable, Λ_d, as defined in equation 3.7. The respective contributions of these two components to the diagonal term is shown in Figure 3.11. The decomposition into the contributions from the two different scales explains the discrepancy between the WRT and TSA diagonal terms of Figure 3.10. Diagonal terms are mostly dependant on the broad-scale, which in this implementation is symmetric by construction. The broad-scale diagonal terms are therefore symmetric by construction as well, as shown in Figure 3.11a. The perturbation, which carries the asymmetry of the spectrum, cannot entirely compensate in this case, yielding the mostly symmetric total diagonal terms of Figure 3.10b.

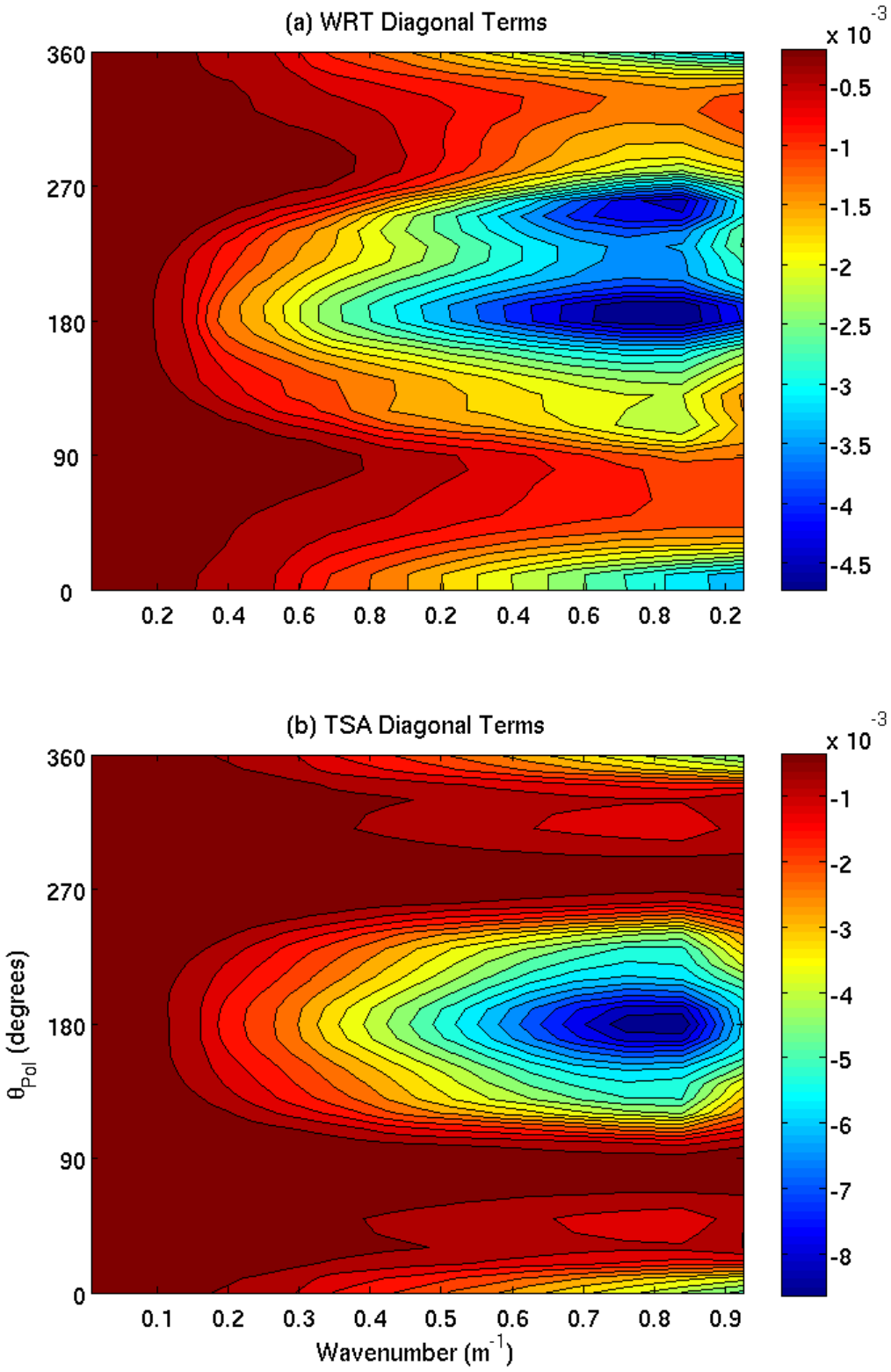

Figure 3.10: Diagonal terms as calculated by (a) the WRT method and (b) the TSA for the input spectrum shown in Figure 3.1a.

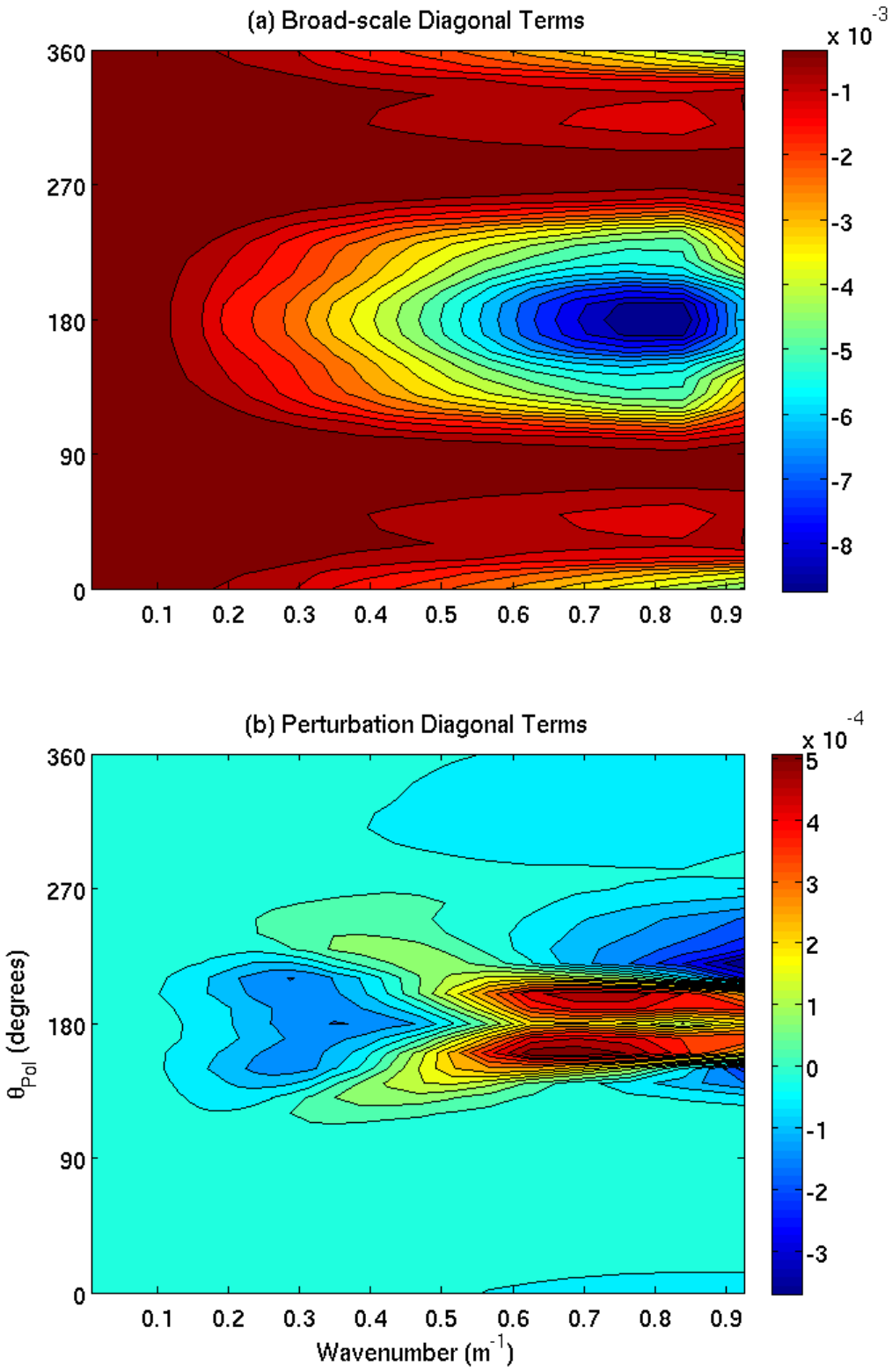

Figure 3.11: Diagonal term components from (a) the broad-scale and (b) the perturbation for the TSA diagonal term shown in Figure 3.10.

CHAPTER 4

ONE POINT EXPERIMENTS

Wave evolution in ocean wave models can be affected by several factors described earlier. In order to limit the bulk of the wave dynamics to the balance of source terms, several one-point numerical experiments are conducted to assess the performance of the new method. The first tests of the TSA are performed on a simple domain consisting of only nine points shown in Figure 4.1. Of these, only the centre point is active water; the surrounding eight are land boundary points. Unlike circulation models in which land masses are considered to be a closed boundary, wave models allow waves to dissipate as they reach the shore. A sea point surrounded by land points can thus only lose energy to the boundaries. This setup allows us to consider local seas exclusively as no waves are coming from any neighbouring grid cell. The energy spectrum stabilizes (reaches dynamic equilibrium) when the contributions of all source terms balance with energy propagation. The one point experiments were performed using the DIA, TSA and WRT methods for calculation of non-linear interactions, as well as the two different propagation schemes described in section 2.3.

4.1 Turning Winds

The first experiment is the one-point equivalent of the seventh test case described in *SWAMP* (1985). In this experiment, wind blows in one direction until saturation is reached, then the wind rotates by 90^o while keeping the same strength. This can be thought of as

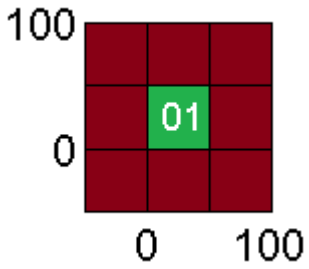

Figure 4.1: Model domain used for the one point experiments. The green point is the model's active output point and red points are land points.

being similar to the passage of a meteorological front over a modelled domain, which can cause a rapid rotation in winds. In our case, 20 m/s easterly winds blow for 48 hours, followed by 72 hours of northerly winds of the same speed. The durations of the two periods of winds are longer than required to reach dynamic equilibrium. These simulations were quick to perform, the run time for the one point models on a single processor is less than two hours. Once the equilibrium is reached, the wave energy spectrum simply stays constant. Such long time integrations thus allowed us to check the model stability.

4.1.1 Growth Curves and One-Dimensional Evolution

The main spectrally integrated parameters considered for wave growth are the significant wave height (H_s) and the peak frequency (f_p). These two variables define the energy content of the wave spectrum and its location in spectral space. In the growth curves for this experiment, shown in Figure 4.2, the difference between using the two advection schemes for a given non-linear interaction formulation is small for both H_s and f_p in comparison to the difference caused by the change of non-linear interaction calculation method. The similarity in the growth curves using different advection schemes for the same non-linear interaction method indicates that the impact of the formulations of non-linear wave-wave interactions on wave evolution is larger than that of the propagation schemes used in this experiment.

Figure 4.2 shows that dips in wave height and peak frequency occur after 48 hours, when the wind turns from easterly to northerly. The wind shift causes dissipation of the

waves which have a component going against the wind. The change in wind direction also breaks the dynamic equilibrium between source terms, which had allowed the significant wave height to grow to close to 3 meters. Propagation and dissipation continue to have their impacts on spectral evolution and, with turning winds, waves become decoupled from the wind, forming swell that propagates out of the domain. Meanwhile, new wind waves are generated, which eventually reach similar levels for wave height and peak frequency as the previous equilibrium. Everything after the transition tends to be similar to what was before the winds turned, only rotated by 90^o.

The growth curves calculated by the WRT and TSA methods show very good agreement, especially for the peak frequency, for which the two methods are almost indistinguishable. Large differences in the significant wave height growth curves shown in Figure 4.2a can be explained by the fact that S_{in} and S_{ds} have both been tuned to observed growth curves and for the DIA and WRT while similar tuning has not been performed yet for the TSA. In wave modelling studies, the dissipation term S_{ds} is typically used as a closure term designed to be tuned so that given formulations for other source terms result in appropriate model behaviour with respect to growth curve observations. This is the case with the wave dissipation parameterization used here, which has been tuned for both the WRT and DIA methods. As the TSA is relatively close to the exact integration represented by the WRT method, the tuning performed for the WRT is also used for the TSA. However, it is to be expected from these results that a retuning of the dissipation in order to weaken the term would allow the TSA runs to generate higher waves and remain close to the WRT H_s curve. The shape of the TSA curves however, are similar to the WRT curves, which is very encouraging.

Figure 4.3 demonstrates that the evolution of the one dimensional energy spectra, the energy spectrum integrated over directions (F_{1D}), is consistent with the evolution of the integrated parameters of Figure 4.2. Since both the first and third order propagation schemes provide essentially identical results, only the first order scheme is shown here. The spectra produced by the WRT (Figure 4.3a) and the TSA (Figure 4.3b) methods are in

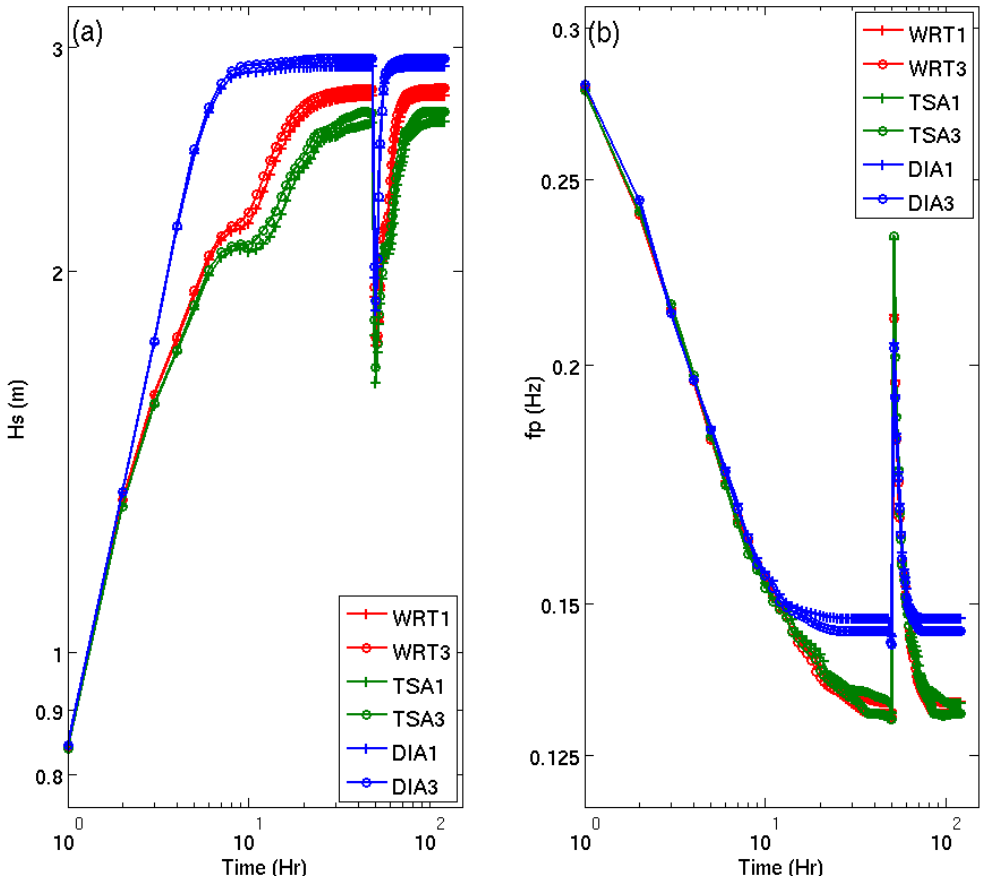

Figure 4.2: Growth curves for the turning wind experiment showing (a) the significant wave height and (b) the peak frequency. Different formulations for non-linear interactions are marked by different colours, while the different propagation schemes (first or third order) are marked by different symbols.

good agreement. Their shape and distribution along the frequency axis are similar, whereas the DIA (Figure 4.3c) results show spectra which are much broader.

The large differences in peak frequencies shown in Figure 4.2b can also be seen in Figure 4.3. The high energy regions of both the WRT and TSA results occur at the same frequencies, whereas the spectra for the DIA peak at higher frequencies and also stabilize earlier. The energy content values, summarized by H_s in Figure 4.2a, are also visible here. While the WRT and DIA spectra show similar values for the peak energy, the wider spread for the DIA explains its larger overall energy content and thus higher waves. The shape of the TSA spectra is very much like that of the spectra obtained using the WRT, being

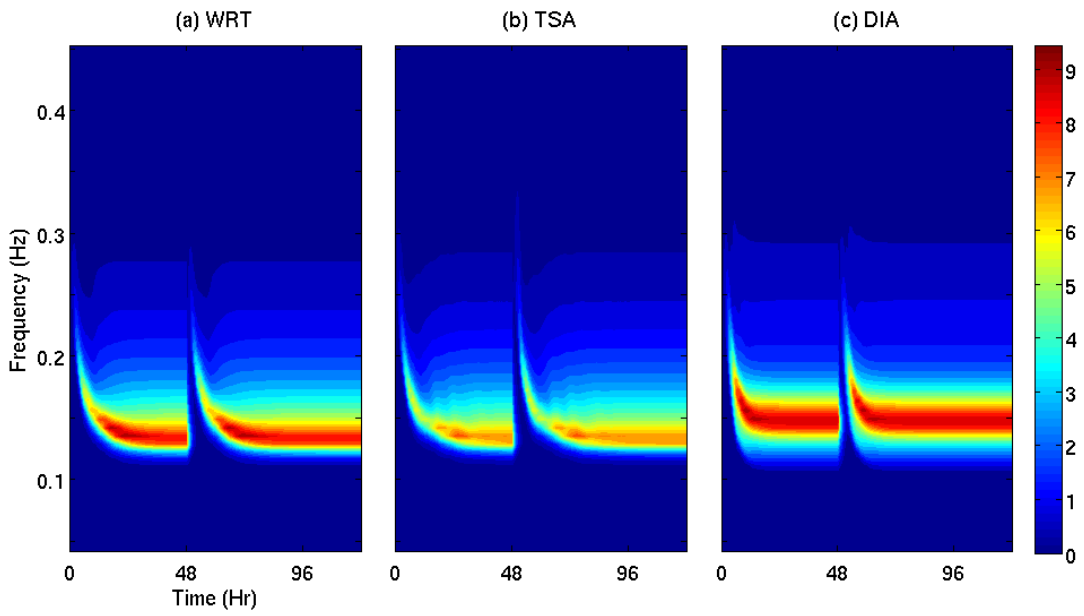

Figure 4.3: Evolution of one-dimensional energy spectrum in m^2Hz^{-1} obtained from model results using (a) the WRT, (b) the TSA and (c) the DIA with the first order propagation scheme.

narrow during wave growth and thicker upon reaching equilibrium. This is especially easy to see with the curvature in the high frequency region of Figures 4.3a and 4.3b during the first twelve hours and between hours 48 and 60. The spectral distribution of energy of the WRT and TSA results are very close. The lower significant wave heights of the results obtained using the TSA shown in Figure 4.2a therefore does not come from a discrepancy in a specific area of the spectrum but from the overall lower energy levels. Spectral shape being harder to reproduce than intensity, this is an encouraging result.

The other interesting feature shown in Figure 4.3 is the weak oscillation in the energy spectra as the waves reach equilibrium. This is particularly visible in the TSA results (Figure 4.3b), between the sixteenth and thirtieth hours, and again for a similar period as the waves are re-equilibrating with the northerly wind. A similar phenomenon, albeit much shorter lived and restricted to the peak area can be seen for both the WRT (Figure 4.3a) and DIA (Figure 4.3c) results. This represents a brief period after which the different source terms re-balance one another. The oscillations in the TSA last longer and are observed on

a wider range of frequencies.

The evolution of one-dimensional non-linear wave-wave interactions, the non-linear interactions equivalent of F_{1D} shown in Figure 4.4, shares very similar main features with one-dimensional energy spectra (Figure 4.3). Once the stable solution is reached, the positive peak of the interactions for both the WRT method and the TSA method are centred around the same frequencies while the DIA peaks at slightly higher frequencies. This difference in the final position of the positive contributions of the interactions plays a major role in the difference in the locations of the energy peak, as non-linear interactions are responsible for the transfer of energy towards lower frequencies. The intensity of the interactions calculated using the TSA is also weaker than that calculated by the WRT method because the energy spectrum peaks at a lower maximum energy for the TSA. The shapes of non-linear wave-wave interactions shown in Figure 4.4 are very similar for the three methods, with the negative lobes of the TSA being slightly deeper during wave growth and extending to higher frequencies upon reaching equilibrium. The DIA shows broader positive peaks similar to the corresponding energy, as well as a narrow band of more negative interactions around 0.17Hz which is not observed in either the WRT and TSA. The oscillations found in Figure 4.3 are also present in the positive peak of the non-linear interactions, particularly for TSA results.

A closer inspection of the evolution of both the one-dimensional energy and non-linear interactions shown in Figure 4.5 reveals that the oscillations in non-linear interactions lead the oscillations in energy spectra. The broadening of the non-linear interactions term in frequencies is maximal at hours 15 and 22 of the simulation while the energy spectra broaden at hours 17 and 24. The amplitude of the oscillations is larger for the runs using the TSA than in the runs using the other two methods due to the TSA's approach to the calculation of the non-linear interactions. The higher amplitude can be explained by the two-step process used for the TSA: the decomposition of the energy spectrum into two scales, then the calculation of the interactions, neglecting part of the energy. This means that the TSA calculates its interactions based on a partial representation of the energy

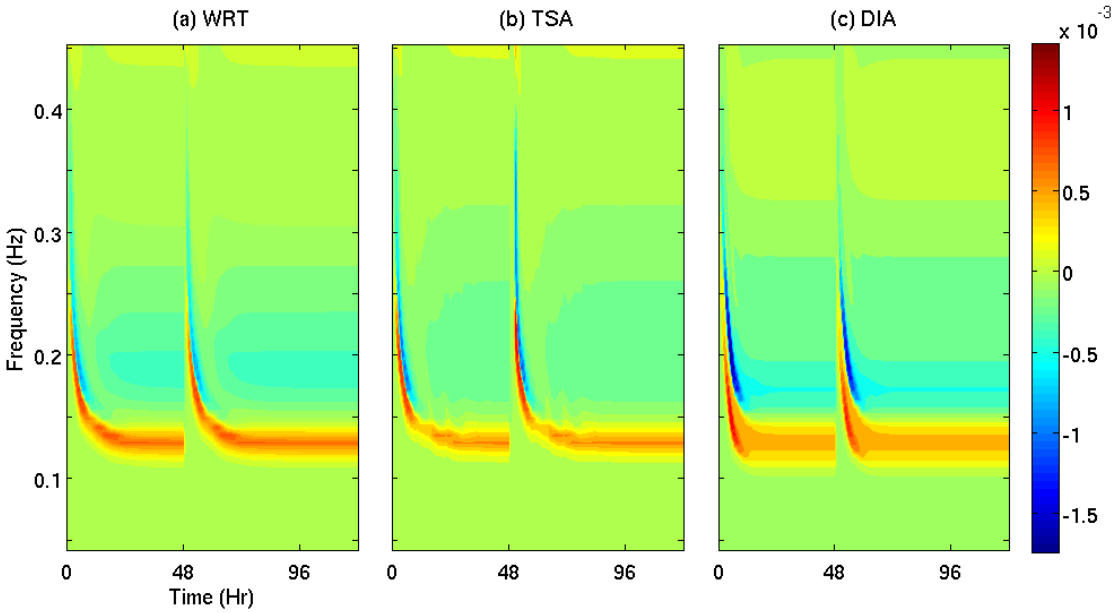

Figure 4.4: Evolution of the one-dimensional non-linear interactions in m^2 for (a) the WRT, (b) the TSA and (c) the DIA obtained using the first order propagation scheme.

spectrum which is updated every time step, making convergence to the equilibrium solution more complex. However, it does converge towards a two-dimensional energy spectrum which is very similar to the one obtained with the WRT.

4.1.2 Two-Dimensional Spectral Evolution

The spectra obtained by the three methods after the first forty-eight hours are shown in Figure 4.6 and the corresponding non-linear interactions are shown in Figure 4.7. As with the one-dimensional spectra, only the spectra for the experiment with the first order propagation scheme are presented. The two-dimensional wave spectra generated in the wave growth part of this simulation using the TSA method show remarkable agreement with those obtained using the WRT method. Spectral shape and peak location produced by the TSA and WRT are very similar but peak energy is underestimated in the TSA results.

The equilibrium energy spectra obtained using the WRT and the TSA methods share a number of similarities. The location of the peak energy, the bimodal distribution of energy at higher frequencies (two maxima for different directions at a given frequency)

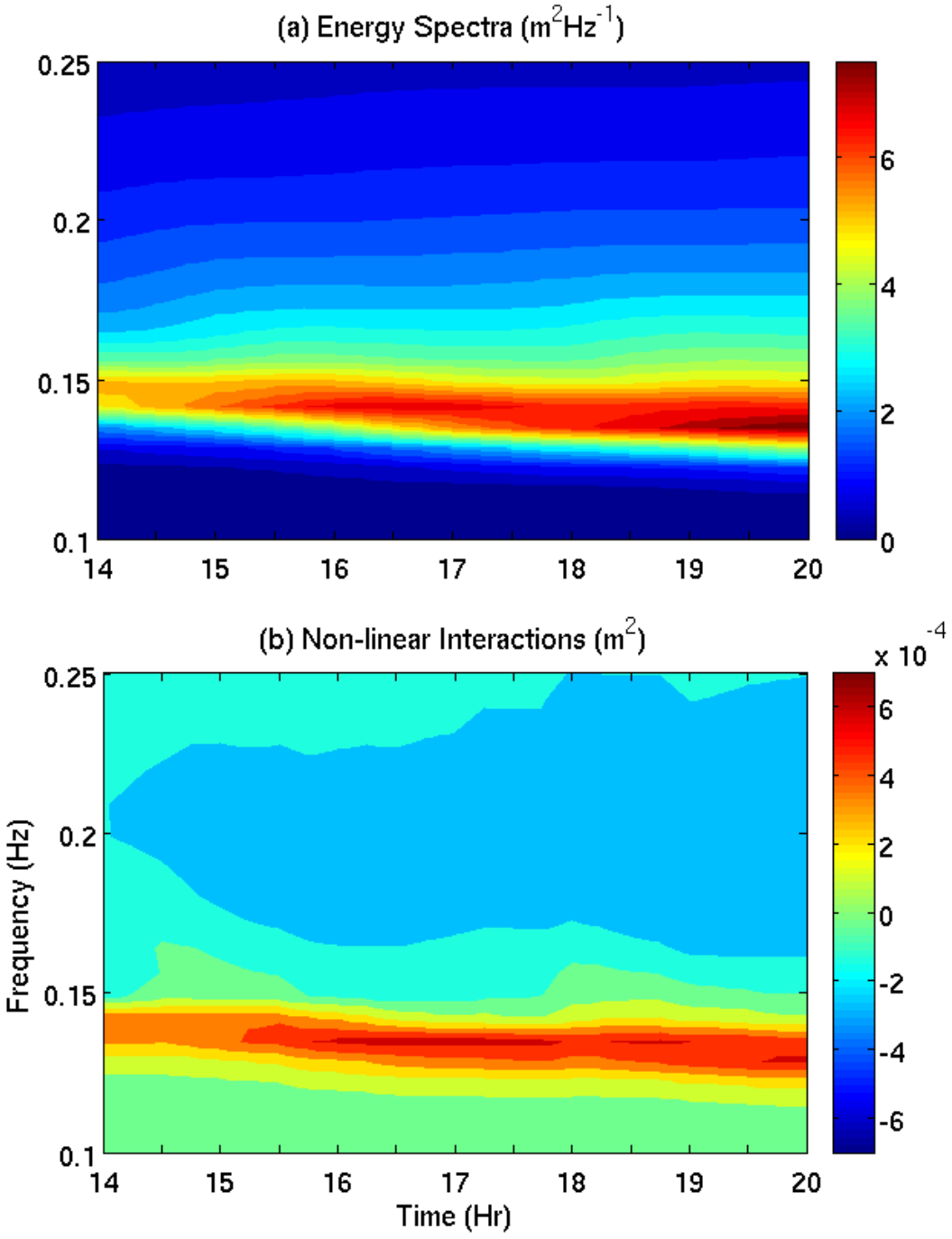

Figure 4.5: A closer view of the oscillations found in (a) the energy spectra and (b) the non-linear interactions for the TSA using the first order propagation scheme.

and the sharp drop in energy with a small amount of concavity in the forward face (the region of spectral space with frequencies lower than the peak frequency) are all shared characteristics of both the WRT and TSA methods. By comparison, the spectrum obtained with the DIA shown in Figure 4.6 has a significantly bimodal distribution of energy in the forward face but no bimodality at higher frequencies, a slower decrease in energy on the forward face and concave sides which are all quite different from the spectra obtained in the WRT or TSA cases. Additionally, while the two-dimensional spectral energy peak of the DIA spectrum is at the same frequency as for the spectra of the other two methods, the spread of energy is larger above the peak, and smaller for the other spectra (from TSA and WRT). The two-dimensional distribution of energy above the peak for the DIA spectrum causes its one-dimensional energy peak to be at higher frequency, explaining the discrepancy between the DIA and WRT curves in Figure 4.2b.

The non-linear interaction spectra for the WRT and TSA methods shown in Figure 4.7 have similar large-scale features except for different peak intensities. Both the WRT and TSA methods generate a broad negative lobe and a narrow, bimodal, positive lobe. By comparison, the interactions obtained using the DIA have a deeper negative lobe and broader positive lobe. The larger spread of the positive lobe and its exaggerated concavity contribute to the presence of similar features in the energy spectrum. The cause of the band of more negative interactions in Figure 4.4c can also be seen in the two-dimensional interactions in Figure 4.7c. It is the frequency interval ($\sim$0.17 Hz) over which the negative lobe is abnormally deep, and where the positive lobes on either sides do not quite compensate.

One hour after the wind turned from easterly to northerly, new wind waves can be seen around $\theta = 180^o$ while the waves generated by the easterly winds ($\theta = 270^0$) are still present, as shown in Figure 4.8. Once again, the spectra obtained using the WRT and the TSA methods are very similar at this time. In this case, however, it is mainly because the non-linear interactions in the wind waves are of much smaller amplitude than the interactions in the swell during the first hour. The TSA method, due to its formulation and due to the parameterization chosen for the broad-scale in this implementation, cannot yet

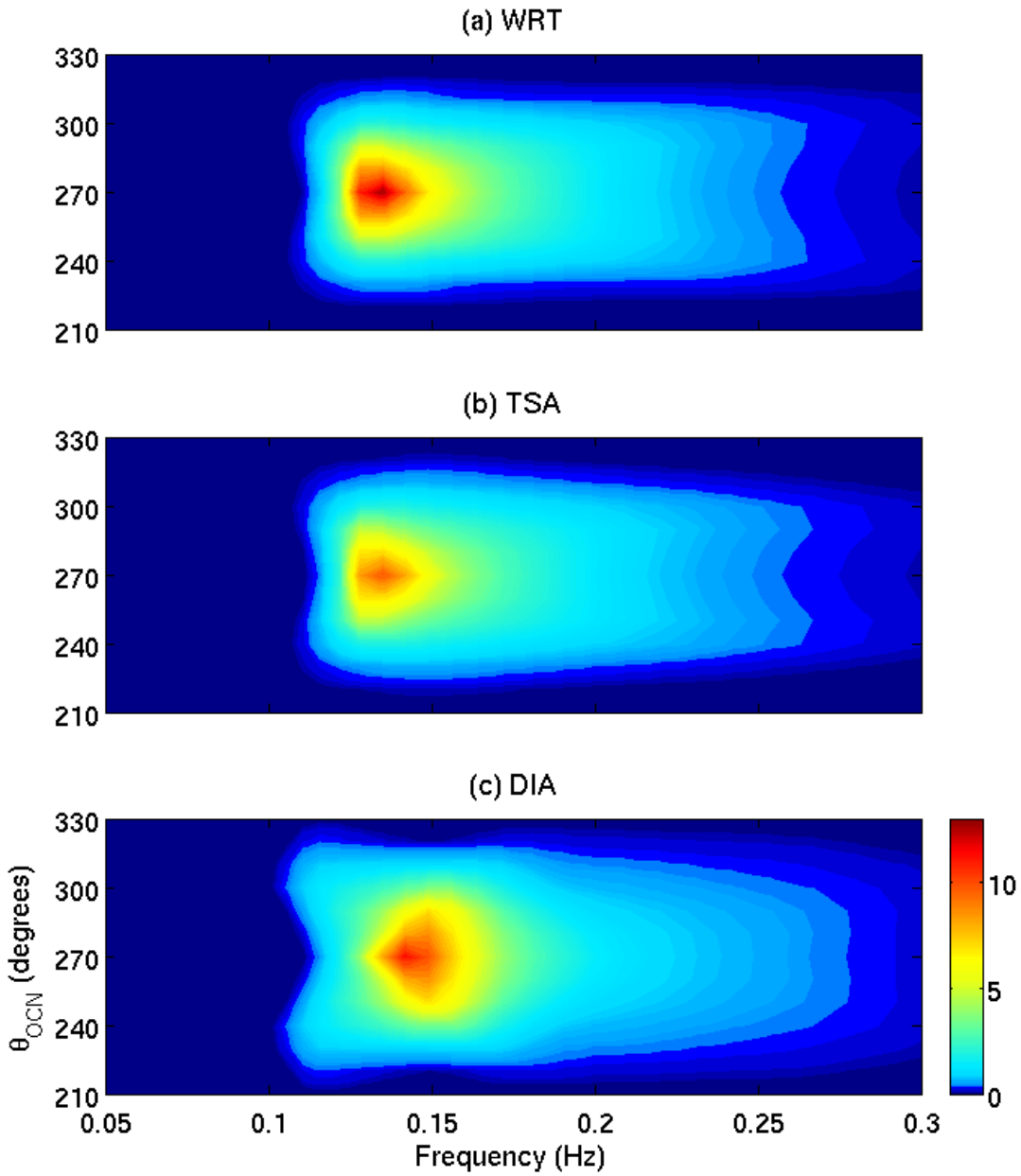

Figure 4.6: Wave energy spectrum ($m^2 Hz^{-1}$) obtained with (a) the WRT method, (b) the TSA and (c) the DIA after 48 hours of easterly winds.

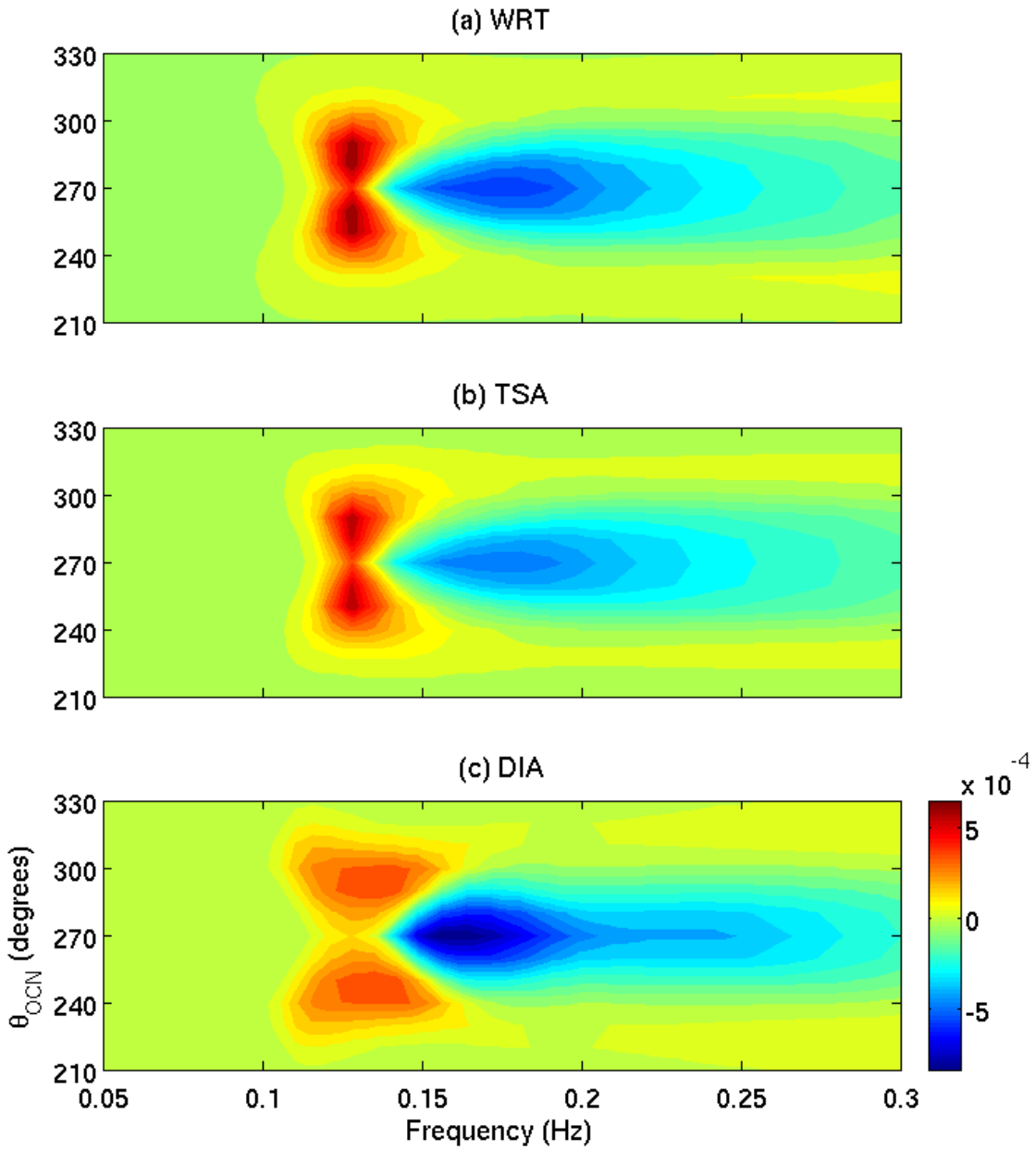

Figure 4.7: Non-linear interactions (m^2) obtained with (a) the WRT method, (b) the TSA and (c) the DIA after 48 hours of easterly winds.

produce reasonable interactions when dealing with multiple peaks in a spectrum. With the TSA method, the broad-scale term will try to fit the highest energy peak, which in this case is the swell peak, resulting in interactions that tend to be accurate only in this region, as shown in Figure 4.9. The other peak is then solely represented by the perturbation term and as such the interactions calculated for it might not be accurate. Figure 4.9 demonstrates that there is very good agreement between WRT and TSA results for the interactions around the swell peak, while around the wind waves, where interactions are dynamically the most important in terms of spectral development, there is very little non-linear transfer. Meanwhile, the DIA's results, while being worse than those of the TSA around the swell peak, globally look more accurate as its formulation is able to give some representation to the non-linear transfer around the wind sea peak of the spectral space. The interactions as calculated with the WRT also include a strong flux of energy towards high frequencies for the wind sea, which is absent from the non-linear interactions of TSA, because it is far away from the region where the broad-scale is dominant. Non-linear interactions from the DIA method also fail in generating intense non-linear interactions at high frequencies (> 0.4 Hz) in the wind direction (Fig.4.9a and c), most likely because of the coarse approximation used.

The model using the TSA still generates relatively accurate results as far as the shape of the energy spectrum is concerned for the transition period, since wind input and dissipation can generate an acceptable wind sea without non-linear interactions in the first few hours following the turn in the winds, while the swell propagates out of the domain. A parameterization which would include the possibility of multiple peaks in the broad-scale would allow the TSA to produce more accurate non-linear interactions for the wind waves during the early phase of the transition.

Three hours after the wind has turned, the majority of the energy associated with waves going westward has propagated out of the domain and the wind waves have reached a level that dominates the overall spectrum. At this time, the magnitude of the interactions calculated with the TSA is very large compared to that of the other two methods, as shown

in Figure 4.10. This is because the spectral shape of the wind waves deviates significantly from its dynamical equilibrium shape, having been misrepresented until now in the TSA methodology. The high amplitude of the interactions allows the model to correct the shape of the wind sea in a relatively short amount of time and from the fourth hour onward, the spectra and non-linear interactions for the WRT and TSA method are once again very close, with the results using the DIA standing out, as was the case during the previous wave growth period. The flux of energy towards high frequencies visible in Figure 4.10 is analogous to the flux observed in the interactions calculated with the WRT method earlier in the simulation and shown in Figure 4.9.

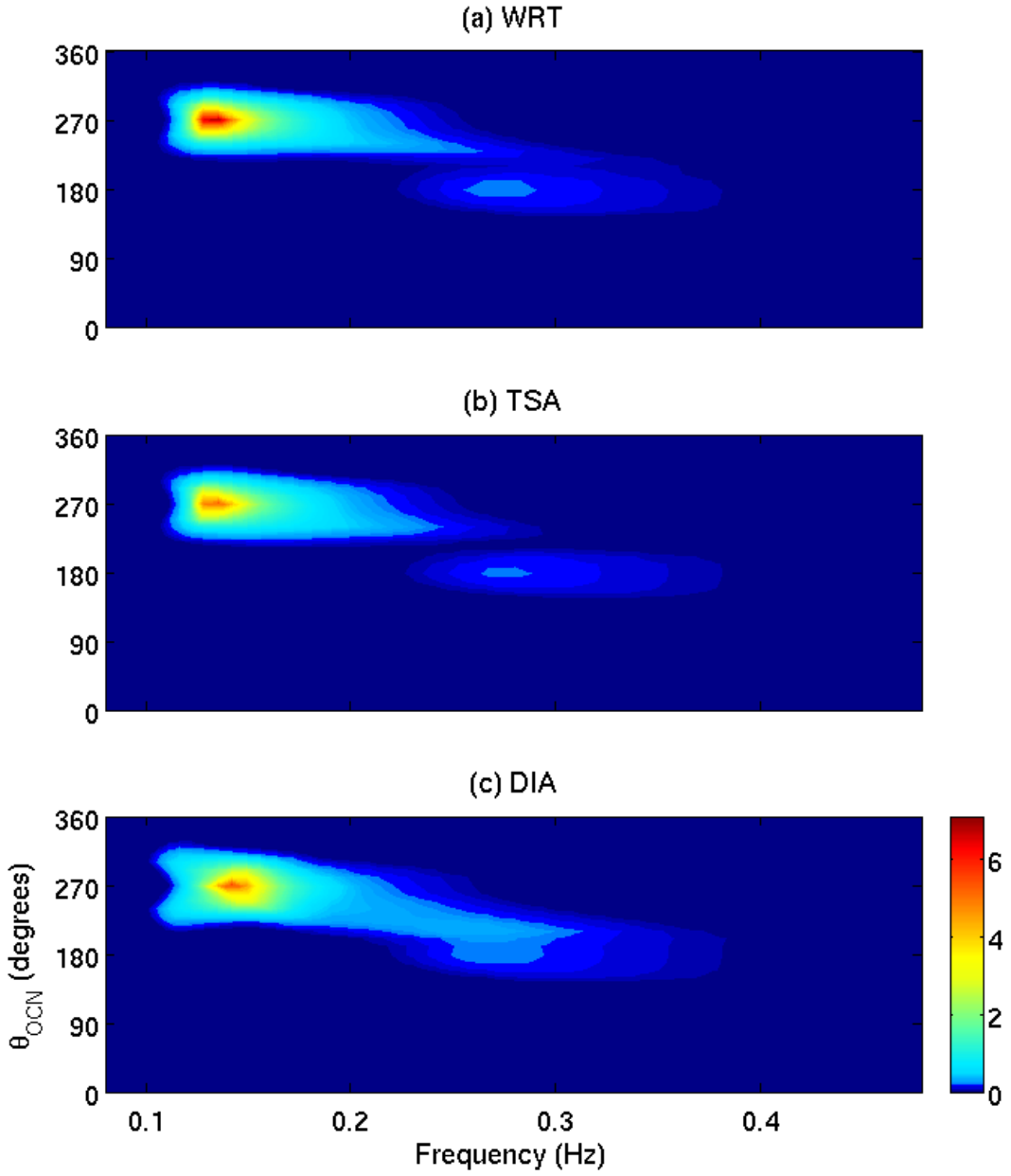

Figure 4.8: Wave energy spectrum ($m^2 Hz^{-1}$) obtained with (a) the WRT method, (b) the TSA and (c) the DIA after 48 hours of easterly winds followed by an hour of northerly winds.

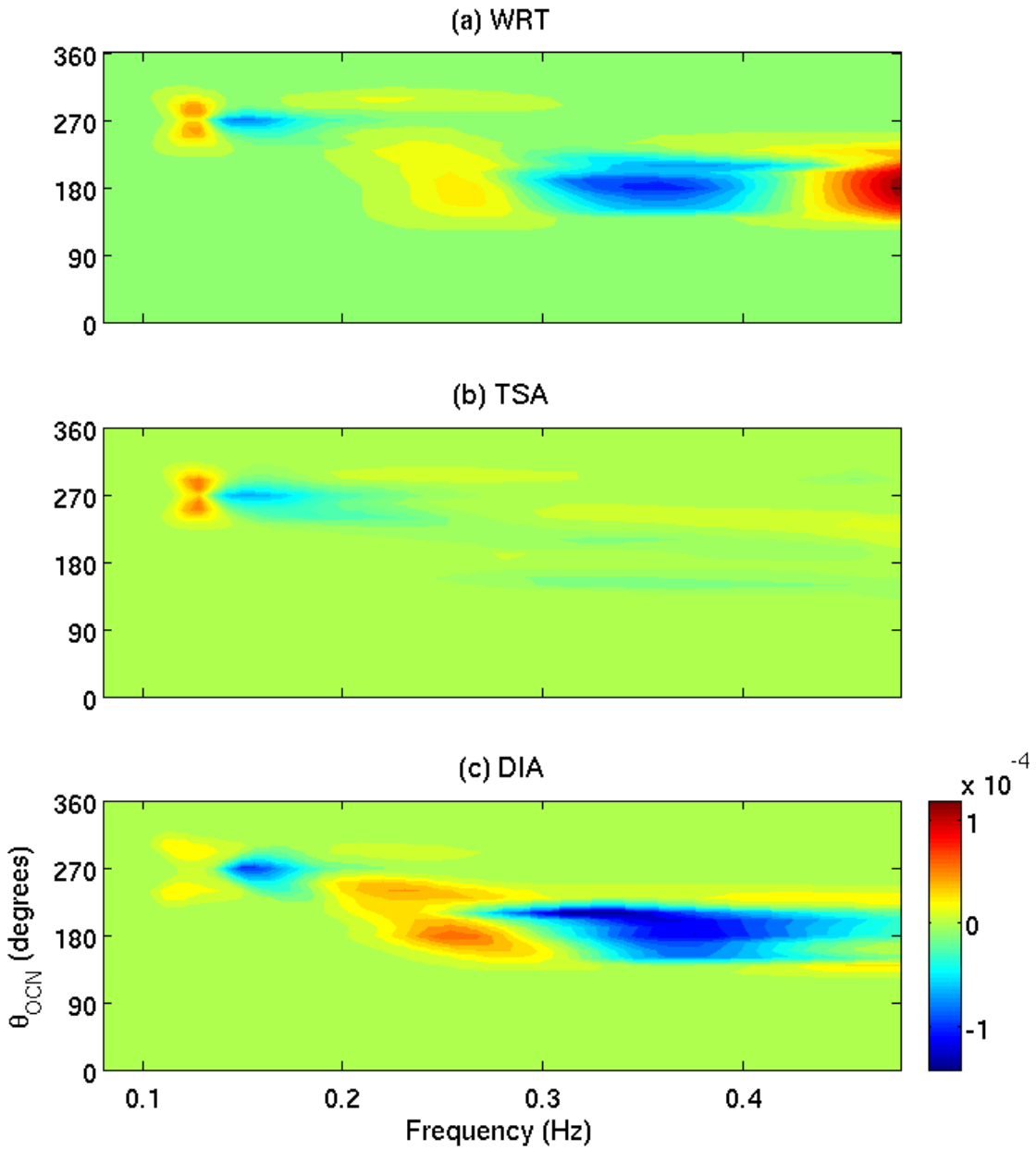

Figure 4.9: Non-linear interactions (m^2) obtained with (a) the WRT method, (b) the TSA and (c) the DIA after 48 hours of easterly winds followed by an hour of northerly winds.

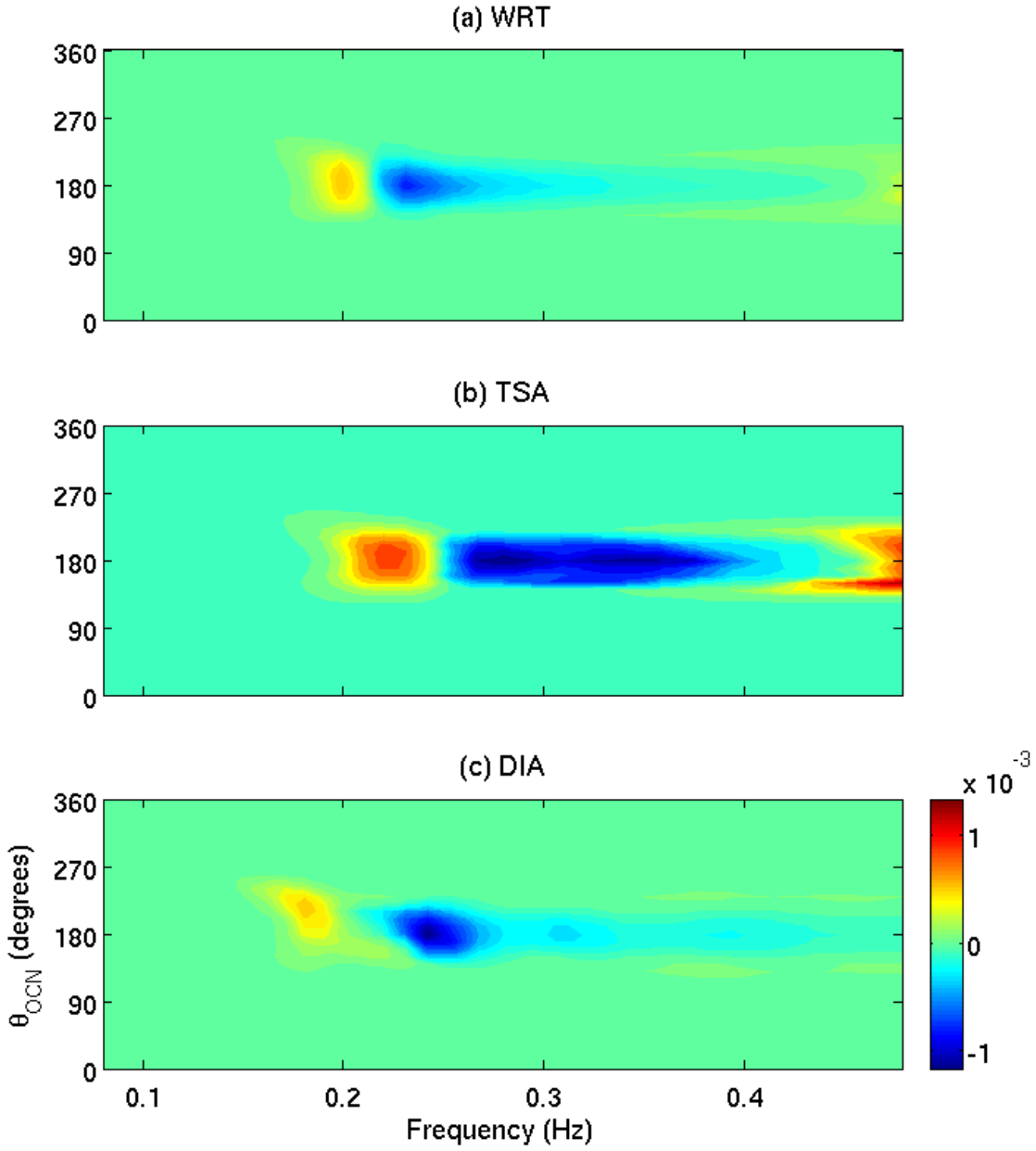

Figure 4.10: Non-linear interactions (m^2) obtained with (a) the WRT method, (b) the TSA and (c) the DIA after 48 hours of easterly winds followed by three hours of northerly winds.

4.2 Slowly Turning Winds

In this section, the performance of the WW3 model using the TSA method is examined in a situation where the change in winds is more gradual. This change in forcing generates an asymmetric wave spectrum instead of multiple distinct peaks. This experiment starts with easterly winds blowing for 48 hours as for the experiment in section 4.1. After 48 hours, instead of suddenly turning the winds by 90^o, winds in this experiment are turned by 7.5^o every two hours, producing a change of 90^o over a period of 24 hours. The meteorological equivalent of this situation would be a cyclone starting directly south of the modelled domain and moving north-eastward, producing a cyclonic rotation in the winds. After the 24 hours turning period, the wave model is ran for an additional 72 hours in order to reach its new equilibrium.

4.2.1 Growth Curves and One-Dimensional Evolution

Unlike the case of the sharply turning winds, with slowly turning winds, differences are large in the growth curves (Figure 4.11) produced by the two propagation schemes once the wind starts to turn. During the first 48 hours, the situation is exactly the same as in section 4.1 (Figure 4.11) and the waves reach the same equilibrium state as in Figure 4.2. After that, the dip in the significant wave height is neither as rapid nor as deep as it is in Figure 4.2 because the change in winds is gradual and the wave energy spectrum of the previous dynamic equilibrium is gradually modified, instead of being fully decoupled from the wind and instantly becoming swell which propagates out while new wind waves are created. Similarly, since there is no entirely new wind sea created, the spike in peak frequency observed in section 4.1 (when the location of the maximum energy changed from swell to wind sea) does not occur in this case. Instead, a gradual transition starts at hour 48 and lasts for more than 24 hours.

The results obtained using the TSA and WRT methods in this experiment are similar during wave growth. By comparison, the DIA and the WRT methods produce similar model results during the transition period: with one smooth dip in significant wave height, or peak in peak frequency, followed by a new equilibrium state. This is not the case for the

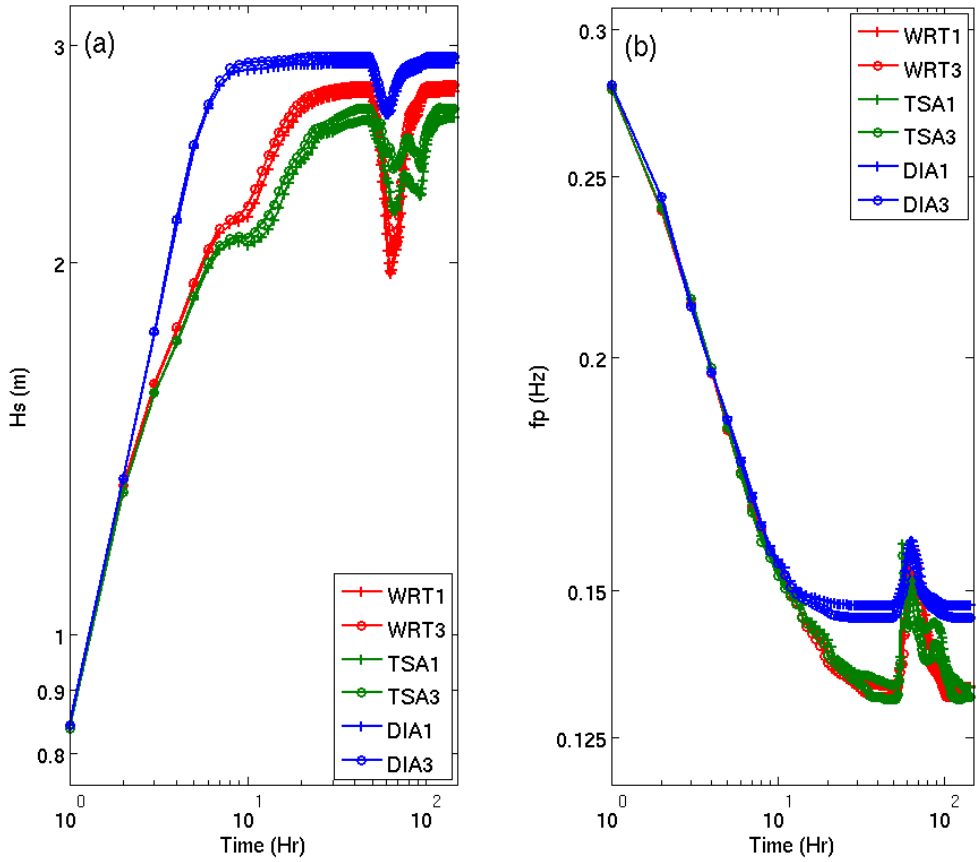

Figure 4.11: Growth curves for the slowly turning wind experiment showing (a) the significant wave height and (b) the peak frequency. Different formulations for non-linear interactions are marked by different colours, while the different propagation schemes (first or third order) are marked by different symbols.

results obtained using the TSA, which has two oscillations of differing amplitudes instead of one.

The evolutions of the one-dimensional energy spectra shown in Figure 4.12 are consistent with the growth curves of their respective mean wave parameters. The WRT and DIA results are smooth and show a gap between maxima while the wind was turning. The one-dimensional TSA results are very similar between the two propagation schemes, although their growth curves are different from one another. This is because the different timing of the oscillations is much more obvious with time shown on a logarithmic scale as in Figure 4.11, then when shown linearly as in Figure 4.12. The time required to reach

equilibrium is longer because of these oscillations, which are similar to the ones occurring in the experiment in section 4.1. The equilibrium solutions of the results obtained with the three methods are essentially the same as in the experiment in section 4.1, as should be expected given that the forcing is the same, except for the more gradual transition phase.

The slowly turning winds modify the energy spectrum over time which is different from the creation of new wind waves as in section 4.1. The TSA was initially expected to perform better with the slowly changing wave spectrum than with a spectrum showing multiple peaks. However, the difficulties in dealing with asymmetries created in the wave spectra from the spin-up period by the turning winds proved to be a significant challenge for the TSA in this experiment.

Figure 4.13 shows differences between one-dimensional non-linear interaction spectra generated by the two propagation schemes for the three methods. Results obtained with the WRT method are the least sensitive to the change of propagation schemes. For both the TSA and DIA methods, the negative lobes in model runs with the third order scheme are wider than when the first order scheme is used. The oscillations present after the winds turned are also more important when using the third order scheme. This can be seen in the most negative part of the interactions for TSA, between hours 67 and 77 and for both the positive and negative parts of the DIA results.

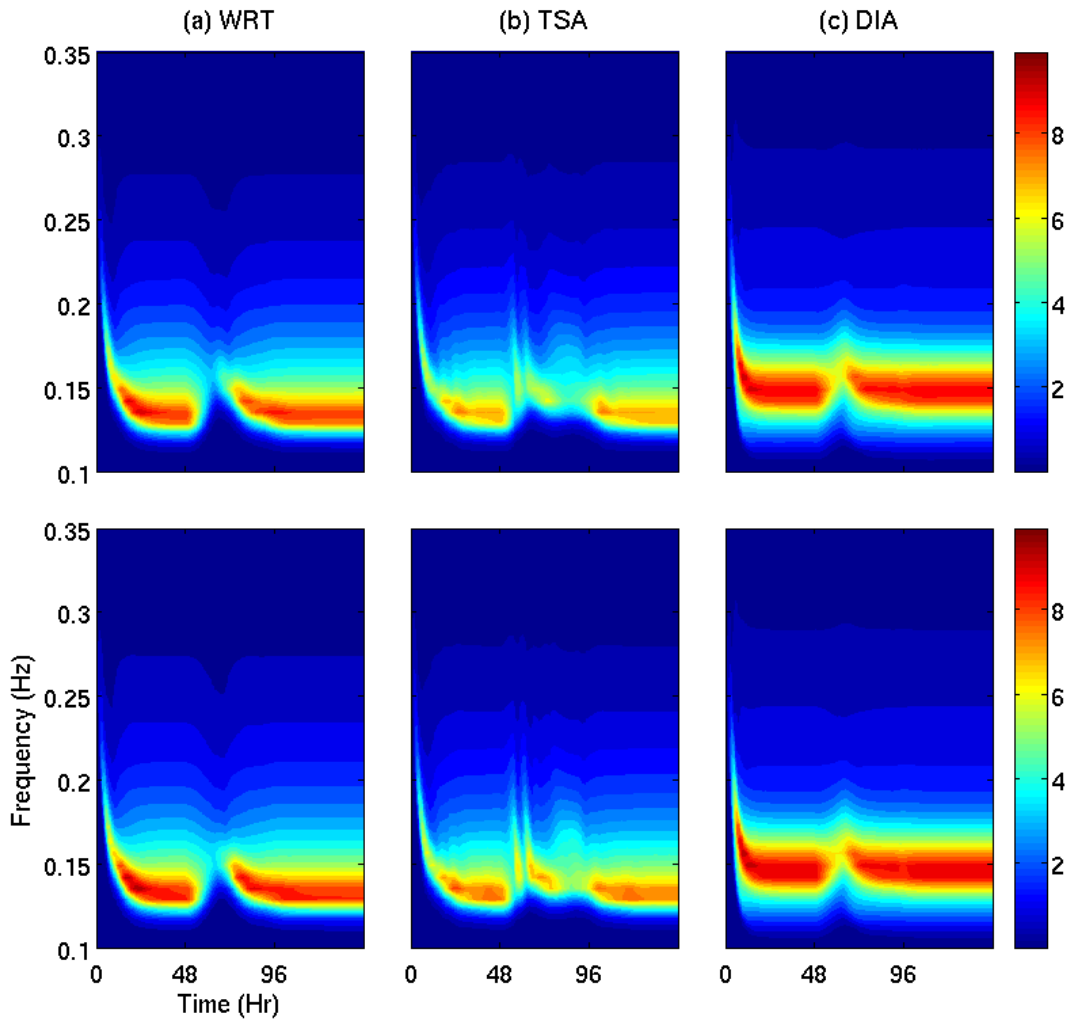

Figure 4.12: One-dimensional energy spectrum evolution in m^2Hz^{-1} for (a) the WRT, (b) the TSA and (c) the DIA obtained using the first order propagation scheme (top) and third order scheme (bottom).

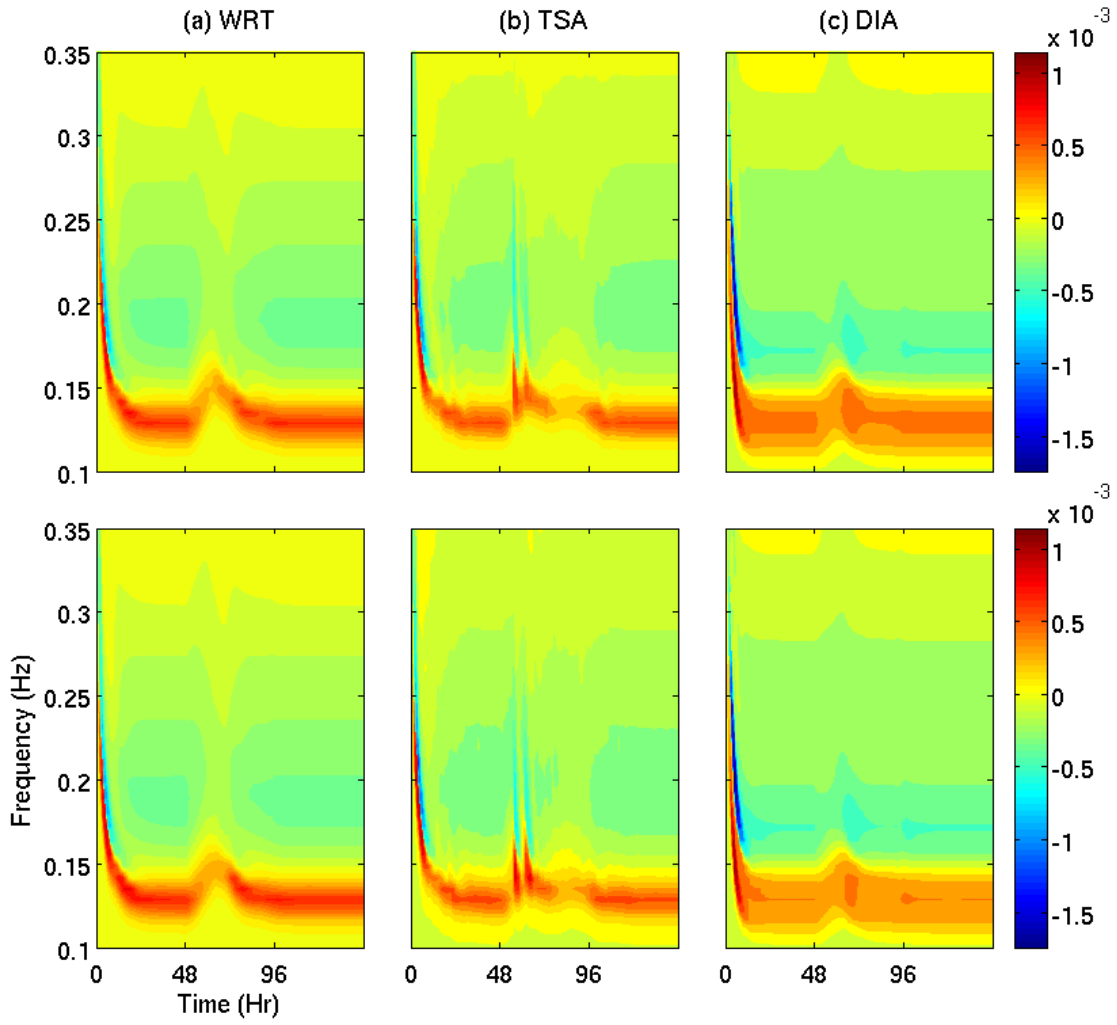

Figure 4.13: One-dimensional non-linear interactions in m^2 for (a) the WRT, (b) the TSA and (c) the DIA obtained using the first order propagation scheme (top) and third order scheme (bottom).

4.2.2 Two-Dimensional Spectral Evolution

The most interesting wave development occurs in the twenty-four hours during which the wind is turning. The oscillations seen in Figures 4.12 and 4.13 during this period are due to the current formulation used for TSA's parametric fit to generate the broad-scale component of the energy spectrum. Depending on the frequency and direction of the energy peak, the TSA model will generate a broad-scale term using a predefined shape. As shown in section 4.1.2 when the broad-scale component changed from swell to wind sea, the location of the broad-scale peak in spectral space has a significant impact on the quality of the interactions obtained with the TSA method.

The oscillations observed while the wind is turning in this experiment are in essence the same phenomenon as the sudden strong non-linear interactions at the fifty-first hour of the experiment described in section 4.1.2. In this case, instead of being caused by the propagation of the swell outside the domain during the growth of the new wind-sea, the shift in the spectral location of the broad-scale is caused by the changes in the shape of the energy spectrum.

With slowly turning winds, the broad-scale component does not change appreciably at every time step, because the general shape of the spectrum evolves slowly. However, the perturbation grows because the wind input is stronger on one side of the energy spectrum than on the other. When the asymmetry is large enough to affect the parametric fit of the spectrum, a significantly different broad-scale component is generated. Since the TSA depends strongly on the broad-scale, the shift causes a change in the shape and location of the non-linear interactions which will in turn impact the evolution of the energy spectrum differently. Over successive iterations of the model, the spectrum converges towards a new solution. Meanwhile, the perturbation grows on one side because of the turning winds, until the whole process begins anew with another shift in the broad-scale. Only when the forcing becomes stationary can the oscillations recede. Indeed, in Figures 4.12 and 4.13, the last oscillation occurs after the winds settled in their new direction and has smaller amplitude than the other ones.

Figure 4.14 shows the wave energy spectra and non-linear interactions seven hours after the winds have started to turn. The energy spectrum from the TSA has taken a shape which is significantly different from the spectrum obtained with the WRT method, with corresponding non-linear interactions. At this point, the spectrum obtained using the DIA is closer to that of the WRT and the DIA non-linear interactions are closer to those of WRT than TSA. The shape of the positive peak of the interactions of all three methods is also closely tied to the shape of the corresponding energy spectrum. The fitting routine currently used for the TSA cannot properly represent strongly asymmetric energy spectra. Since the perturbation is too large, the interactions calculated using the TSA have diverged from those of the WRT method, leading to a different wave energy spectrum.

One hour later, after the wind has been turning for eight hours, the wind waves, the spectral components centered on $\theta = 240^o$, now contain most of the energy present in the spectrum, as shown in Figure 4.15. At this point, the broad-scale shifts from being a fit of the swell centered on $\theta = 270^o$ to fitting the wind waves. The interactions calculated with the TSA are stronger than those of the other methods. The shape of the spectrum is significantly different from its equilibrium shape which explains the magnitude of the interactions, even though the overall energy content of the spectrum the TSA model run is smaller. The non-linear interactions calculated by the TSA at this step have a strong positive peak at $\theta = 270^o$, the location of the energy peak in the WRT model run, rather than the wind sea peak, around $\theta = 240^o$ like in the previous hour. On the other hand, nothing has changed for the DIA, both the energy and the interactions are close to the ones shown in Figure 4.14.

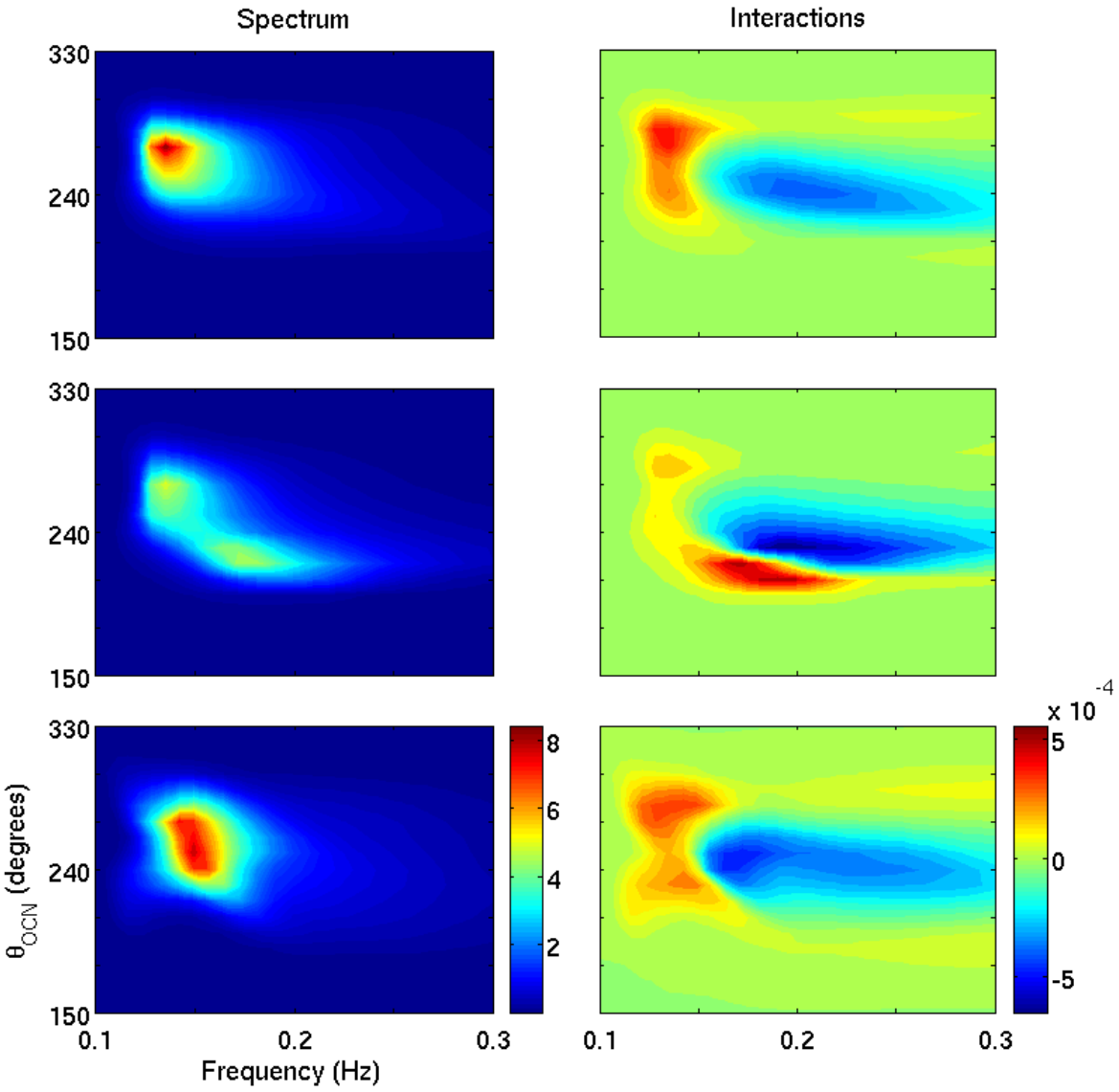

Figure 4.14: Wave energy spectrum ($m^2 Hz^{-1}$) (left) and non-linear interactions (m^2) (right) obtained with the WRT method (top), the TSA (centre) and the DIA (bottom) after 48 hours of easterly winds followed by seven hours of turning winds.

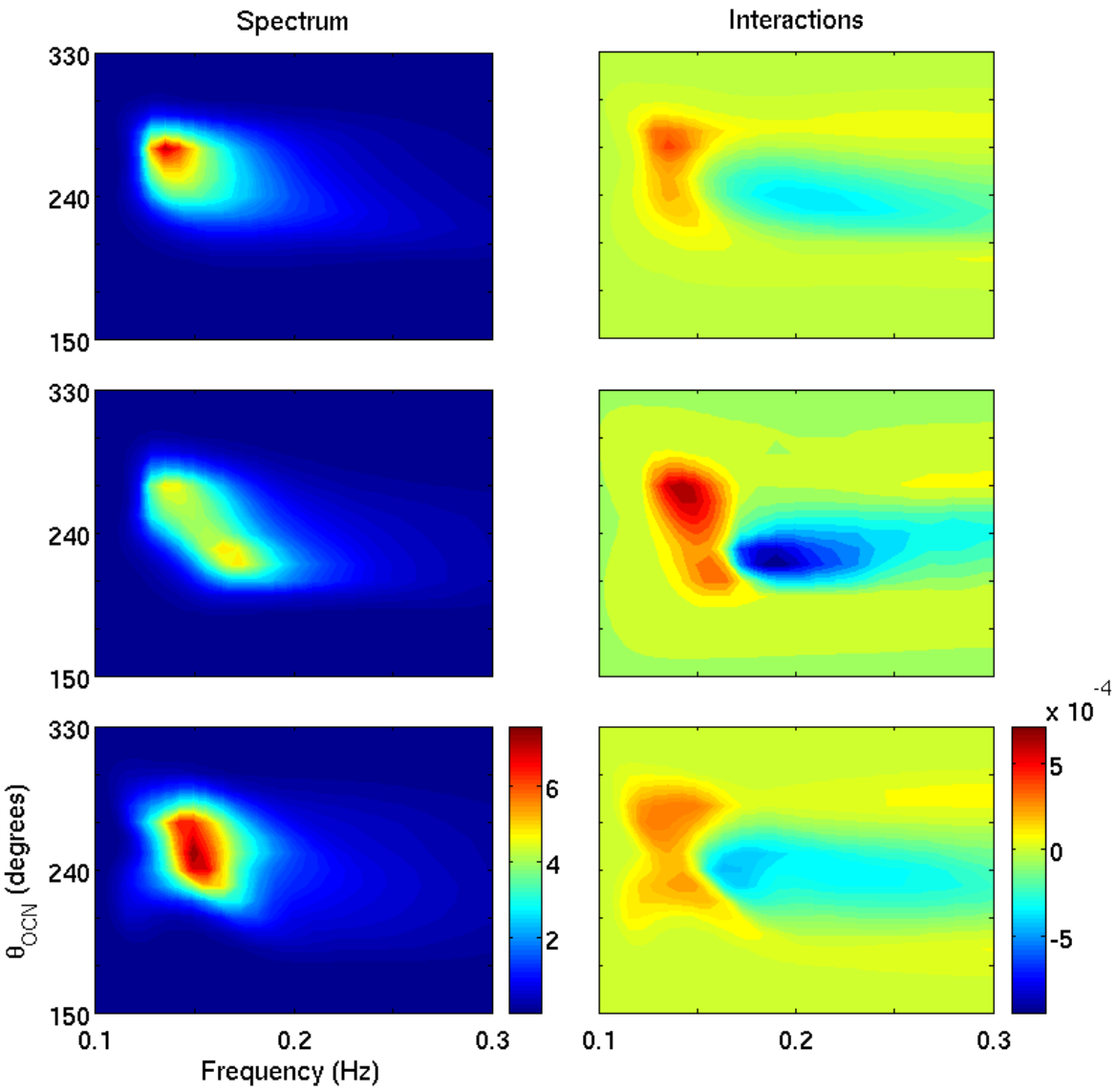

Figure 4.15: Wave energy spectrum (m^2Hz^{-1}) (left) and non-linear interactions (m^2) (right) obtained with the WRT method (top), the TSA (centre) and the DIA (bottom) after 48 hours of easterly winds followed by eight hours of turning winds.

During the next three hours, non-linear interactions contribute to the convergence of the energy spectrum obtained using TSA towards the spectrum obtained with the WRT method. After these three hours, there is much more in common between the WRT and the TSA results than with the DIA, as seen in Figure 4.16.

On the twelfth hour, however, the wind sea portion of the energy in the TSA result, shown in Figure 4.17, is once more becoming stronger due to the lack of representation of the developing spectral components in the broad-scale. This flaw in the parametric fit causes the interactions to be more positive in that region than they should be. This begins a new cycle where the energy spectrum deviates from the solution obtained with the WRT method until a change in the location and shape of the broad-scale brings the evolution back to convergence to the WRT result.

These oscillations continue as the wind keeps turning, until the forcing stops turning and the interactions calculated using the TSA make the energy converge to its dynamical equilibrium solution. This test shows that, under recurring changes in the forcing, the current version of the TSA responds in incremental bursts instead of continuously, indicating that the TSA requires a parametric shape which allows for asymmetry in the energy spectrum so that the broad-scale component can evolve more gradually.

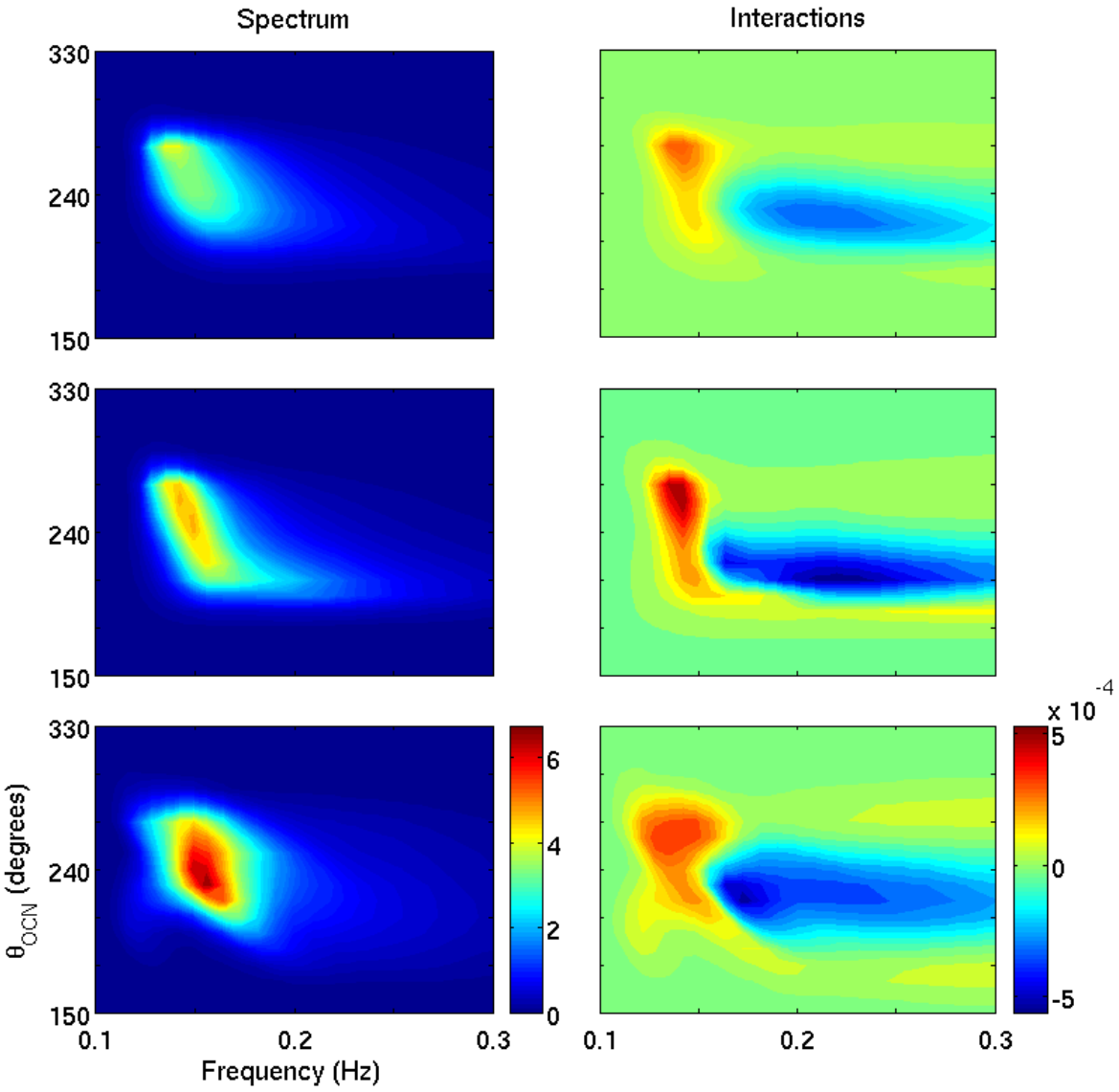

Figure 4.16: Wave energy spectrum ($m^2 Hz^{-1}$) (left) and non-linear interactions (m^2) (right) obtained with the WRT method (top), the TSA (centre) and the DIA (bottom) after 48 hours of easterly winds followed by eleven hours of turning winds.

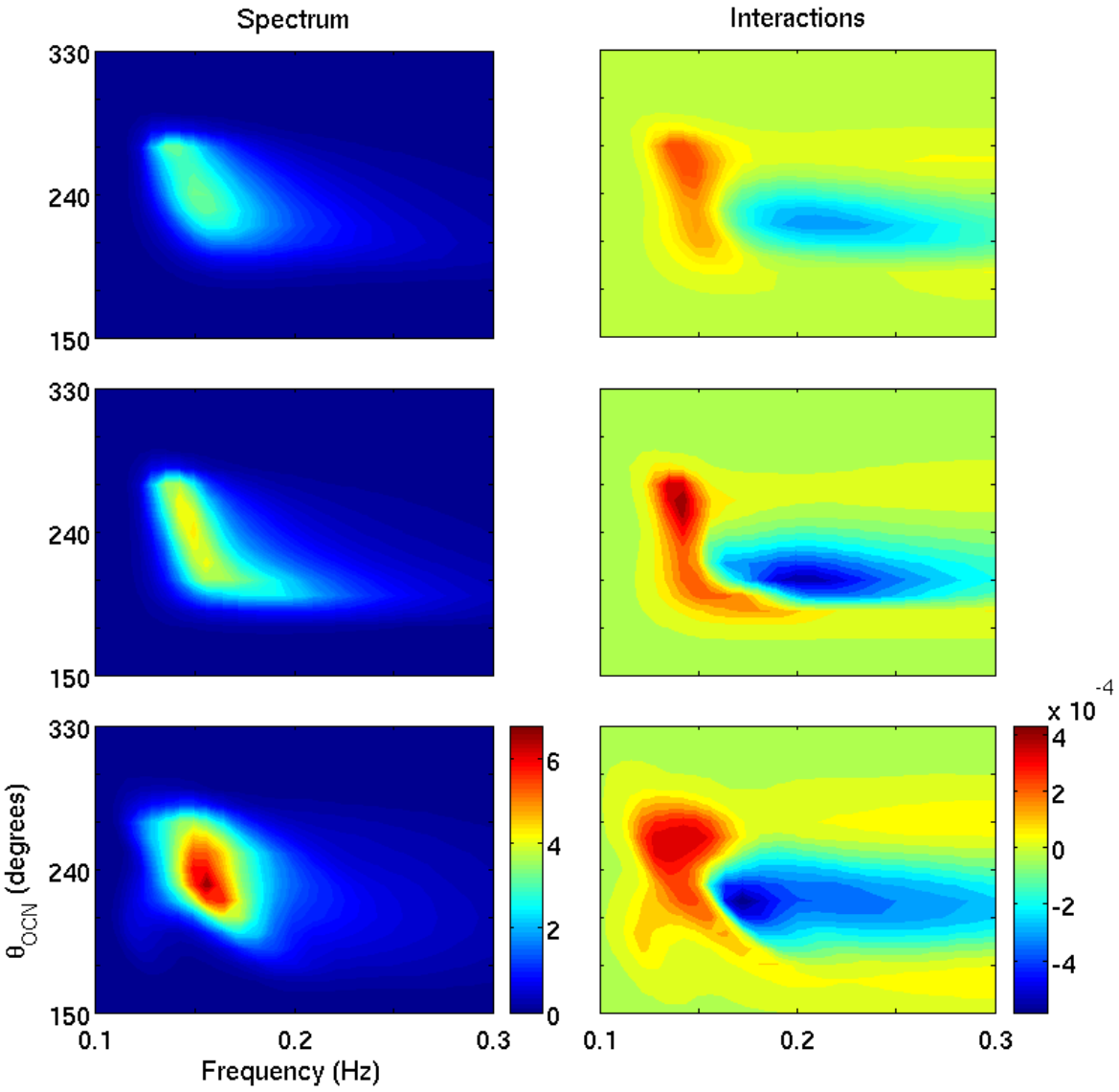

Figure 4.17: Wave energy spectrum ($m^2 Hz^{-1}$) (left) and non-linear interactions (m^2) (right) obtained with the WRT method (top), the TSA (centre) and the DIA (bottom) after 48 hours of easterly winds followed by twelve hours of turning winds.

CHAPTER 5

TWO-DIMENSIONAL EXPERIMENTS

Five additional experiments were performed on a two-dimensional domain, which are primarily intended to compute the basic fetch-limited growth curves and, secondarily, to investigate the impact of wave propagation and swell - wind sea interactions in model runs using the version of the TSA method proposed in this thesis. The model domain is a square ocean of 23 by 23 points with a grid spacing of 50km. The outer points of the domain are land, so waves reaching the boundary of the domain are simply absorbed. Of the 441 active points, 25 were chosen as the models output points in the four experiments, providing additional data about the dynamics of the wave evolution at their locations. These points are located on a 5 by 5 square grid, as shown in Figure 5.1, and were chosen to obtain maximum coverage.

5.1 Wave Generation

In this experiment the two-dimensional domain is subjected to 20 m/s winds coming from the east for 48 hours. With the waves growing on a wide domain, both duration-limited and fetch-limited growth comparisons can be performed using the DIA, WRT and TSA formulations for the non-linear interactions. This experiment also serves as the initial conditions for the subsequent forays into more complicated sea-states.

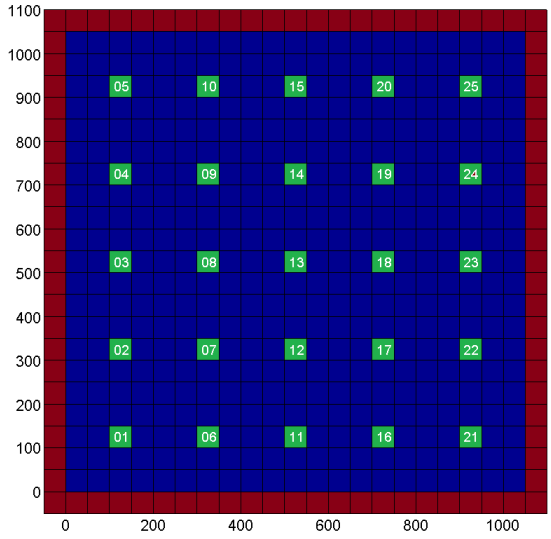

Figure 5.1: Model domain used for the two-dimensional experiments. Green points are output points shown with their associated numbers, red points are land and blue points active ocean points.

5.1.1 Field Evolution

The wave field develops under constant easterly winds. In this setup wave heights at a given time are highest in the model run using the DIA and lowest using the TSA. The highest waves over the model domain for all methods and propagation schemes combinations are at the centre of the domain's west side. The fields of significant wave height, H_s, at hour 24 are shown in Figure 5.2. The maximum values are 8.74 m for the model using the WRT, 7.72 m for the TSA and 9.03 m for the DIA methods.

The general progression of small waves on the east of the domain and larger waves on the west side is very similar among the three models, especially in the easternmost quarter of the domain. The fetch-limited growth seen here is somewhat equivalent to duration-limited growth sampled at different times. The similarity between all the H_s fields for the easternmost quarter of the model domain, followed by more visible differences in wave heights at larger fetches in the domain, are consistent with the growth curves shown in section 4 for single point integrations. The three methods using both propagation schemes

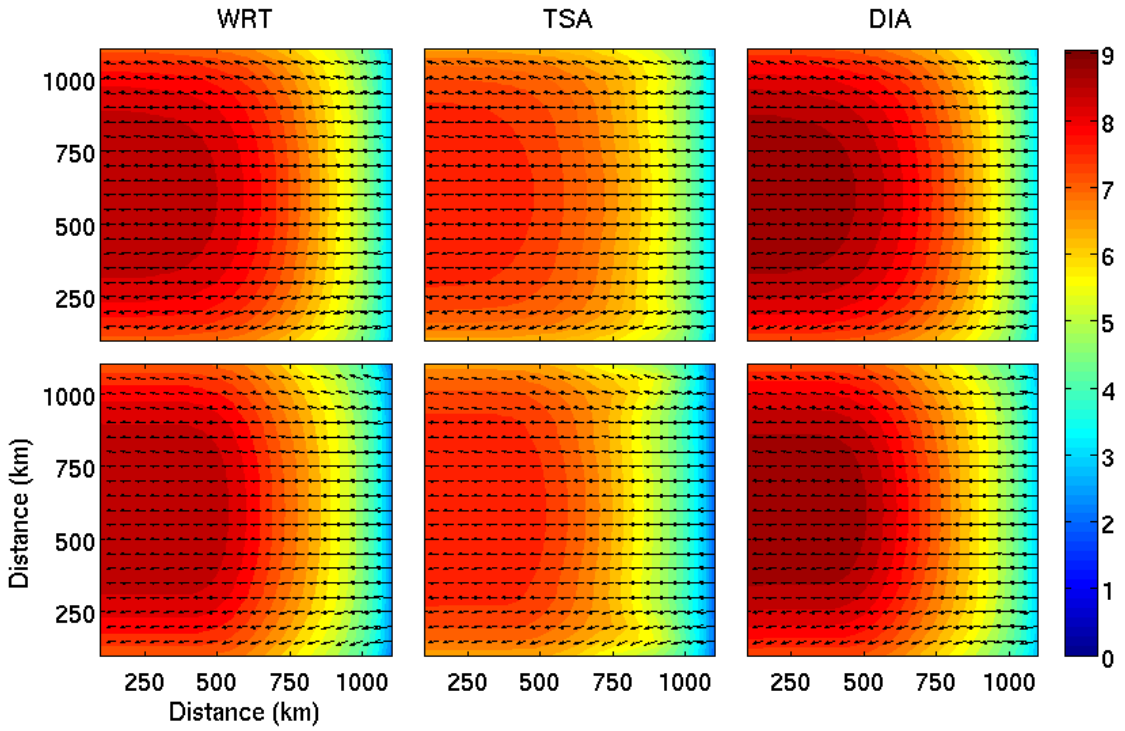

Figure 5.2: Significant wave height fields (in meters) and wave direction (arrows) after 24 hours of easterly winds for the WRT (left), the TSA (centre) and the DIA (right) with the first and third order propagation schemes (top and bottom, respectively).

have similar skill in simulating H_s for the short fetch. However, differences become obvious among interaction schemes at longer fetch, or after longer times, as different interaction schemes converge to different dynamic equilibria.

There are some differences in the spatial distributions of wave height among the six cases presented in Figure 5.2. While the wave fields generated using the first order propagation scheme (in the top row) have curved contours on the northern and southern sides of the domain, the third order scheme produces slightly straighter contours, parallel to the coastlines of the domain. This is due to the larger numerical diffusion in the first order propagation scheme than in the third order scheme and occurs regardless of the method used for the computation of non-linear interactions.

Another impact of the propagation schemes, which is more visible in the wave fields at hour 48 shown in Figure 5.3, is the smoothing of the numerical noise in the TSA's field.

At that point, unlike the fields obtained using the WRT and DIA methodologies, the TSA shows strong interactions with the edges of the domain. These create two protrusions of higher significant wave heights near the edges. Using the first order scheme, the protrusions are smoothed somewhat by the numerical diffusion. However, with the third order propagation scheme, they are much more clearly defined. The early development of these structures can be seen in Figure 5.2 as well, close to both the north and the south edges of the domain, between the fifteenth and seventeenth points. These structures are absent in the early stage of wave growth. They first occur on the eighteenth hour of the evolution close to the eastward edge of the domain. By then, the wave height where these features are seen has reached its maximum fetch-limited value and the wave spectrum is in dynamic equilibrium. The waves then propagate westward across the domain and continue to reach their wave height limits as dictated by fetch, as can be seen by comparing Figures 5.2 and 5.3.

5.1.2 Growth Curves

The evaluation of the evolution of the main wave parameters, significant wave height (H_s) and peak frequency (f_p), is very important in assessing the characteristics of wave models. Only duration-limited growth curves could be assessed with the one point experiments presented in chapter 4. The duration-limited growth curves at point #3, located at the centre near the western edge of the domain, are presented in Figure 5.4. In the initial phase of the wave growth, waves appear to be dominated by local generation processes. During this phase, which covers the first ten hours, wave heights simulated using the TSA are particularly close to results obtained with the WRT method. As time goes on, waves propagate from greater distances, nearer the eastern edge of the domain, leading to the creation of waves about ten meters high after thirty hours. After the first ten hours, wave heights obtained using the TSA method are lower than those obtained using the WRT method and their equilibrium solution also differs. As the TSA results diverge from WRT results, the DIA converges to about the same wave heights as the WRT method. This is expected as source terms S_{in} and S_{ds} have been tuned to be largely in agreement with

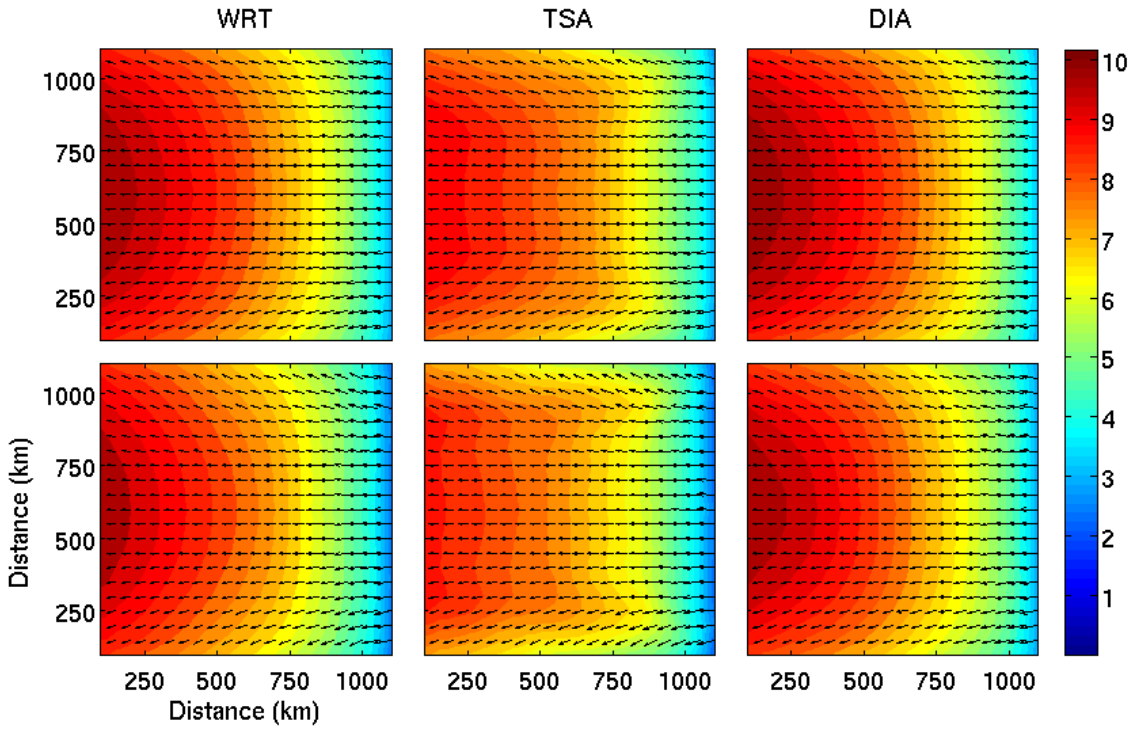

Figure 5.3: Significant wave height fields (in meters) and wave direction (arrows) after 48 hours of easterly winds for WRT (left), the TSA (centre) and the DIA (right) with the first and third order propagation schemes (top and bottom, respectively).

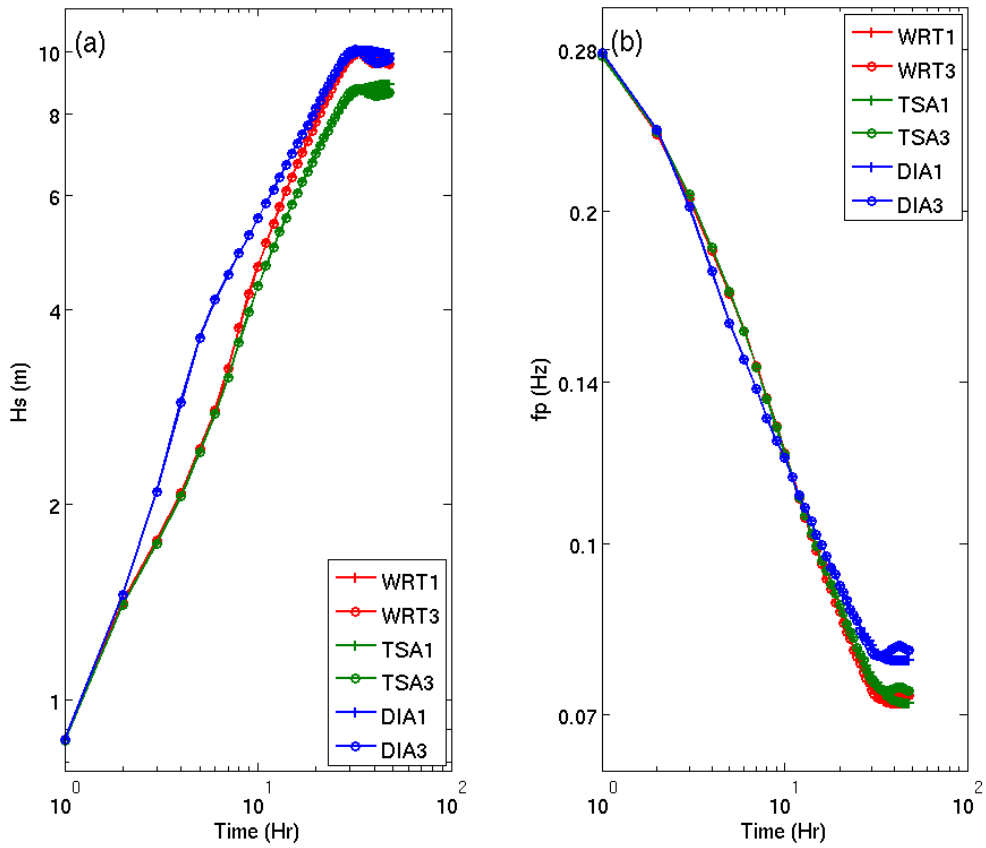

Figure 5.4: Duration-limited growth curves for output point 3 of the two-dimensional domain showing (a) the significant wave height and (b) the peak frequency. Different methods for non-linear interactions are marked by different colours, while the different propagation schemes are marked by different symbols.

observed fetch-limited growth curves for the WRT and DIA methods, for example as discussed by *Holthuijsen* (2007), while this has not been done for the TSA.

Unlike in the significant wave height growth curves, in the peak frequency growth curves, shown in Figure 5.4b, the WRT and TSA curves remain very close for the full 48 hours, while the DIA stabilizes at slightly higher frequencies. These results are similar to those obtained for duration-limited growth results in the one-point experiments described in chapter 4, which shows that the addition of wave propagation preserves the similarity between growth curves. Only when the waves converge to their final highest significant wave height does the propagation scheme make much difference, with the 1st

order linear scheme somewhat limiting the oscillations about the dynamic equilibrium limit.

Figure 5.5 presents results produced by the three methods at points #23, #18, #13, #8 and #3, which form a transect going through the center of the domain parallel to the wind direction. These points are chosen in order to minimize the impact of the north and south boundaries of the domain on fetch limited growth observed along the transect. Along this transect, fetch is the distance from the eastern boundary point. Fetch-limited growth curves along this transect after 48 hours are shown in Figure 5.5. Fetch- and duration-limited growth should have some degree of equivalence, through similarity properties of the wave equations, whereby waves which have developed at longer fetches are older. In this case, the fetch-limited growth curves are consistent with the duration-limited ones. At short fetch, the significant wave height obtained with TSA and WRT are close together, but the TSA results diverge from the results obtained with the WRT method at longer fetch due to contributions of the other source terms (S_{in} and S_{ds}), and the advection. Results calculated by the DIA show much higher wave heights at short fetch than results calculated by the TSA and WRT methods. At long fetches the levels obtained using the DIA converge towards those obtained using the WRT method. The TSA and WRT results remain close together in terms of peak frequency, especially when using the first-order propagation scheme, while the results from DIA are consistently higher.

5.1.3 Spectral Evolution

The main advantage of the TSA over the DIA is its ability to calculate more accurate non-linear interactions which have a similar spectral shape as that obtained with WRT's representation of the non-linear wave-wave interactions. Thus, spectral evolution as produced by the TSA should resemble that resulting from WRT. The spectra obtained from location #3 for both the TSA and WRT methods support this. After twenty-four hours, spectra obtained using both propagation schemes look very similar; therefore only the spectra obtained with the first-order scheme are presented in Figure 5.6. This similarity in spectra for all methods explains why the growth curves shown in Figure 5.4 do not appear to appreciably differ between the two propagation schemes.

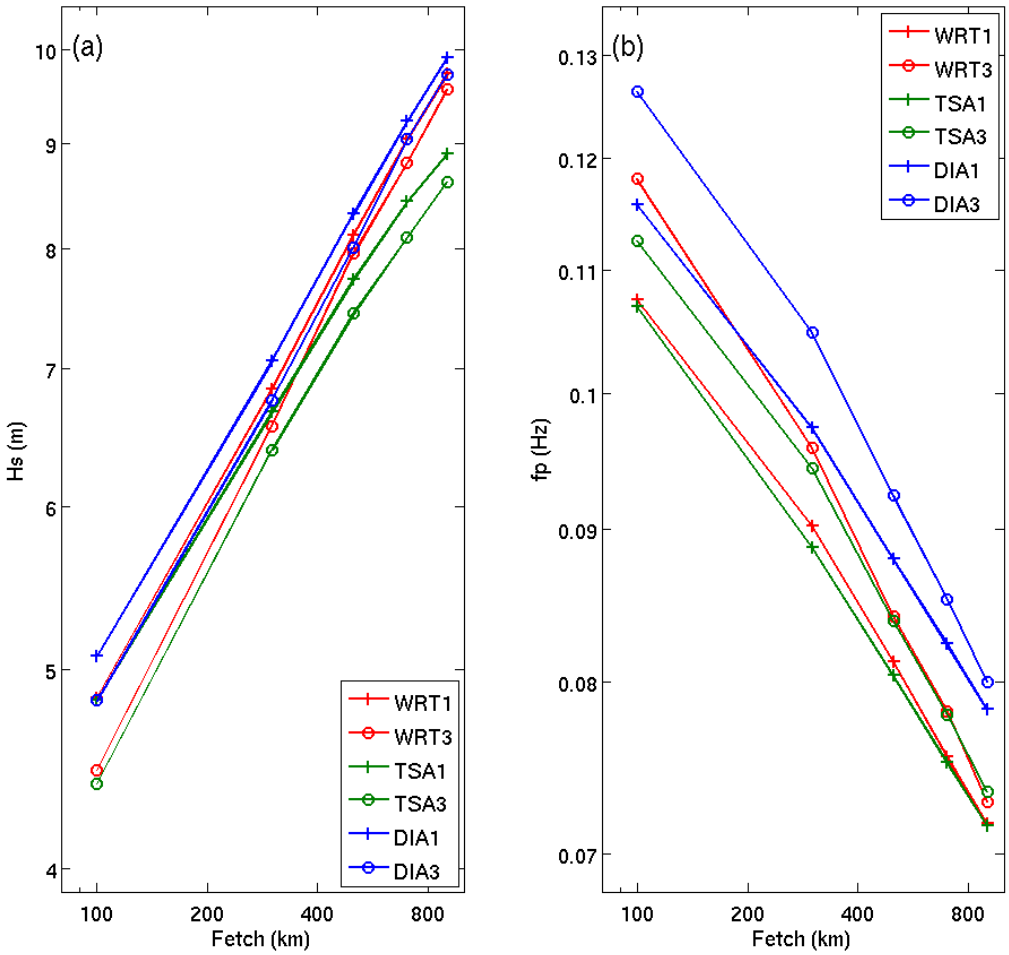

Figure 5.5: Fetch-limited growth curves for a transect in the middle of the two-dimensional domain after forty-eight hours showing (a) significant wave height and (b) the peak frequency. Different formulations for non-linear interactions are marked by different colours, and the different propagation schemes are marked by different symbols.

There are however significant differences in both the wave energy and non-linear interaction spectra among all three methods (Fig.5.6). Wave energy spectra obtained using the TSA and WRT methods peak at the same frequencies and have a similar steep forward face. They are also both bimodal at higher frequencies. Their main difference is in the values of the peak energy, which is lower in the TSA results than for the WRT. This explains the lower significant wave heights and similar peak frequencies. Energy spectra obtained using the DIA are somewhat different from the spectra using the WRT, with a peak energy occuring at higher frequency than for the energy spectrum from the WRT method and a different directional distribution. The forward face of the energy spectrum of the DIA results is not as steep as that obtained with the other methods and also spread over a wider range of directions. Contrary to the one point experiment, the high frequency part of the spectrum obtained using the DIA method does show a certain degree of bimodality.

The non-linear interactions calculated by the three methods are dependent on the respective input energy spectra. The interactions calculated using the WRT and TSA methods have narrow positive and negative lobes, with very shallow extensions towards higher frequencies. The non-linear interactions calculated using the WRT method show two high frequency side lobes which are not reproduced with the same intensity by TSA or DIA formulations. The WRT method generates a separated extension of the negative lobe towards higher frequencies, which the DIA somewhat reproduces, albeit with two regions of negative interactions. The extension of the energy spectrum derived from the DIA towards lower frequencies is explained by the two maxima and wider spread in frequencies of the positive lobe of the interactions calculated with it.

Figures 5.7 and 5.8 show the equilibrium spectra obtained using the first and third order propagation schemes at hour 48. The wave fields have reached their dynamic equilibria, as seen in the growth curves, and reflect the source terms and propagation schemes used in the integrations. The energy spectra for all three methods have similar shapes to the corresponding spectra shown in Figure 5.6. However the bimodality at high frequencies is

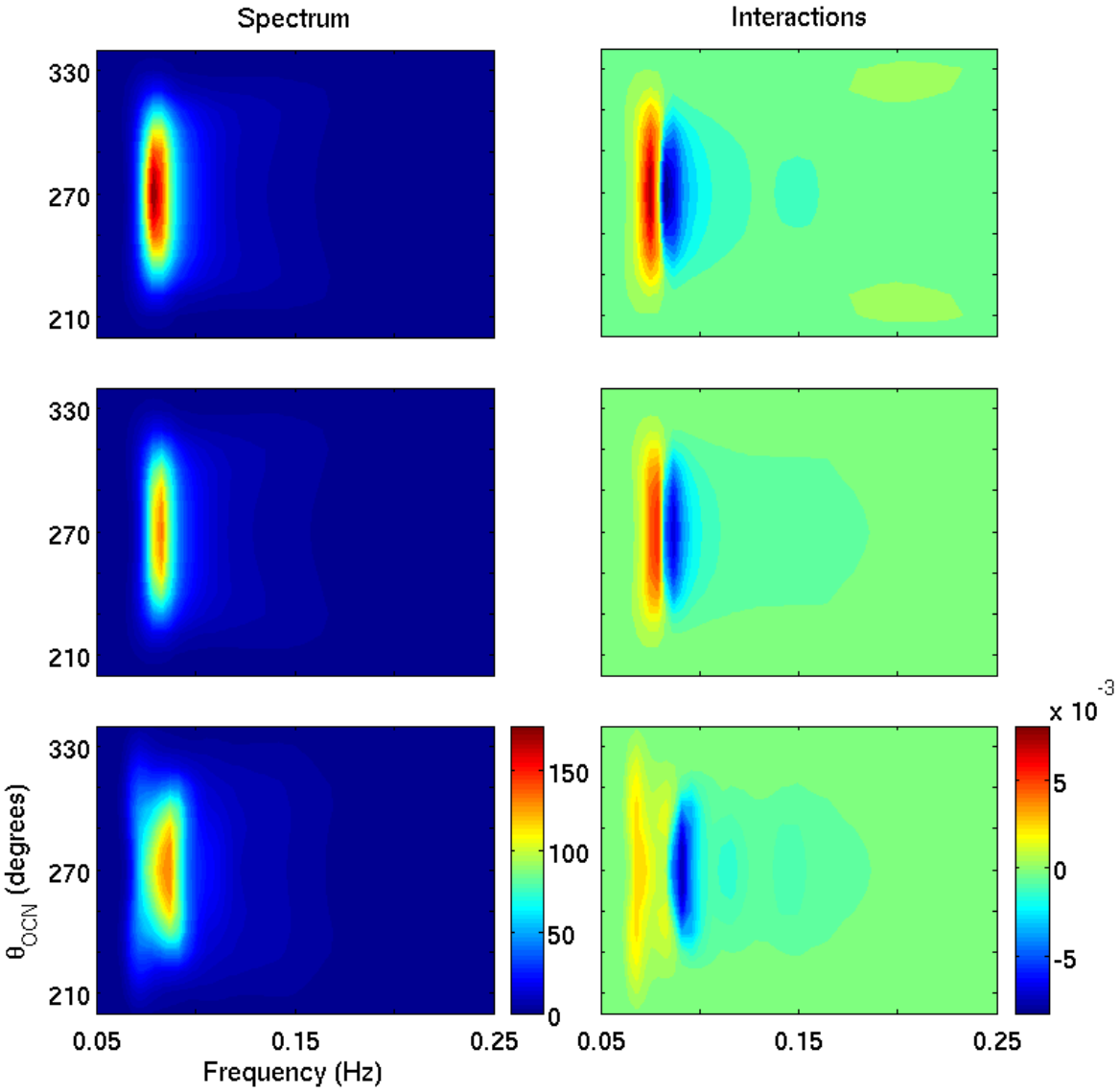

Figure 5.6: Wave energy spectrum ($m^2 Hz^{-1}$) (left) and non-linear interactions (m^2) (right) obtained with the WRT method (top), the TSA (centre) and the DIA (bottom) after 24 hours of easterly winds at 800 km fetch using the first order propagation scheme.

increased in all of them.

Similar large-scale features occur in the wave energy spectra and non-linear interactions after 48 hours. However, there are noticeable differences caused by the use of the two propagation schemes. With the first-order propagation scheme shown in Figure 5.7, the low frequency part of the interactions have kept the same shape as they had after 24 hours, however further structural features have appeared at high frequencies. Positive lobes are present for the DIA, and a further elongation of the negative lobe of the TSA, along with an extension of the bimodal energy spectrum towards higher frequencies. In the WRT and TSA non-linear interactions calculated from spectra obtained with the third-order propagation scheme, shown in Figure 5.8, the positive and negative lobes are wider in frequencies and angles and their peak values are lower than interactions from the first-order scheme. Positive lobes at higher frequencies are also visible, although the ones generated using the TSA cover a much wider fraction of the spectral space. Interactions from the DIA show the smallest differences between propagation schemes, although the high frequency positive lobes are missing.

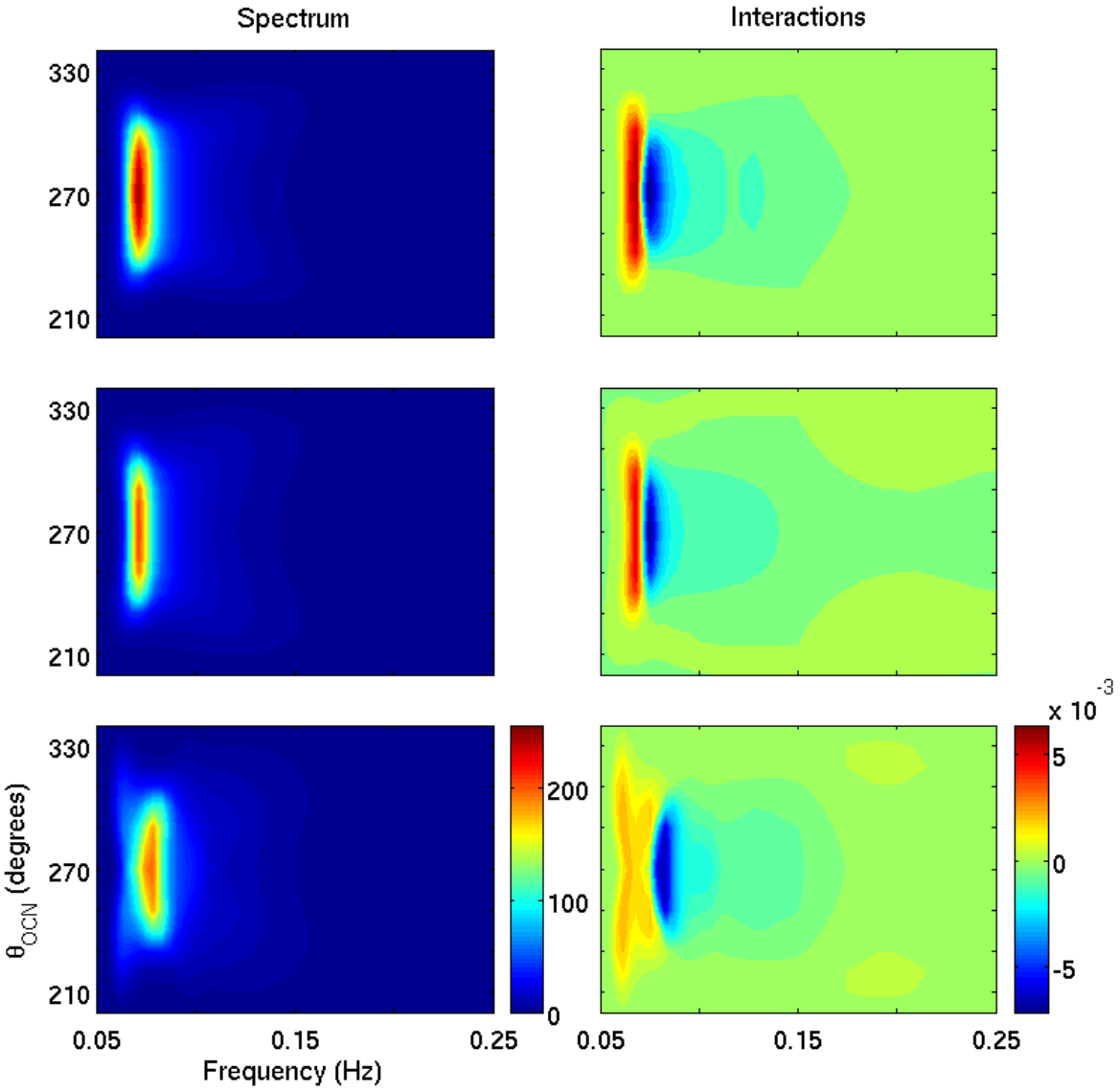

Figure 5.7: Wave energy spectrum ($m^2 Hz^{-1}$) (left) and non-linear interactions (m^2) (right) obtained with the WRT method (top), the TSA (centre) and the DIA (bottom) after 48 hours of easterly winds on a 800 km fetch using the first-order propagation scheme.

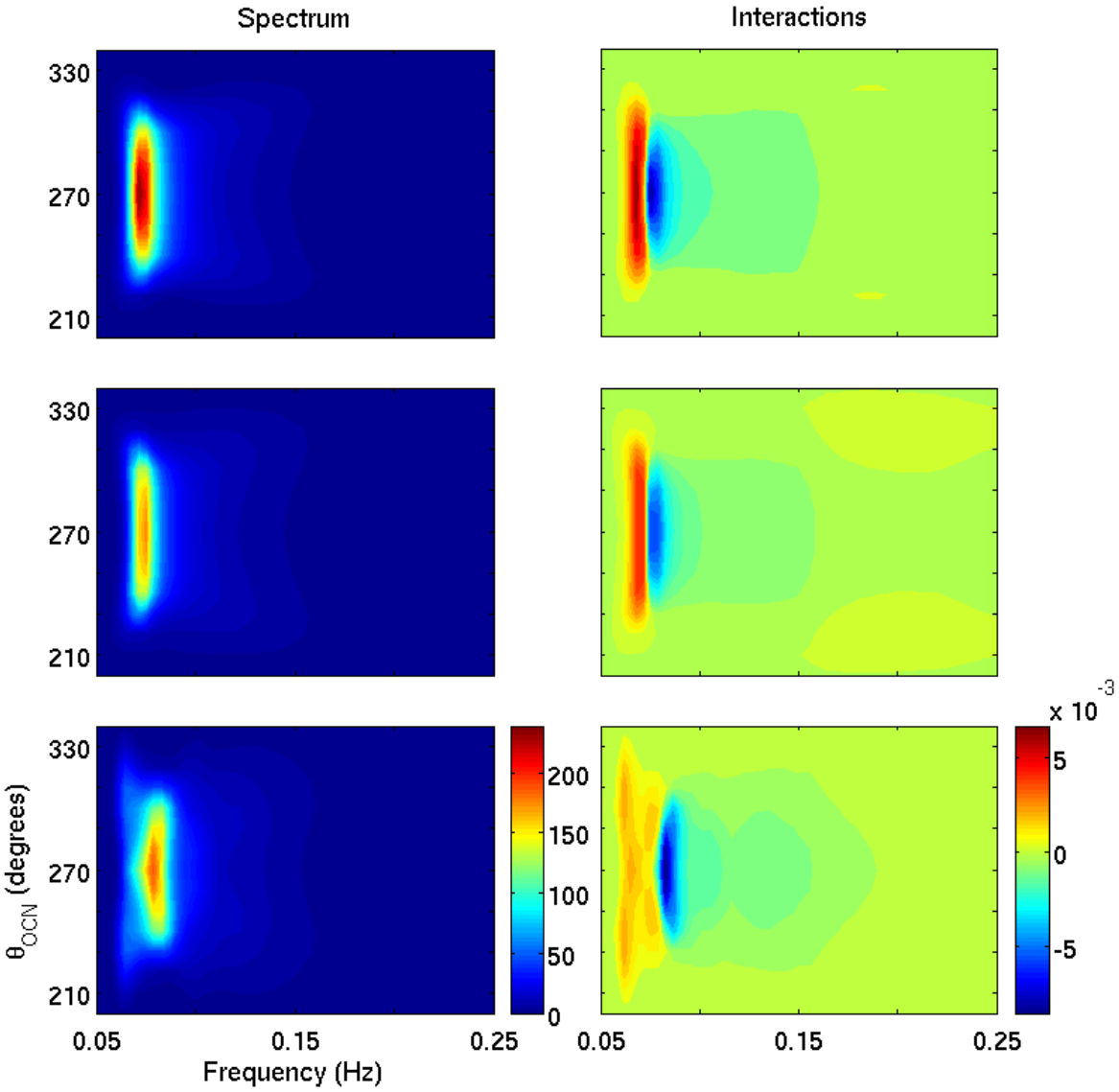

Figure 5.8: Wave energy spectrum ($m^2 Hz^{-1}$) (left) and non-linear interactions (m^2) (right) obtained with the WRT method (top), the TSA (centre) and the DIA (bottom) after 48 hours of easterly winds on a 800 km fetch using the third-order propagation scheme.

5.2 Turning Winds

This experiment was carried out to assess the performance of the three methods in simulating waves under turning winds on the two-dimensional domain. The wind forcing is the same as used in section 4.1, with 20 m/s winds coming from the east for 48 hours and then from the north for 72 hours. While the waves are growing, before the wind turns, the model results produced by the three methods are the same as described in section 5.1. Once the winds become northerly, since the swell generated initially does not propagate quickly outside of the domain (as in section 4.1), it can interact with the newly generated wind seas.

Waves generated in the first 48 hours of the simulation continue to propagate westward while a new wind sea begins to grow. The wave spectra generated by the easterly winds peak along the easterly direction ($\theta = 270^o$) and contain energy for directions ranging from $\theta = 200^o$ to $\theta = 340^o$. This range in directions means that some waves have a northward component in their direction while others have a southward component. The northerly wind removes energy from waves with a northward component in their direction and provides energy to the waves with a southward component, which creates asymmetries in the swell.

As seen in section 4.1, the current version of the TSA method has difficulties when dealing with swell and wind sea occurring at the same point. In this experiment, the time required for the swell to reach the edge of the domain is much longer, so the swell will interact with the wind sea over a greater length of time. After six hours of northerly winds, the wave field is significantly influenced by the new winds, as shown in Figure 5.9. The first noticeable feature is the region to the east of the domain where waves are now going southward. This comes from the swell propagating away from the region, leaving only the developing wind sea which is parallel to the wind.

Under the northerly wind, wave height contours would be expected to rotate counter-clockwise in time. However, this is not the case in all model runs. Both runs performed using the WRT method show contours rotating in the expected way. However, some

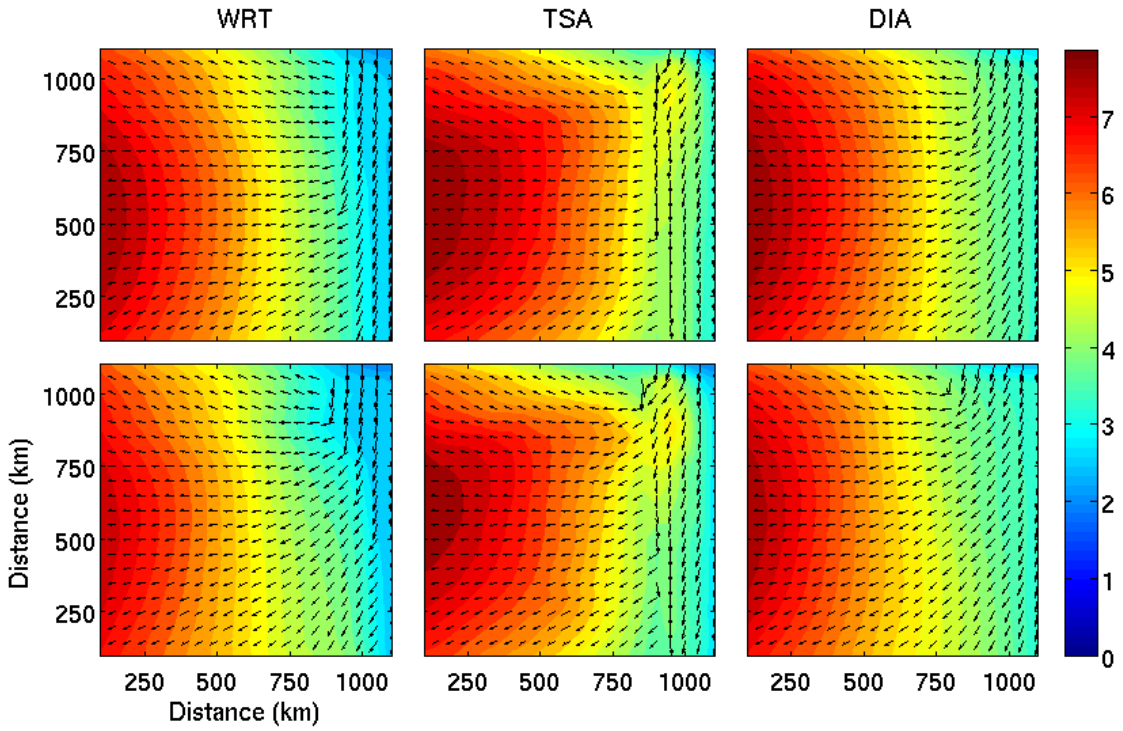

Figure 5.9: Significant wave height fields (in meters) and wave direction (arrows) after 48 hours of easterly winds followed by 6 hours of northerly winds obtained using the WRT (left), the TSA (centre) and the DIA (right) with the first and third order propagation schemes (top and bottom, respectively).

additional structures become visible. In the run with the third-order propagation scheme, an inversion in the contours curvature is observable close to the north edge of the domain. The distance between the northern edge and the inversion is the same as the distance to the eastward protrusions of significant wave height seen in the wave fields of the current TSA during the initial wave growth. This indicates that interactions with the boundaries can be an issue even with the WRT formulation for the non-linear interactions. The first order scheme also shows a change in curvature but the diffusion associated with the scheme mitigates it.

The wave fields obtained using the TSA show that the wind reinforces the northern protrusions of higher significant wave heights while the lower half of the domain is dominated by swell, still propagating westward. This results in a shape that is contrary to expectations. Model runs using the DIA show the smoothest contours of the three methods, with a hint

of boundary effect on the north side of the domain, which is more prominent on the east where wave heights are lower.

After 24 hours under the northerly winds, wave fields from the WRT and DIA methods are both showing convergence towards their equilibrium solutions. Fields from the TSA differ in intensity and in shape from the fields of the other methods. Wave heights are well above those obtained when using the WRT and DIA methods, with maximum wave heights of up to 14 m for the results using the TSA compared to maxima below 8 m for the other methods. Simulations using both propagation schemes show higher waves on the western side of the domain, which is where the influence of the swell was longest, with a maximum in the north-west corner of the domain, where the wave height protrusion did impact the early development of the waves.

At hour 120, after seventy-two hours of northerly winds, fields obtained with WRT and DIA have both reached their dynamical equilibrium, as shown in Figure 5.10. Fields generated using the TSA are still evolving but are converging towards their stable solutions as well, including the development of the extensions of high significant wave height along the edges of the domain. The return of the wave field to the expected equilibrium solution after the important disruption caused by the change in wind forcing shows the resilience of the WW3-TSA model to perturbations.

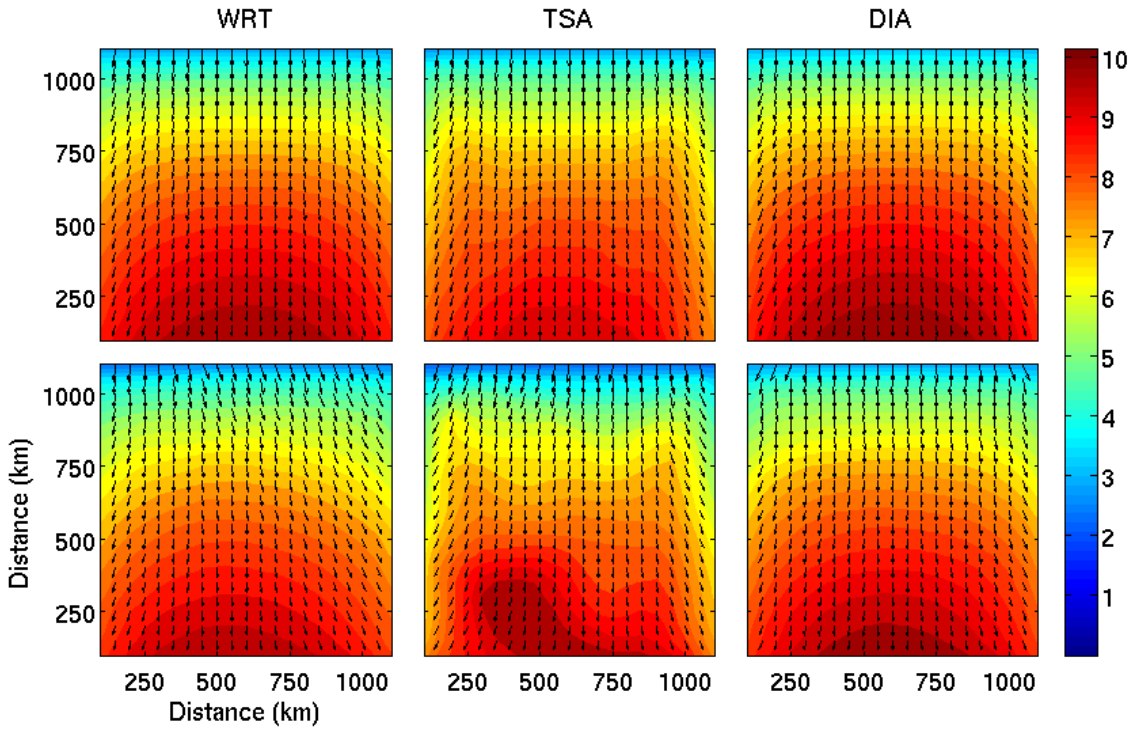

Figure 5.10: Significant wave height fields (in meters) and wave direction (arrows) after 48 hours of easterly winds followed by 72 hours of northerly winds obtained using the WRT (left), the TSA (centre) and the DIA (right) with the first and third order propagation schemes (top and bottom, respectively).

5.3 Slowly Turning Winds

This experiment was carried out to assess the performance of the three methods in simulating waves under slowly turning winds on the two-dimensional domain. Initial conditions were taken from section 5.1 and subjected to winds turning slowly southward over 24 hours followed by 72 hours of northerly winds.

Slowly turning winds were initially thought of as a favourable forcing for the current implementation of the TSA; this forcing should prevent the appearance of a distinct wind sea peak in addition to the swell. As was demonstrated in section 4.2, the asymmetries generated by the turning winds proved to be a different challenge to the TSA.

At hour 60, which is 12 hours after the wind has started to rotate, wind blows north-easterly. Waves in all the simulations show a transition from being parallel to the current

wind along the eastern border of the domain (Figure 5.11), where waves were just created, to being westward in the north-west corner where the swell peak has not yet been influenced by the wind. In the south-west corner of the domain, the peak wave direction also has rotated towards the current wind direction. This rotation comes from the combination of the swell with waves growing as they propagate southward from the north.

As in section 5.2, the most notable feature of the TSA is the further development of the northern region of anomalously high wave height under the turning winds. In this case, it is limited to a smaller part of the domain, especially when using the third order propagation scheme. The eastern edge of the domain, as well as a horizontal band in the centre, are relatively close to the results obtained from the other two methods. In the most part, peak wave directions over the domain are also similar to directions obtained using the WRT and DIA methods. This similarity suggests that discrepancies in wave heights originate from the high frequency part of the spectrum, while the peak region might be following a more normal evolution. Although the spurious features are still present at the end of the transition, the difference in maximum wave height between the TSA and WRT results is about 3 m, compared to 6 m in the previous section. Moreover, the perturbation does not extend all the way to the southern edge of the domain.

After the winds stop turning and remain northerly, the wave field of all methods start to converge to their dynamical equilibrium solutions. At hour 96, twenty-four hours after turning to northerly, fields obtained from both the WRT and DIA methods are very close to their stable solutions, while the TSA is still evolving. The TSA is taking longer to reach its equilibrium due to the magnitude of the perturbation of the wave field. When used with the first order propagation scheme, the TSA method produces results which are relatively close to the WRT equilibrium solution, more so than with the third order scheme which still shows spurious features. At hour 144, after seventy-two hours of constant forcing, fields from simulations using the TSA are close to their final wave fields for both of the propagation schemes and similar to Figure 5.10.

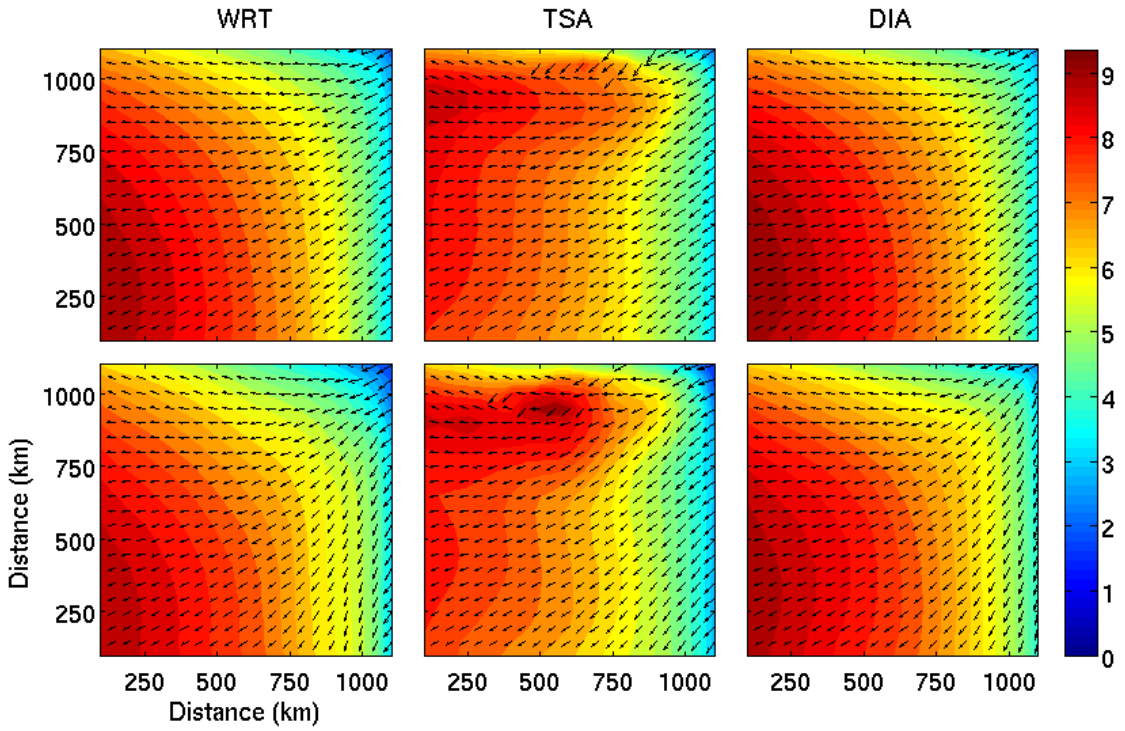

Figure 5.11: Significant wave height fields (in meters) and wave direction (arrows) 12 hours into the transition phase obtained using the WRT (left), the TSA (centre) and the DIA (right) with the first and third order propagation schemes (top and bottom, respectively).

In this experiment, as well as the previous section for sharply turning winds, the numerical diffusion of the first order scheme appears to be a significant advantage for the present version of the TSA. Although the TSA fields generated using both propagation schemes develop noticeable spurious features, a more diffusive propagation scheme tends to smooth spurious features, reducing their importance and allowing the model to reach its equilibrium solution faster. Under the perturbations described here and in section 5.2, although the simulations using the TSA do go through a phase where the solution degenerates, they remain stable enough to eventually converge back to their solution once conditions become more favourable to the parameterization.

5.4 Oblique Winds

This experiment was designed to further investigate the role played by wave propagation in the evolution of the wave field. The setup is the same as for the the experiment described in section 5.1 except that, instead of being easterly, the wind is north-easterly. Although this is a relatively small change, the implications for wave propagation in a model with a cartesian domain are significant. Instead of propagating mainly along one of the main axis of the domain, the waves are now oblique to both axis which complicates the propagation.

5.4.1 Field Evolution

During the first 18 hours of wave growth, all model variations perform relatively well. The impact of wave propagation scheme is very small and, as in the case of the other experiments, the model runs using the TSA method produce slower growth then when using the WRT method while model runs using the DIA method reach higher energy levels quicker. Otherwise, wave fields at hour 12, shown in Figure 5.12, exhibit little difference between model runs.

At hour 18, the first spurious features start to show in the TSA runs, in the north-east corner of the domain, as shown in Figure 5.13. At this point, the only impact of the propagation scheme is that waves modelled using the third order propagation scheme reach higher levels at a given fetch for all methods, which is indicated by more closely spaced significant wave height contours.

Later in the model run, the boundary effects seen in previous sections become visible, creating lobes of higher significant wave height along the northern and eastern edges of the domain. After twenty four hours, the wave fields from model runs using the WRT and DIA methods are in very good agreement, while the results from the TSA have much faster wave growth than the other methods, close to the northern and eastern edges. However, the saturation levels obtained with the TSA are up to two meters lower than those of the other methods. The overall maximum wave height, which occurs in the south-west corner of the domain, is relatively unaffected and shows the usual influence of non-linear interactions, with the DIA producing the highest waves and the TSA the smallest.

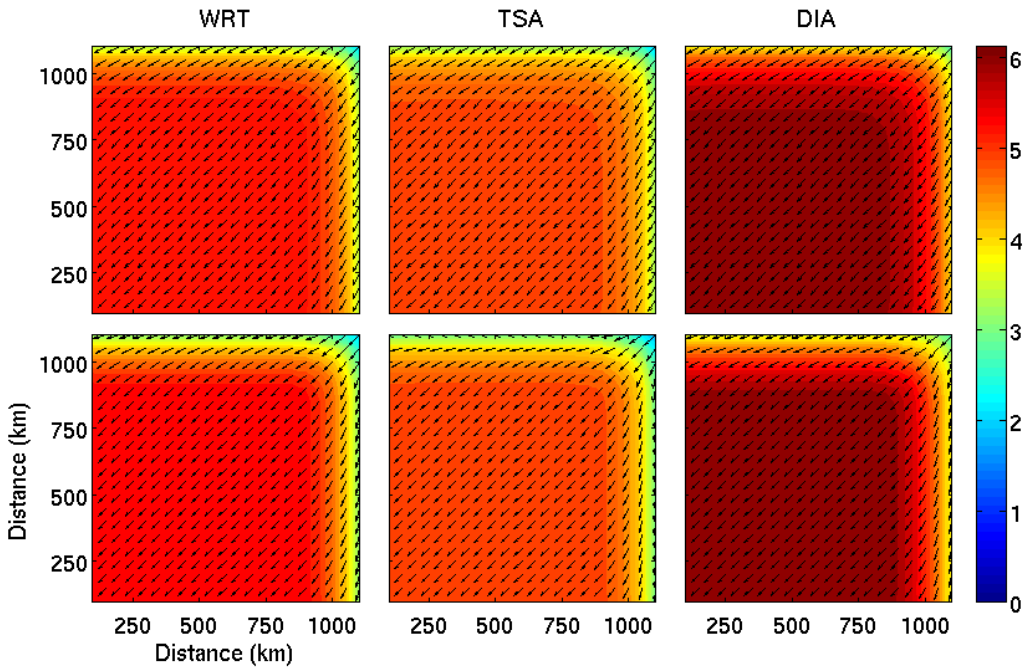

Figure 5.12: Significant wave height fields (in meters) and wave direction (arrows) after 12 hours of north-easterly winds obtained using the WRT (left), the TSA (centre) and the DIA (right) with the first and third order propagation schemes (top and bottom, respectively).

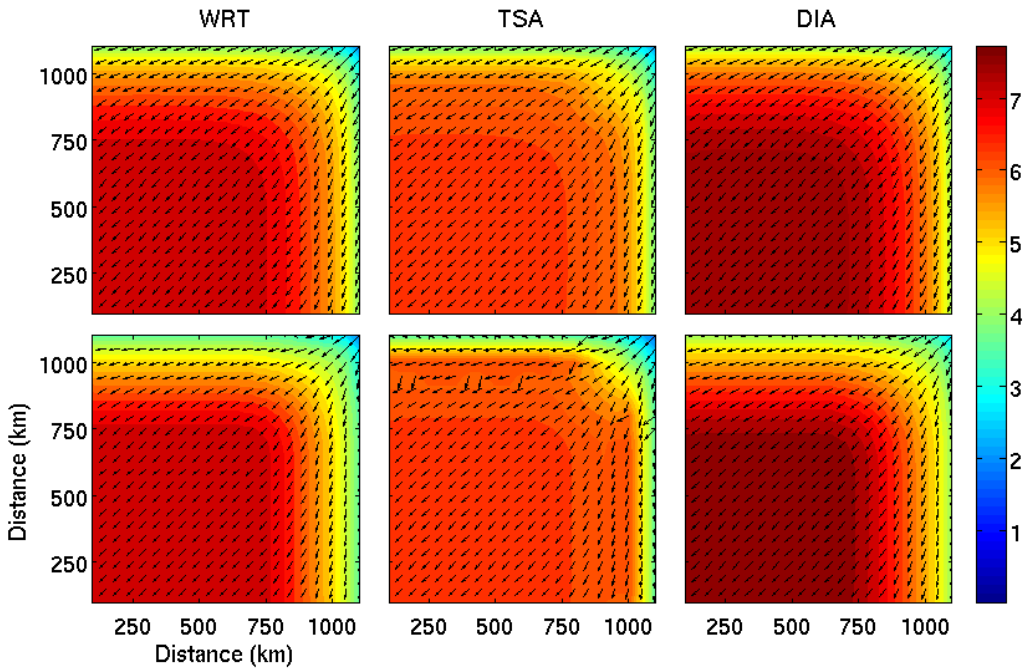

Figure 5.13: Significant wave height fields (in meters) and wave direction (arrows) after 18 hours of north-easterly winds obtained using the WRT (left), the TSA (centre) and the DIA (right) with the first and third order propagation schemes (top and bottom, respectively).

5.4.2 Spectral Evolution

Looking at the wave energy spectrum and associated interactions, overall results are consistent with those shown in section 5.1. TSA produces spectra which have a much closer shape to the WRT spectra than the DIA. The non-linear wave-wave interactions, especially around the peak, are also very similar, while the positive lobe of the interactions produced using DIA remains quite far away and is responsible for the discrepancies observed in the shape of the energy spectrum.

The wind used in this experiment blows towards the south-west of the domain, at an angle of 225^o in polar coordinates, which are the coordinates used for the internal computations of WW3. The angular distribution of the spectral grid used in these simulations has 10^o resolution. The energy spectrum created under these conditions therefore tends to be split between two directions, 220^o and 230^o. As described in section 3.2.1, the parameterization used for the broad-scale in the TSA in this implementation finds the spectral peak in the one-dimensional spectrum, then the direction where the energy is maximized for that given frequency.

In this situation, there is not a single direction with maximum energy, but two, which the current parameterization cannot account for. This results in the broad-scale component peaking preferentially in one of the two directions, until the energy at the discounted direction becomes larger, causing a shift in the location of the broad-scale direction. This oscillation can be seen in Figures 5.14 to 5.16 where spectra and associated interactions for the thirteenth to fifteenth hours of the simulation are shown for the model output point #1, which is at maximal fetch for the diagonal winds.

In these figures, although the energy spectrum and non-linear interactions obtained with the TSA are both close to those from WRT, asymmetries can be seen in the non-linear interactions resulting from TSA. The other methods, WRT and DIA, have fully symmetric formulations and do not show this. At hour 13, TSA's extension of the negative lobe of the non-linear interactions towards higher frequencies has higher amplitudes for waves

centred around 210^o (see Figure 5.14) instead of being spread around 220^o to 230^o like the other methods. TSA's positive lobes at high frequencies are also different, with the one centred around 270^o starting at higher frequencies than the other lobe.

An hour later (hour 14), the wave energy spectrum, shown in Figure 5.15, produces an almost symmetric interaction spectrum for the TSA, with minor changes for the results from WRT or DIA. At hour 15, shown in Figure 5.16, the directional location of the broad-scale term has once again changed and the negative lobe is now slanted towards more westward directions. There is also a small positive lobe around 270^o which has no mirror image. Over the course of the experiment, both the WRT and DIA methodologies remain symmetric at all times, whereas the TSA results, due to the formulation of its parameterization, produces asymmetric non-linear interactions and energy spectra.

This also sheds a new light on the boundary effects observed with the TSA results. Points close to the edge of the domain receive energy from the centre of the domain because waves do not propagate exclusively in the direction of the wind. However, they do not receive any energy from the edge of the integration domain, as it is represented by land, which simply absorbs all incoming energy. This can create asymmetric spectra, or potentially spectra which peak for a direction that falls between directions defined in the spectral grid. Addressing these two issues could mitigate the edge effects observed when using the TSA.

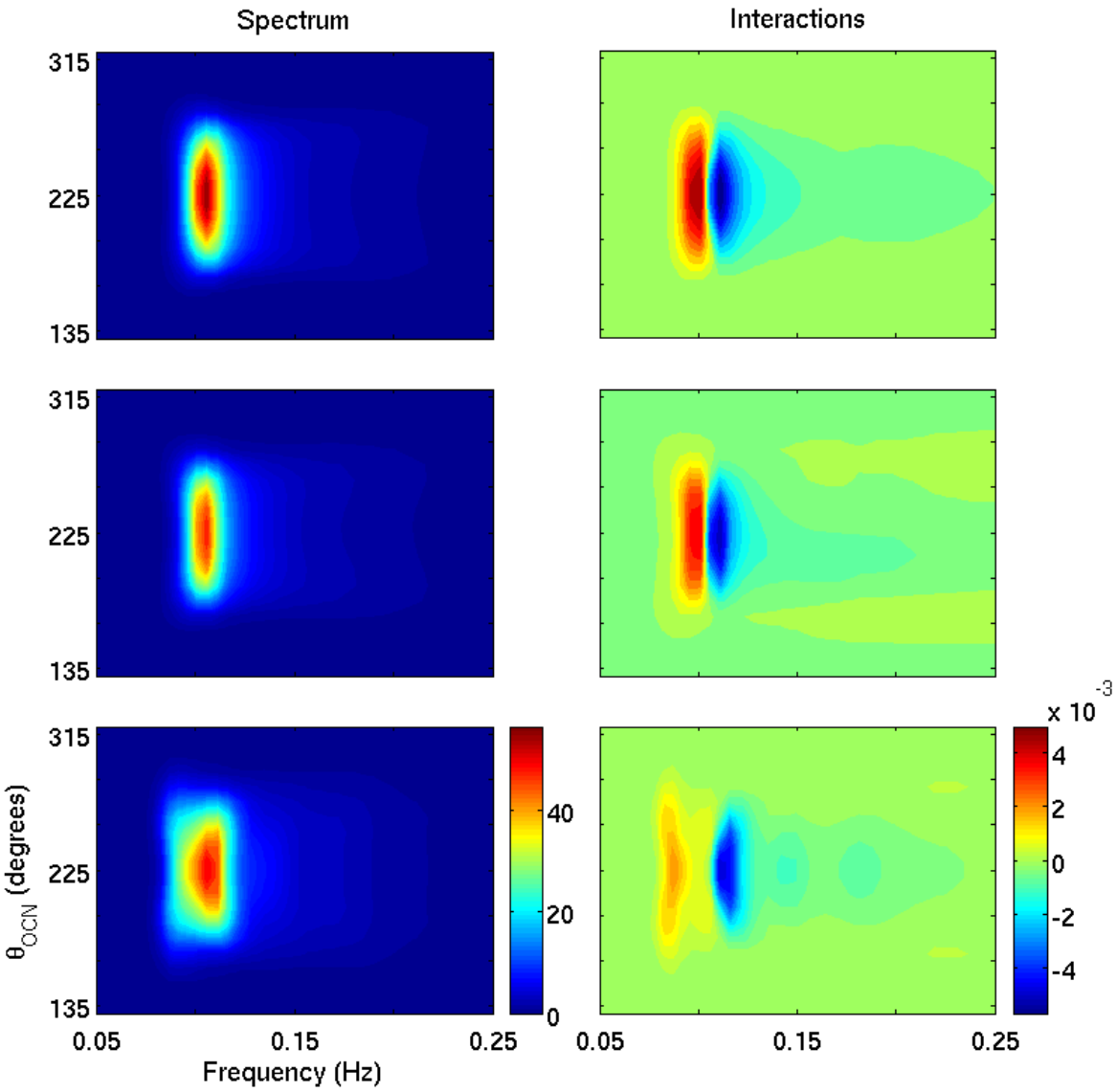

Figure 5.14: Wave energy spectrum (m^2Hz^{-1}) (left) and non-linear interactions (m^2) (right) obtained with the WRT method (top), the TSA (centre) and the DIA (bottom) after thirteen hours of north-easterly winds at model output point #1 using the first-order propagation scheme.

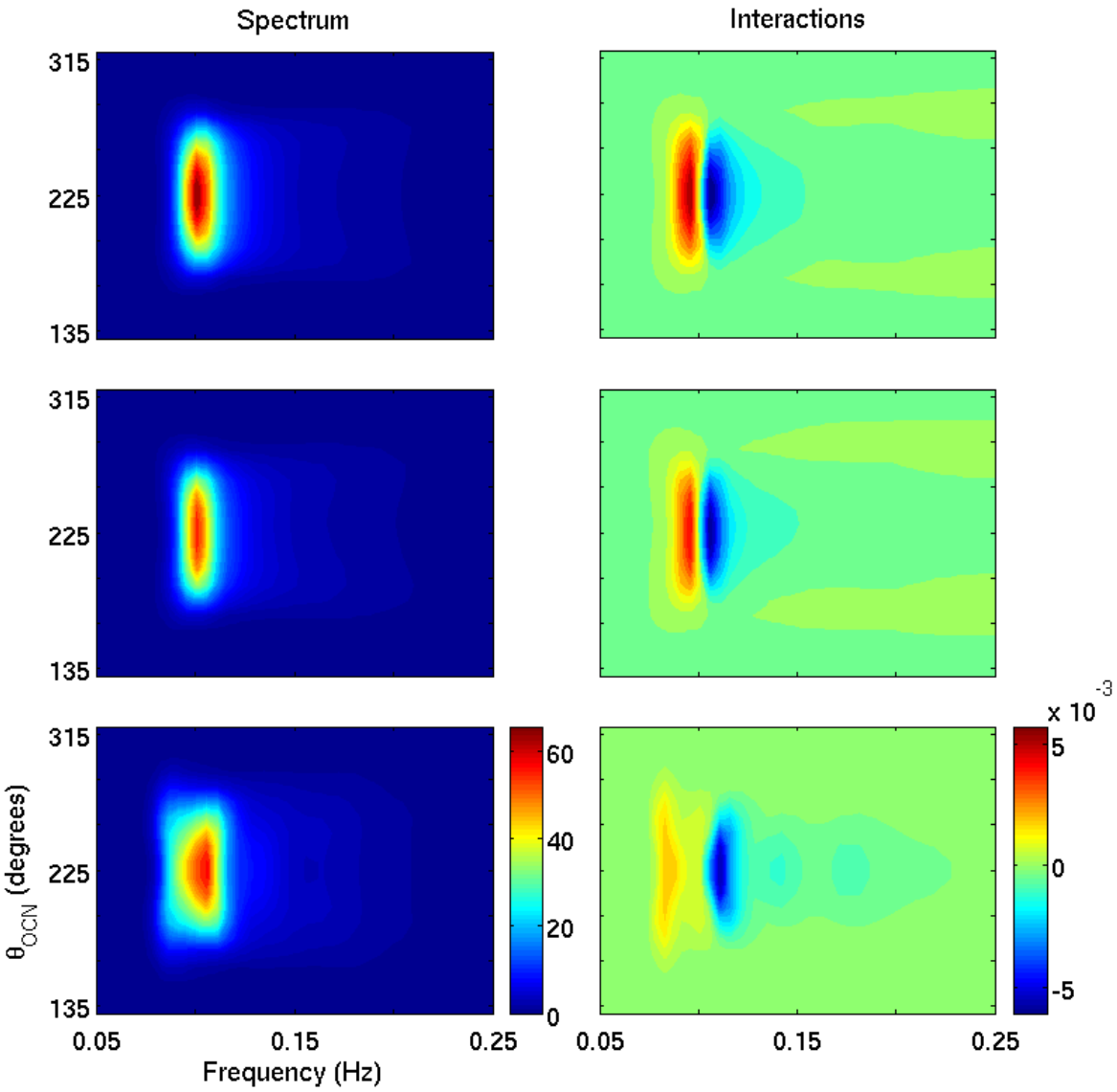

Figure 5.15: Wave energy spectrum ($m^2 Hz^{-1}$) (left) and non-linear interactions (m^2) (right) obtained with the WRT method (top), the TSA (centre) and the DIA (bottom) after fourteen hours of north-easterly winds at model output point #1 using the first-order propagation scheme.

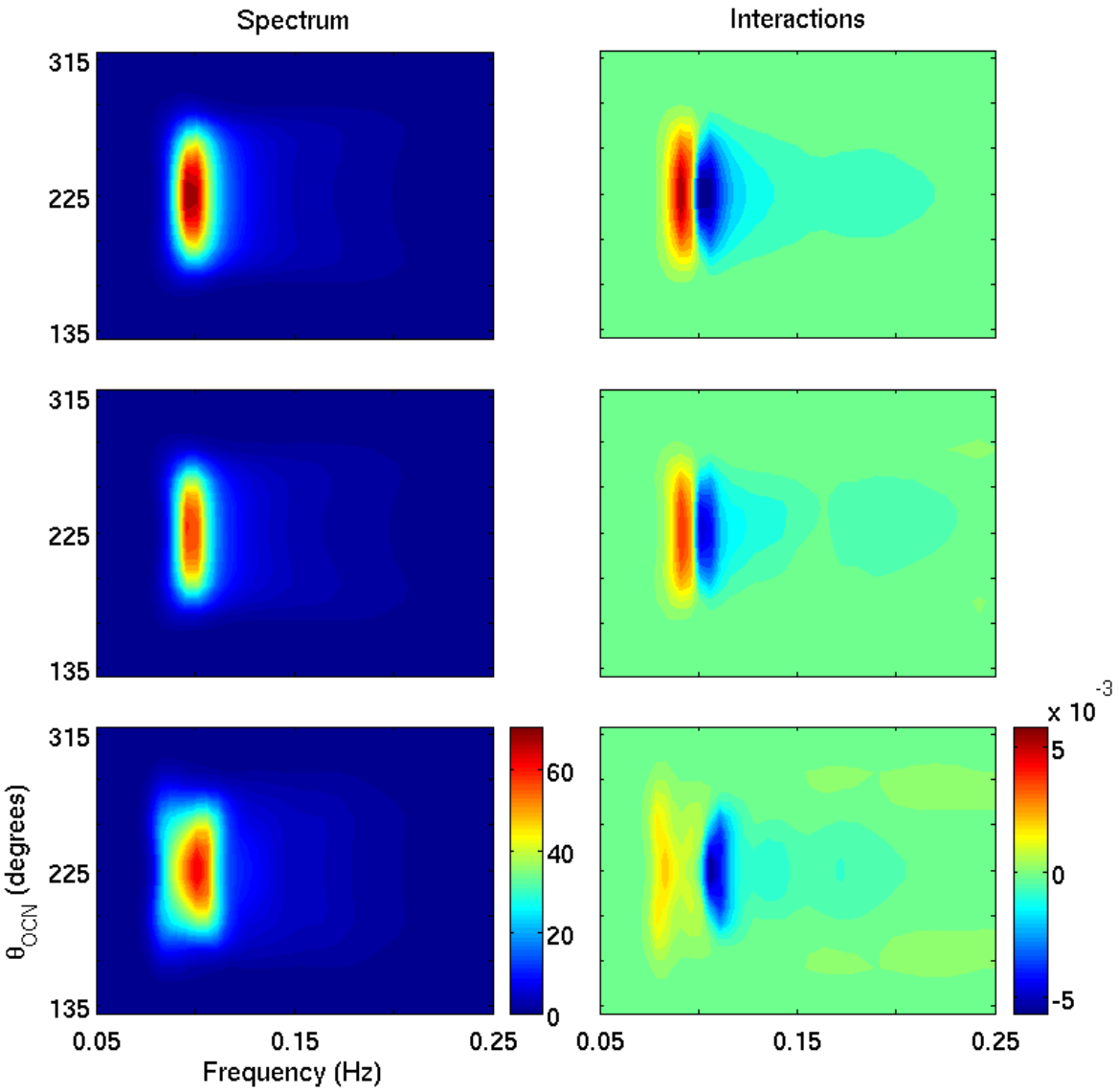

Figure 5.16: Wave energy spectrum (m^2Hz^{-1}) (left) and non-linear interactions (m^2) (right) obtained with the WRT method (top), the TSA (centre) and the DIA (bottom) after fifteen hours of north-easterly winds at model output point #1 using the first-order propagation scheme.

5.5 Diagonal Front

This experiment builds upon the turning winds experiment. Here, instead of turning the winds at a predefined time over the whole domain, a front divides the domain diagonally from the north-west to the south-east. Winds in the south-west half of the domain are orientated northerly, which is towards the front. In the north-east half of the domain, winds are westerly, going away from the front. Waves created in the south-west section of the domain thus propagate towards the front and cross it at different periods of their evolution depending on the distance from their point of origin to the front.

Wave fields produced with the frontal winds all share a similar shape in the early hours of evolution, shown in Figure 5.17 at hour 15. Two maxima occur in the domain, around the areas with the longest fetch before and after the waves encounter the front. Normal wave evolution with losses on the western edge of the domain and the front explain the triangular shape. Once waves cross the front, energy loss to the wind causes a brief decrease in wave height, followed by an increase as the new wind waves develop. Longer fetches in the northern section of the domain allow for higher waves to develop. At hour 21, fields produced using the TSA begin to show the influence of the model's boundary in the western part of the domain, and an inversion in concavity in the southern contours close to the front.

Later in the model runs, the maxima in wave heights occur closer to the boundary of the domain, where the fetch is longest, for the WRT and DIA cases, but not for the TSA results where changing winds (as waves cross the front) cause the maximum to occur near the centre of the domain, just past the front. The saddle point seen near the middle of the domain for both the WRT and DIA simulations is also present with the TSA results, although the loss of energy from crossing the front is smaller. Figure 5.18 shows the fields at hour 24 and the absence of the concavity in the southern contours for the TSA results.

The model runs using the TSA show a rapid turning in peak directions as waves cross the wind fronts along with an increase in significant wave heights, hinting at problems in handling the wind shift. This is expected given the results from section 5.2. On the other

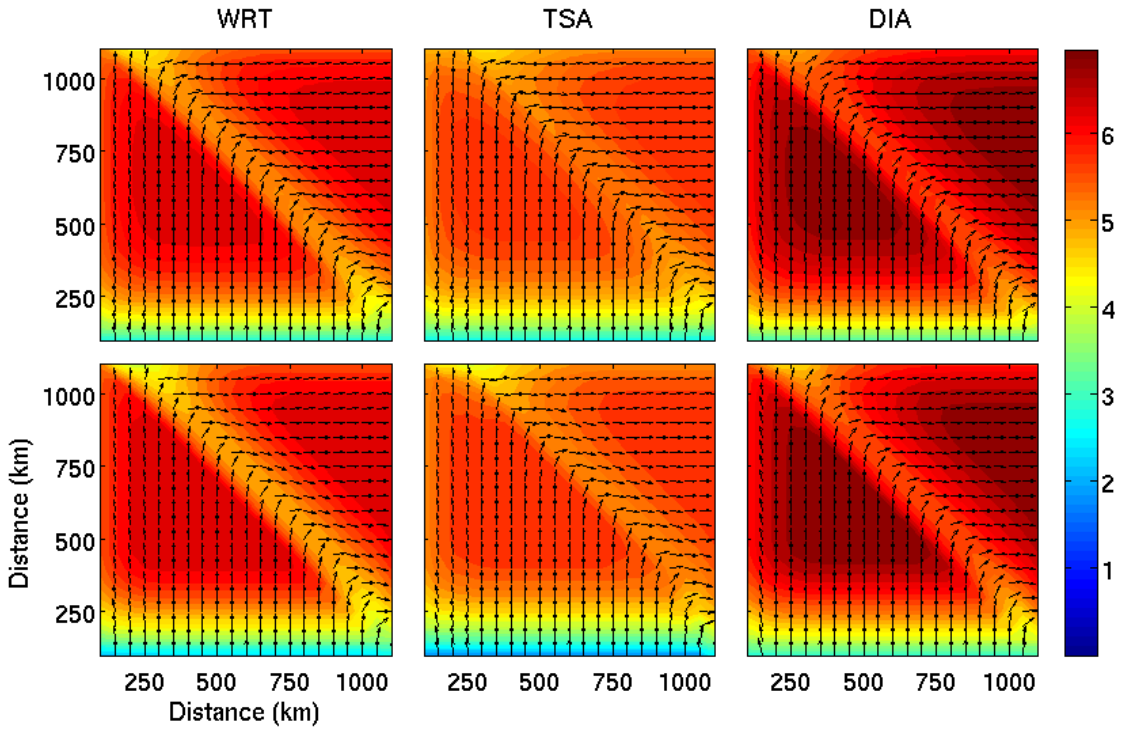

Figure 5.17: Significant wave height fields (in meters) and wave direction (arrows) 15 hours into the diagonal front experiment for the WRT (left), the TSA (centre) and the DIA (right) using the first and third order propagation schemes (top and bottom, respectively).

hand, similarities in the southern half of the domain indicate that, with a younger swell peaking at higher frequencies, the evolution under perpendicular winds is resolved more accurately by the TSA than for older swell in the northern half.

At hour 48, the wave fields have mostly reached their equilibrium solutions. For all simulations, the southern half of the domain shows very similar features, including the loss of energy to the western model boundary and straight contours with a concave eastern side. The influence of the wind front on the wave field is very similar for the model runs using the WRT and DIA methods, with waves further north than two-thirds of the domain not changing directions as the swell overwhelms the developing wind sea. The wave fields obtained with the TSA method are similar to those at hour 24 and the southern half of the domain shows better agreement with fields obtained with the WRT method.

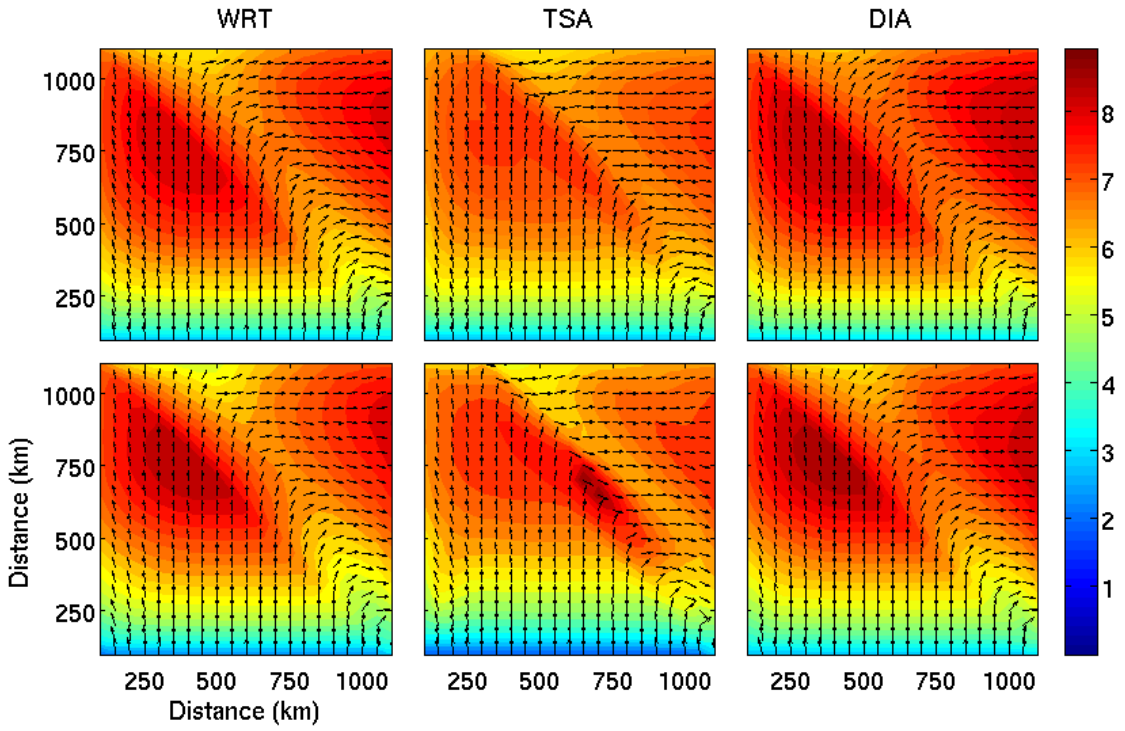

Figure 5.18: Significant wave height fields (in meters) and wave direction (arrows) 24 hours into the diagonal front experiment for the WRT (left), the TSA (centre) and the DIA (right) using the first and third order propagation schemes (top and bottom, respectively).

CHAPTER 6

SUMMARY AND DISCUSSION

Calculation of the non-linear wave-wave interactions represents one of the most computationally expensive steps for numerical wave models. In order to meet the inherent time constraints of operational modelling, only a crude approximation, the Discrete Interactions approximation (DIA), has been used until now. The two-scale approximation, called TSA, is a new method for the computation of non-linear wave-wave interactions. The TSA was successfully implemented in WaveWatchIII (denoted WW3), an operational numerical wave forecast model. The TSA method makes use of a multi-step process in order to simplify the required computations. From the input energy spectrum, a broad-scale term is constructed to contain the majority of the energy and is assumed to have a predefined parametric shape. The difference between the actual spectral energy and the broad-scale term is calculated and stored as the local-scale or perturbation term. Using these two terms, the non-linear wave-wave interactions are then generated (*Resio and Perrie*, 2008). Results presented in this study confirm the initial findings of *Perrie and Resio* (2009), that the TSA method produces nonlinear wave-wave interaction spectra which closely resemble the results of so-called exact methods, in this case the WRT method (*Webb*, 1978; *Tracy and Resio*, 1982; *Resio and Perrie*, 1991).

Numerical studies of the impact of multiple successive time integrations of source terms on the wave energy spectrum were performed. In the case of steady wind forcing with wind speed and direction held constant, the TSA is able to generate a succession

of wave energy spectra whose shape is much closer to results obtained using the WRT method when compared with results obtained with the DIA. The two main mean wave parameters used in operational forecasting and modelling, significant wave height and peak frequency, are accurately simulated by the wave model using the TSA in the first ten hours of wave growth. Given WW3's default source terms for wind input energy S_{in}, and wave dissipation S_{ds}, accuracy for significant wave height deteriorates after the first ten hours of wave growth but tracking of peak frequency remains excellent up to and including the time where the system reaches dynamical equilibrium. The actual two-dimensional energy spectra produced using the TSA also show very good agreement with WRT results in shape, while the magnitude of the energy peak is lower, explaining the difference in significant wave height between the two methods.

Two duration-limited experiments were performed with WW3's default source terms, using sharply turning and slowly turning winds. In these numerical experiments, the transitions initiate oscillations in the energy spectra and associated non-linear interactions from the TSA. These stem from asymmetries created in the energy spectrum which the current formulation of the parametric shape used to define the broad-scale term cannot take into account. In the case of sharply turning winds, a second peak is generated, whereas the slowly turning winds create intense asymmetries as the waves rotate to follow the wind. In both cases, these perturbations exceed the range of applicability of the current TSA formulation. However, once the forcing stops changing, the TSA results converge to the solutions obtained using the WRT method. Furthermore, taking those situations into account for the formulation of TSA's parametric shape would allow the TSA to properly model them.

In order to assess the skill of the current implementation of the TSA in a situation more akin to operational wave modelling, simulations of wave growth over a two-dimensional domain were performed. Under constant wind forcing, the significant wave heights and peak frequencies produced by the TSA show good agreement with results obtained using the WRT method and DIA. Notable boundary edge effects are observed, which stem from

TSA's current parametric shape not taking into account the asymmetries in the energy spectrum. This effect can be somewhat mitigated by numerical diffusion. Duration-limited growth at points taken far from the sides of the domain, and where fetch is the longest, show consistent results with the time integration experiment; TSA produces accurate spectral shapes with slightly lower spectral energies. Fetch-limited growth curves taken in the centre of the domain along the wind direction are similar, with agreement for both significant wave heights and peak directions at short fetch. Further along the fetch, significant wave heights from TSA do not increase as rapidly with fetch as with other two methods. However, the peak frequency from TSA results remains closer to results obtained with the WRT method than the DIA.

Additional experiments, inspired by tests described in *SWAMP* (1985), were performed on the two-dimensional domain to investigate the robustness of the current implementation of the TSA in the wave model. First, slowly and sharply turning winds were applied to the waves after they had reached their equilibrium sea state. Results from these experiments show the importance of adding the possibility of asymmetries and multiple peaks into the formulation for the parametric shape of the broad-scale component. Once the winds stabilize over the domain, the wave field once again converges towards its equilibrium solution, showing that the model is stable when subjected to temporary perturbations that take it outside its current realm of applicability. Wave growth under slanting winds was also studied, which created a situation where the energy peak was spread over two neighbouring frequencies. Accounting for this possibility in the creation of the broad-scale term will improve the range of situations for which the TSA method might be applicable. Study of frontal winds showed that the WW3-TSA was more successful in modelling wind shifts for younger seas than for strong swell which can create unstable situations. This issue, along with the turning wind cases, can be addressed by allowing for multiple peaks and asymmetries to be taken into account for the parametric broad-scale term.

Overall, the model results presented in this thesis have demonstrated the potential for increased accuracy provided by the TSA method when compared to the DIA, for both

wave energy spectra and the non-linear interactions, over time and spatial scales that allow the spectrum to reach its dynamical equilibrium. For these cases, the current method for the decomposition of the energy spectra into the two different scales required by TSA proved to be adequate. With the proper broad-scale and local-scale energy components, the approximation to the complete non-linear interactions performed by the TSA is successful in producing time-series of energy and non-linear interaction spectra that closely resemble the ones obtained with the WRT method.

The various experiments constructed in this study to simulate complicated sea states suggest that allowing for the possibility of multiple peaks and asymmetries in the parametric shape (when generating the broad-scale term) should yield a notable enhancement of the range of applicability of the TSA. Investigation of the neglected terms in the approximation and of a two-dimensional spectrum fitting method could also be considered. Upon implementation of the improvements to the parametric shape, along with the fulfilment of the time saving potential of the approximation, TSA should become a serious contender for the computation of non-linear interactions in both research and operational wave models.

BIBLIOGRAPHY

Andrews, D., and M. McIntyre, On wave action and its relatives, *Journal of Fluid Mechanics*, *89*, 647–664, 1978.

Bowyer, P., and A. MacAfee, The theory of trapped-fetch waves with tropical cyclones - an operational perspective., *Weather Forecasting*, *20*, 229–244, 2005.

Cardone, V. J., R. E. Jensen, D. T. Resio, V. R. Swail, and A. T. Cox, Evaluation of contemporary ocean wave models in rare extreme events: the "Halloween Storm" of October 1991 and the "Storm of the Century" of March 1993, *Journal of Atmospheric and Oceanic Technology*, *13*, 198–230, 1996.

Chalikov, D. V., The parameterization of the wave boundary layer, *Journal of Physical Oceanography*, *25*, 1333–1349, 1995.

Chalikov, D. V., and M. Y. Belevich, One-dimensional theory of the wave boundary layer, *Boundary Layer Meteorology*, *63*, 65–96, 1993.

Davis, R. W., and E. F. More, A numerical study of vortex shedding from rectangles, *Journal of Fluid Mechanics*, *116*, 475–506, 1982.

Hasselmann, K., On the non-linear transfer in a gravity wave spectrum, Part 1. General theory, *Journal of Fluid Mechanics*, *12*, 481–500, 1962.

Hasselmann, S., and K. Hasselmann, Computations and Parameterizations of the Nonlinear Energy Transfer in a Gravity-Wave Spectrum. Part I: A New Method for Efficient Computations of the Exact Nonlinear Transfer Integral, *Journal of Physical Oceanography*, *15*, 1369–1377, 1985.

Hasselmann, S., K. Hasselmann, J. H. Allender, and T. Barnett, Computations and Parameterizations of the Nonlinear Energy Transfer in a Gravity-Wave Spectrum. Part II: Parameterizations of the Nonlinear Energy Transfer for Application in Wave Models, *Journal of Physical Oceanography*, *15*, 1378–1391, 1985.

Holthuijsen, L. H., *Waves in Oceanic and Coastal Waters*, Cambridge University Press, 2007.

Janssen, P., Quasilinear Approximation for the Spectrum of Wind-Generated Water Waves, *Journal of Fluids Mechanics*, *117*, 493–506, 1982.

Leonard, B. P., A stable and accurate convective modelling procedure based on quadratic upstream interpolation, *Computational Methods Applied to Mechanical Engineering*, *18*, 59–98, 1979.

Leonard, B. P., The ultimate conservative difference scheme applied to unsteady one-dimensional advection, *Computational Methods Applied to Mechanical Engineering*, *88*, 17–74, 1991.

Liu, P. C., D. J. Schwab, and R. E. Jensen, Has wind-wave modeling reached its limit?, *Ocean Engineering*, *29*, 81–98, 2000.

Long, C., and D. Resio, Wind wave spectral observations in Currituck Sound, North Carolina, *Journal of Geophysical Research-Oceans*, *112*, C05,001, 2007.

MacAfee, A. W., and P. J. Bowyer, The modeling of trapped-fetch waves with tropical cyclones - a desktop operational model, *Weather Forecasting*, *20*, 245–263, 2005.

Miles, J. W., On the generation of surface waves by shear flows, *Journal of Fluids Mechanics*, *3*, 185–204, 1957.

Moon, I., I. Ginis, and H. T., Effect of Surface Waves on Air-Sea Momentum Exchange. Part II: Behavior of Drag Coefficient under Tropical Cyclones, *Journal of Atmospheric Sciences*, *61*, 2334–2348, 2004.

Perrie, W., and D. Resio, A two-scale approximation for efficient representation of nonlinear energy transfers in a wind wave spectrum - part 2: Application to observed wave spectra, *Journal of Physical Oceanography*, *39*, 2451–2476, 2009.

Perrie, W., A. Susilo, and B. Toulany, A new approximation for nonlinear wave-wave interactions, *Ocean Modeling*, *33*, 159–176, 2010.

Qiao, F., Y. Yuan, Y. Yang, Q. Zheng, C. Xia, and J. Ma, Wave-induced mixing in the upper ocean: Distribution and application to a global ocean circulation model, *Geophysical Research Letters*, *31*, L11,303, 2004.

Resio, D. T., and W. Perrie, A numerical study of nonlinear energy fluxes due to wave-wave interractions. part 1: Methodology and basic results, *Journal of Fluids Mechanics*, *223*, 609–629, 1991.

Resio, D. T., and W. Perrie, A two-scale approximation for efficient representation of nonlinear energy transfers in a wind wave spectrum - part 1: Theoretical development, *Journal of Physical Oceanography*, *38*, 2801–2816, 2008.

Smith, J., Wave-current interactions in finite-depth, *Journal of Physical Oceanography*, *36*, 1403–1419, 2006.

SWAMP, *Ocean Wave Modeling*, Plenum Press, 1985.

Tolman, H., V. Krasnopolsky, and D. Chalikov, Neural network approximations for nonlinear interactions in wind wave spectra: direct mapping for wind seas in deep water, *Ocean Modelling*, *8*, 253–278, 2005.

Tolman, H. L., Optimum discrete interaction approximations for wind waves. part 3: Generalized multiple dias., *Tech. rep.*, Note 269 NOAA/NWS/NCEP/MMAB, 2008.

Tolman, H. L., *User manual and system documentation of WAVEWATCH III, version 3.14*, Environmental Modeling Center Marine Modeling and Analysis Branch, 3.14 ed., 2009.

Tolman, H. L., and D. Chalikov, Source terms in a third-generation wind wave model, *Journal of Physical Oceanography*, *26*, 2497–2518, 1996.

Tracy, B. A., and D. T. Resio, Theory and calculation of the nonlinear energy transfer between sea waves in deep water, *Tech. rep.*, 1982.

WAMDI, The wam model a third generation oceans wave prediction model, *Journal of Physical Oceanography*, *18*, 1775–1810, 1988.

Warner, J. C., B. Armstrong, R. He, and J. B. Zambon, Development of a coupled oceanatmospherewavesediment transport (coawst) modeling system, *Ocean Modeling*, *35*, 230–244, 2010.

Webb, D. J., Non-linear transfers between sea waves, *Deep Sea Research*, *25*, 279–298, 1978.

Whitham, G. B., A general approach to linear and non-linear dispersive waves using a lagrangian., *Journal of Fluid Mechanics*, *22*, 273–283, 1965.

Zakharov, W., and N. Filonenko, The energy spectrum for stochastic oscillation of a fluid surface, *Doklady Akademii Nauk*, *170*, 1291–1295, 1966.